









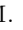
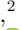


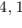










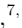















THE ALPINE-ALMA [CII] SURVEY: MULTI-WAVELENGTH ANCILLARY DATA AND BASIC PHYSICAL MEASUREMENTS

A. L. FAISST ¹, D. SCHAEERER ^{2,3}, B. C. LEMAUX ⁴, P. A. OESCH ², Y. FUDAMOTO ², P. CASSATA ^{5,6},
M. BÉTHERMIN ⁷, P. L. CAPAK ^{1,8,9}, O. LE FÈVRE ⁷, J. D. SILVERMAN ^{10,11}, L. YAN ¹², M. GINOLFI ²,
A. M. KOEKEMOER ¹³, L. MORSELLI ^{5,6}, R. AMORÍN ^{14,15}, S. BARDELLI ¹⁶, M. BOQUIEN ¹⁷, G. BRAMMER ⁸,
A. CIMATTI ^{18,19}, M. DESSAUGES-ZAVADSKY ², S. FUJIMOTO ^{20,21}, C. GRUPPIONI ¹⁶, N. P. HATHI ¹³,
S. HEMMATI ²², G. C. JONES ^{23,24}, Y. KHUSANOVA ^{7,25}, F. LOIACONO ^{18,16}, F. POZZI ¹⁸, M. TALIA ^{18,16},
L. A. M. TASCA ⁷, D. A. RIECHERS ^{26,25}, G. RODIGHIERO ^{5,6}, M. ROMANO ⁵, N. SCOVILLE ²⁷, S. TOFT ^{8,9},
L. VALLINI ²⁸, D. VERGANI ¹⁶, G. ZAMORANI ¹⁶ AND E. ZUCCA ¹⁶

¹*IPAC, M/C 314-6, California Institute of Technology, 1200 East California Boulevard, Pasadena, CA 91125, USA*

²*Observatoire de Genève, Université de Genève, 51 Ch. des Maillettes, 1290 Versoix, Switzerland*

³*Institut de Recherche en Astrophysique et Planétologie – IRAP, CNRS, Université de Toulouse, UPS-OMP, 14, avenue E. Belin, F31400 Toulouse, France*

⁴*Department of Physics, University of California, Davis, One Shields Ave., Davis, CA 95616, USA*

⁵*Dipartimento di Fisica e Astronomia, Università di Padova, vicolo dell'Osservatorio, 3 I-35122 Padova, Italy*

⁶*INAF, Osservatorio Astronomico di Padova, vicolo dell'Osservatorio 5, I-35122 Padova, Italy*

⁷*Aix Marseille Université, CNRS, LAM (Laboratoire d'Astrophysique de Marseille) UMR 7326, 13388, Marseille, France*

⁸*The Cosmic Dawn Center, University of Copenhagen, Vibenshuset, Lyngbyvej 2, DK-2100 Copenhagen, Denmark*

⁹*Niels Bohr Institute, University of Copenhagen, Lyngbyvej 2, DK-2100 Copenhagen, Denmark*

¹⁰*Kavli Institute for the Physics and Mathematics of the Universe, The University of Tokyo, Kashiwa, Japan 277-8583 (Kavli IPMU, WPI)*

¹¹*Department of Astronomy, School of Science, The University of Tokyo, 7-3-1 Hongo, Bunkyo, Tokyo 113-0033, Japan*

¹²*The Caltech Optical Observatories, California Institute of Technology, Pasadena, CA 91125, USA*

¹³*Space Telescope Science Institute, 3700 San Martin Drive, Baltimore, MD 21218, USA*

¹⁴*Instituto de Investigación Multidisciplinar en Ciencia y Tecnología, Universidad de La Serena, Raúl Bitrán 1305, La Serena, Chile*

¹⁵*Departamento de Astronomía, Universidad de La Serena, Av. Juan Cisternas 1200 Norte, La Serena, Chile*

¹⁶*INAF - Osservatorio di Astrofisica e Scienza dello Spazio di Bologna, via Gobetti 93/3, I-40129, Bologna, Italy*

¹⁷*Centro de Astronomía (CITEVA), Universidad de Antofagasta, Avenida Angamos 601, Antofagasta, Chile*

¹⁸*Università di Bologna - Dipartimento di Fisica e Astronomia, Via Gobetti 93/2 - I-40129, Bologna, Italy*

¹⁹*INAF - Osservatorio Astrofisico di Arcetri, Largo E. Fermi 5, I-50125, Firenze, Italy*

²⁰*Research Institute for Science and Engineering, Waseda University, 3-4-1 Okubo, Shinjuku, Tokyo 169-8555, Japan*

²¹*National Astronomical Observatory of Japan, 2-21-1, Osawa, Mitaka, Tokyo, Japan*

²²*Jet Propulsion Laboratory, California Institute of Technology, Pasadena, CA 91109, USA*

²³*Cavendish Laboratory, University of Cambridge, 19 J. J. Thomson Ave., Cambridge CB3 0HE, UK*

²⁴*Kavli Institute for Cosmology, University of Cambridge, Madingley Road, Cambridge CB3 0HA, UK*

²⁵*Max-Planck-Institut für Astronomie, Königstuhl 17, D-69117 Heidelberg, Germany*

²⁶*Department of Astronomy, Cornell University, Space Sciences Building, Ithaca, NY 14853, USA*

²⁷*California Institute of Technology, MC 249-17, 1200 East California Boulevard, Pasadena, CA 91125, USA*

²⁸*Leiden Observatory, Leiden University, PO Box 9500, 2300 RA Leiden, The Netherlands*

Submitted to ApJS

ABSTRACT

We present the ancillary data and basic physical measurements for the galaxies in the *ALMA Large Program to Investigate C⁺ at Early Times (ALPINE)* survey – the first large multi-wavelength survey which aims at characterizing the gas and dust properties of 118 main-sequence galaxies at redshifts

$4.4 < z < 5.9$ via the measurement of [C II] emission at $158 \mu\text{m}$ and the surrounding far-infrared (FIR) continuum in conjunction with a wealth of optical and near-infrared data. We outline in detail the spectroscopic data and selection of the galaxies as well as the ground- and space-based imaging products. In addition, we provide several basic measurements including stellar masses, star formation rates (SFR), rest-frame ultra-violet (UV) luminosities, UV continuum slopes (β), and absorption line redshifts, as well as $\text{H}\alpha$ emission derived from Spitzer colors. Overall, we find that the *ALPINE* sample is representative of the $4 < z < 6$ galaxy population and only slightly biased towards bluer colors ($\Delta\beta \sim 0.2$). Using [C II] as tracer of the systemic redshift (confirmed for one galaxy at $z = 4.5$ for which we obtained optical [O II] $\lambda 3727 \mu\text{m}$ emission), we confirm red shifted Ly α emission and blue shifted absorption lines similar to findings at lower redshifts. By stacking the rest-frame UV spectra in the [C II] rest-frame we find that the absorption lines in galaxies with high specific SFR are more blue shifted, which could be indicative of stronger winds and outflows.

Keywords: galaxies: evolution — galaxies: fundamental parameters — galaxies: ISM — galaxies: star formation — galaxies: photometry

1. INTRODUCTION

1.1. *The Early Growth Phase in Galaxy Evolution*

Galaxy evolution undergoes several important phases such as the ionization of neutral Hydrogen at redshifts $z > 6$ (also known as the Epoch of Reionization) as well as a time of highest cosmic star-formation rate (SFR) density at $z \sim 2 - 3$. The transition phase at $z = 4 - 6$ (a time roughly 0.9 to 1.5 billion years after the Big Bang), often referred to as the *early growth phase*, is currently in focus of many studies. This time is of great interest for understanding galaxy evolution as it connects primordial galaxy formation during the Epoch of Reionization with mature galaxy growth at and after the peak of cosmic SFR density. During a time of only 600 Myrs, the cosmic stellar mass density in the universe increased by one order of magnitude (Caputi et al. 2011; Davidzon et al. 2017), galaxies underwent a critical morphological transformation to build up their disk and bulge structures (Gnedin et al. 1999; Bournaud et al. 2007; Agertz et al. 2009), and their interstellar medium (ISM) became enriched with metal from sub-solar to solar amounts (Ando et al. 2007; Faisst et al. 2016a), while at the same time the dust attenuation of the UV light significantly increased (Finkelstein et al. 2012; Bouwens et al. 2015; Fudamoto et al. 2017; Popping et al. 2017; Cullen et al. 2018; Ma et al. 2019; Yamanaka & Yamada 2019). Furthermore, the most massive of these galaxies may become the first quiescent galaxies already at $z > 4$ (Glazebrook et al. 2017; Valentino et al. 2019; Tanaka et al. 2019; Stockmann et al. in prep.; Faisst et al. 2019). All this put together, makes the early growth phase an important puzzle piece to be studied in order to decipher how galaxies formed and evolved to become the galaxies (either star forming or quiescent) that we observe in the local universe.

It is evident from studies at lower redshift that multi-wavelength observations are crucial for us to be able to form a coherent picture of galaxy evolution. To capture several important properties of galaxies, a *panchromatic* survey must comprise several spectroscopic and imaging datasets that cover a large fraction of the wavelength range of a galaxy’s light emission, including (i) the rest-frame ultra-violet (UV) containing Ly α emission, as well as several absorption lines to study stellar winds and metallicity (Heckman et al. 1997; Maraston et al. 2009; Steidel et al. 2010; Faisst et al. 2016a), (ii) the rest-frame optical containing tracers of age (Balmer break) as well as important emission lines (e.g., $\text{H}\alpha$) to quantify the star-formation and gas metal properties (Kennicutt 1998; Kewley & Ellison 2008), and (iii) the far-infrared (FIR) continuum and several FIR emission lines (e.g., [C II] $\lambda 158 \mu\text{m}$ or [N II] $\lambda 205 \mu\text{m}$) that provide insights into the gas and dust properties of galaxies (De Looze et al. 2014; Pavesi et al. 2019).

Fortunately, the early growth phase at redshifts $z = 4 - 6$ is at the same time the highest redshift epoch at which, using current technologies, such a panchromatic study can be carried out. The rest-frame UV part of the energy distribution at these redshifts has been probed in the past thanks to several large spectroscopic (Le Fèvre et al. 2015; Hasinger et al. 2018) and imaging (Capak et al. 2007; McCracken et al. 2012; Aihara et al. 2019) surveys from the ground as well as imaging surveys with the Hubble Space Telescope (HST, Grogin et al. 2011; Koekemoer et al. 2011; Scoville et al. 2007a). In addition, $\text{H}\alpha$ has been accessed successfully through observations with the Spitzer Space Telescope (Stark et al. 2013; de Barros et al. 2014; Smit et al. 2014; Rasappu et al. 2016; Smit et al. 2016; Faisst et al. 2016a, 2019; Lam et al. 2019). However, the FIR of $z > 4$ galaxies has only been probed sparsely in the past in less than

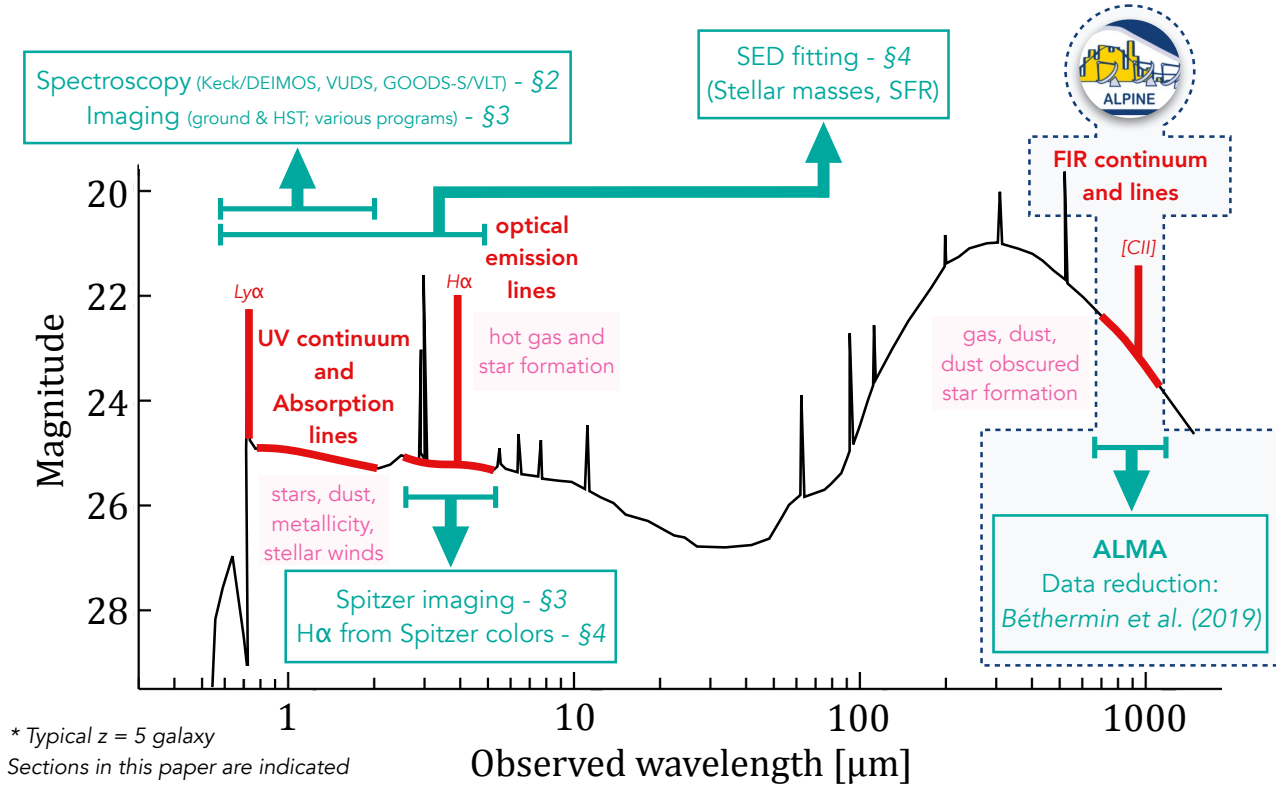
Layout of Current Data Products for *ALPINE* Galaxies

Figure 1. *ALPINE* builds the corner stone of a panchromatic survey at $z = 4 - 6$. The diagram shows the multi-wavelength data products that are currently available for all the *ALPINE* galaxies. The currently covered parts of the spectrum are indicated in red. The numbers link to sections in this paper where the data products and their analysis are explained in detail. The spectrum sketch is based on a typical $z = 5$ galaxy (adapted from Harikane et al. 2018).

a dozen galaxies using the *Atacama Large (Sub-) Millimeter Array* (ALMA, Riechers et al. 2014; Capak et al. 2015; Willott et al. 2015; Carniani et al. 2018). Commonly targeted by these observations is singly ionized Carbon (C^+) at $158 \mu\text{m}$, which is an important coolant for the gas in galaxies and is therefore broadly related to star formation activity and gas masses (Stacey et al. 1991; Carilli & Walter 2013; De Looze et al. 2014). The [CII] emission line is one of the strongest in the FIR and is in addition conveniently located in the ALMA Band 7 at redshifts $z = 4 - 6$ at one of the highest atmospheric transmissions compared to other FIR lines (see, e.g., Faisst et al. 2017). The origin of [CII] emission is still debated. In addition to photo-dissociation regions (PDRs) and the cold neutral medium, a significant fraction can also originate from ionized gas regions or CO-dark molecular clouds (Pineda et al. 2013; Vallini et al. 2015; Pavese et al. 2016). Also, the increasing temperature of the Cosmic Microwave Background (CMB) has an effect on the relation between [CII] and star formation (Ferrara et al. 2019). Both potentially complicates

the interpretation of [CII] as SFR indicator at high redshifts. Similar to $H\alpha$, [CII] traces the gas kinematics in a galaxy and is therefore an important component to quantify rotation- and dispersion-dominated systems as well as outflows (Jones et al. 2017; Pavese et al. 2018; Kohandel et al. 2019; Ginolfi et al. 2019).

The FIR landscape has dramatically changed with the completion of the *ALMA Large Program to Investigate C^+ at Early Times* (*ALPINE*, #2017.1.00428.L). *ALPINE* is laying the ground work for the exploration of gas and dust properties in 118 *main-sequence* star-forming galaxies in the early growth phase at $4.4 < z < 5.9$ and herewith started the first panchromatic survey of its kind at these redshifts.

1.2. *ALPINE* in a Nutshell

In the following, we summarize the scope of the *ALPINE* survey, we refer to Le Fèvre et al. (2019) for a broader overview of the program. *ALPINE* is a 69 hour large ALMA program started in Cycle 5 in May 2018 and completed during Cycle 6 in February 2019.

In total, 118 galaxies have been observed in Band 7 (covering [C II] emission at $158\ \mu\text{m}$ and its nearby continuum) at a spatial resolution of $< 1.0''$ and with integration times ~ 30 minutes on-source depending on their predicted [C II] flux. The galaxies originate from two fields, namely the *Cosmic Evolution Survey* field (COSMOS, 105 galaxies, [Scoville et al. 2007b](#)) and the *Extended Chandra Deep Field South* (ECDFS, 13 galaxies, [Giacconi et al. 2002](#)). Due to gaps in the transition through the atmosphere, the galaxies are split in two different redshift ranges spanning $4.40 < z < 4.65$ and $5.05 < z < 5.90$ with medians of $\langle z \rangle = 4.5$ and 5.5 , respectively. All galaxies are spectroscopically confirmed by either Ly α emission or rest-UV absorption lines and are selected to be brighter than an absolute UV magnitude of $M_{1500} = -20.2$. This limit is roughly equivalent to a SFR cut at $10\ M_{\odot}\ \text{yr}^{-1}$ and corresponds roughly to a limiting luminosity in [C II] emission of $L_{[\text{CII}]} = 1.2_{-0.9}^{+1.9} \times 10^8 L_{\odot}$ (assuming the relation derived by [De Looze et al. 2014](#)). Assuming a 3.5σ detection limit, the [C II] detection rate is 64% and continuum emission is detected in 19% of the galaxies.

The main science goals enabled by *ALPINE* are diverse and cover many crucial research topics at high redshifts:

- connecting [C II] to star-formation at high redshifts,
- coherent study of the total SFR density at $z > 4$ including the contribution of dust-obscured star formation,
- study of gas dynamics and merger statistics from [C II] kinematics and quantification of UV-faint companion galaxies,
- study of gas fractions and dust properties at $z > 4$,
- the first characterization of ISM properties using $L_{\text{FIR}}/L_{\text{UV}}$ and [C II]/FIR continuum diagnostics for a large sample at $z > 4$,
- quantifying outflows and feedback processes in $z > 4$ galaxies from [C II] line profiles.

Note that *ALPINE* provides at the same time the equivalent of a blind-survey of approximately 25 square-arcminutes. This enables us to estimate the obscured fraction of star-formation (mostly below $z = 4$) by finding UV-faint galaxies with FIR continuum or [C II] emission. The serendipitous continuum sources and [C II] detections are discussed in detail in [Bethérmin et al. \(in prep.\)](#) and [Loiacono et al. \(in prep.\)](#). A more detailed description of these science goals can be found in our survey overview paper ([Le Fèvre et al. 2019](#)).

ALPINE is based on a rich set of ancillary data, which makes it the first panchromatic survey at these high redshifts including imaging and spectroscopic observations

at FIR wavelengths (see Figure 1). The backbone for a successful selection of galaxies are rest-frame UV spectroscopic observations from the Keck telescope in Hawaii as well as the European *Very Large Telescope* (VLT) in Chile. These are complemented by ground-based imaging observations from rest-frame UV to optical, HST observations in the rest-frame UV, and Spitzer coverage above the Balmer break at rest-frame $4000\ \text{\AA}$. The latter is crucial for the robust measurement of stellar masses at these redshifts (e.g., [Faisst et al. 2016b](#)).

For a survey overview of *ALPINE* see [Le Fèvre et al. \(2019\)](#) and for details on the data analysis see [Bethérmin et al. \(in prep.\)](#). In this paper, we present these valuable ancillary data products and detail several basic measurements for the *ALPINE* galaxies. The outline of the paper is sketched in Figure 1. Specifically, in Section 2, we present the spectroscopic data and detail the spectroscopic selection of the *ALPINE* galaxies. In the same section, we also present stacked spectra and touch on velocity offsets between Ly α , [C II], and absorption line redshifts. Section 3 is devoted to the photometric data products, which include ground- and space-based photometry. In Section 4.1, we detail the derivation of several galaxy properties from the observed photometry. These include stellar masses, SFRs, UV luminosities, UV continuum slopes, as well as H α emission derived from Spitzer colors. We conclude and summarize in Section 5. All presented data products are available in the online printed version of this paper¹. The different catalogs and their columns are described in detail in the Appendix A. HST cutouts and rest-frame UV spectra for each of the *ALPINE* galaxies are shown in Appendix B.

Throughout the paper we assume the Λ CDM cosmology with $H_0 = 70\ \text{km s}^{-1}\ \text{Mpc}^{-1}$, $\Omega_{\Lambda} = 0.70$, and $\Omega_{\text{m}} = 0.30$. All magnitudes are given in the AB system ([Oke 1974](#)) and stellar masses and SFRs are normalized to a [Chabrier \(2003\)](#) initial mass function (IMF).

2. SPECTROSCOPIC DATA AND SELECTION

2.1. Spectroscopic selection of *ALPINE* galaxies

The *ALPINE* survey is only possible due to a spectroscopic pre-selection of galaxies from large spectroscopic surveys on COSMOS and ECDFS. This is because the ALMA frequency bands are narrow ($\sim 1000\ \text{km s}^{-1}$), and in order to observe [C II] emission the redshift has to be known within a precision of $\sim 1000\ \text{km/s}$. The galaxy selection is refined to optimize the efficiency of

¹ [This link will be available in the accepted version of this paper]

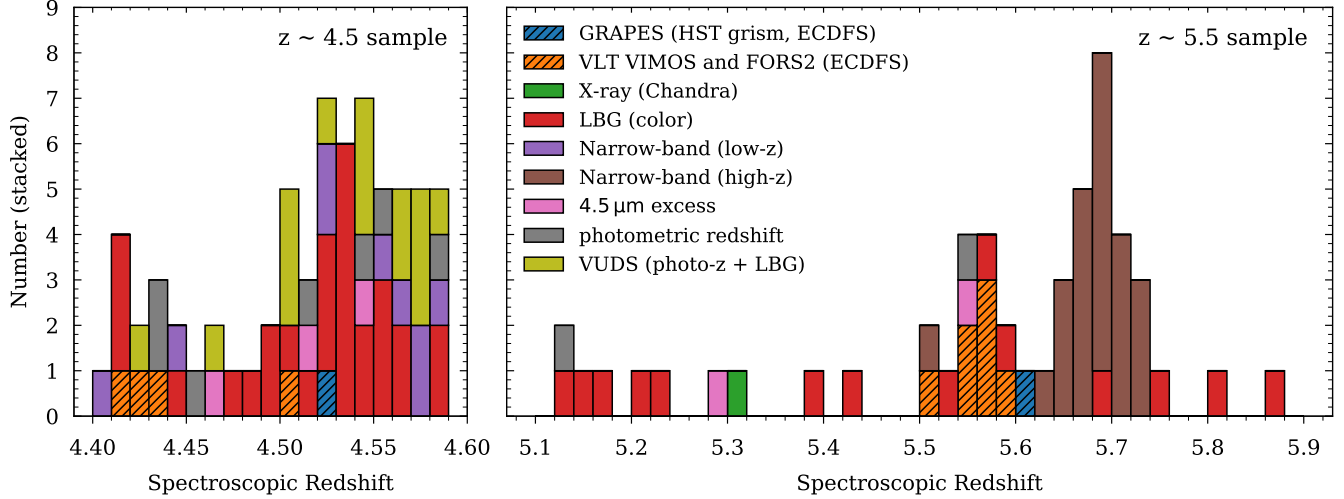


Figure 2. Redshift distribution of *ALPINE* galaxies. Each bar shows the stacked number of different selections per bin (see Table 1 and description in text). The bins with galaxies from the ECDFS field are hatched. The left and right panels show galaxies in the two different redshift bins.

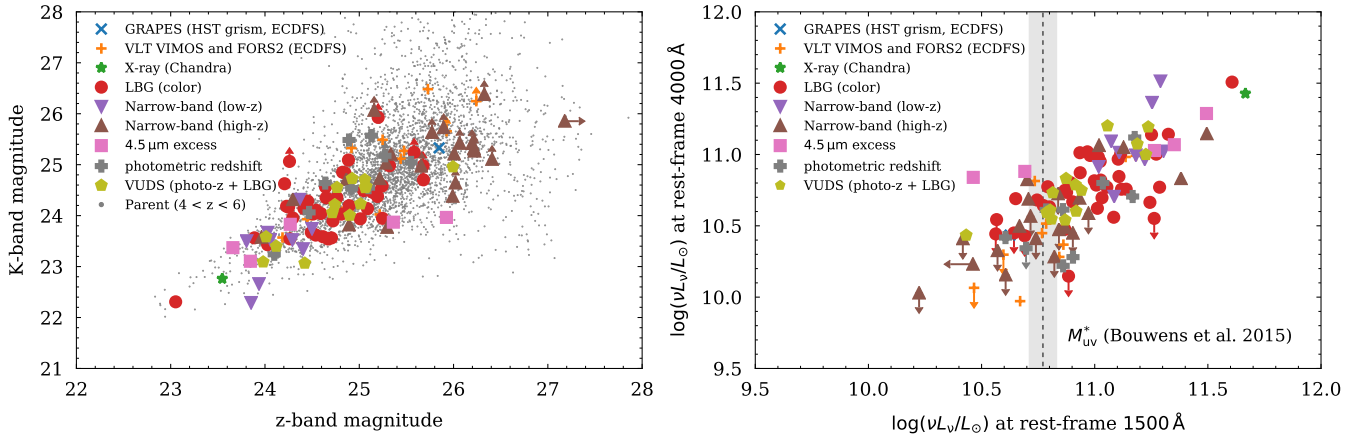


Figure 3. Comparison of observed (i.e., not corrected for dust) z -band and K -band magnitudes (left) and luminosities (right) for different selections listed in Table 1. The measurements on the parent sample in COSMOS at $4 < z < 6$ is shown in light gray. The color-coding is the same as in Figure 2. The arrows show 1σ upper limits. The gray area denotes the M_{UV}^* , the knee of the UV luminosity function, which corresponds to -21.1 ± 0.15 (or $\log(\nu L_\nu/L_\odot) \sim 10.77$) at $z = 5$ (Bouwens et al. 2015). The derivation of the photometry is described in detail in Section 3.

the ALMA observations by creating groups of galaxies in spectral dimensions. Our sample also includes 7 galaxies that were previously observed with ALMA by Riechers et al. (2014) and Capak et al. (2015). These are *HZ1*, *HZ2*, *HZ3*, *HZ4*, *HZ5*, *HZ6/LBG-1*, and *HZ8*, which correspond to the *ALPINE* galaxies *DC_536534*, *DC_417567*, *DC_683613*, *DC_494057*, *DC_845652*, *DC_848185*, and *DC_873321*, respectively. Furthermore, four galaxies from the VUDS survey (*vc_5101288969*, *vc_5100822662*, and *vc_510786441* in COSMOS and *ve_530029038* in ECDFS) are observed twice (resulting in a total number of 122 observations). The duplicate observations are used for quality assess-

ment. Bethermin et al. (in prep.) describes the combination of these observations.

The rest-frame UV spectroscopic data from which the *ALPINE* sample is selected combine various large surveys on the COSMOS and ECDFS fields. Out of the 105 *ALPINE* galaxies on the COSMOS field, 84 are obtained by the large DEIMOS spectroscopic survey (Capak et al. 2004; Mallery et al. 2012; Hasinger et al. 2018) at the Keck telescope in Hawaii. The remaining spectra on the COSMOS field are obtained from the VIMOS Ultra Deep Survey (VUDS, Le Fèvre et al. 2015; Tasca et al. 2017) at the VLT in Chile. In total 6 of the VUDS spectra are inde-

Table 1. Spectroscopy and selection of *ALPINE* galaxies

| Survey | Selection | Number | Ref. |
|------------------------------------|---|-----------------|------|
| COSMOS field (105 galaxies) | | | |
| <i>Keck/DEIMOS</i> [†] | narrow-band ($z \sim 4.5$) ^a | 6 | 1 |
| | narrow-band ($z \sim 5.7$) ^b | 23 | |
| | LBG (color) ^c | 41 | |
| | pure photo- z ^d | 9 | |
| | 4.5 μm excess | 4 | |
| | X-ray (Chandra) | 1 | |
| | with Ly α emission | 66 | |
| | weak Ly α emission or absorption | 18 | |
| <i>VUDS</i> | photo- z + LBG | 21 | 2 |
| | [narrow-band ($z \sim 4.5$) | 3] [‡] | |
| | [narrow-band ($z \sim 5.7$) | 1] [‡] | |
| | [LBG (color) | 1] [‡] | |
| | [4.5 μm excess | 1] [‡] | |
| | with Ly α emission | 16 | |
| | weak Ly α emission or absorption | 5 | |
| | ECDFS field (13 galaxies) | | |
| <i>VLT GOODS-S</i> | primarily LBG (color) | 11 | 3 |
| | total with Ly α emission | 6 | |
| | total without Ly α emission | 5 | |
| <i>HST/GRAPES</i> | Grism (no <i>a priori</i> selection) | 2 | 4 |
| | with Ly α emission | 2 | |
| | weak Ly α emission or absorption | 0 | |

[†] For a detailed description of the selection criteria, we refer to Mallery et al. (2012) and Hasinger et al. (2018).

[‡] Six of these galaxies are also observed as part of the Keck/DEIMOS survey (ref. 1). The corresponding number per selection from the Keck/DEIMOS program is given in square-brackets for those six galaxies.

^a Ly α emitters selected with *NB711*.

^b Ly α emitters selected with *NB814*.

^c Color-selected galaxies in B , g^+ , V , r^+ , and z^{++} using the criteria from Ouchi et al. (2004); Capak et al. (2004, 2011); Iwata et al. (2003); Hildebrandt et al. (2009).

^d Galaxies with a photometric redshift $z > 4$ with a probability of $> 50\%$ based on the Ilbert et al. (2010) photo- z catalog.

References: (1) Capak et al. (2004); Mallery et al. (2012); Hasinger et al. (2018), (2) Le Fèvre et al. (2015), (3) Vanzella et al. (2007, 2008); Balestra et al. (2010), (4) Malhotra et al. (2005); Rhoads et al. (2009)

pendently also observed as part of the Keck/DEIMOS survey (*vc_5100559223*, *vc_5100822662*, *vc_5101218326*, *vc_5101244930*, *vc_5101288969*, *vc_510786441*). The redshifts are consistent within 280 km s^{-1} and we do not find any systematic offsets between the two observations (see also Section 2.4.1). Out of the 13 galaxies in the ECDFS field, 11 are obtained from spectroscopic observations with VIMOS (9) and FORS2

(2²) at the VLT (Vanzella et al. 2007, 2008; Balestra et al. 2010), and 2 come from the HST grism survey *GRAPES* (Malhotra et al. 2005; Rhoads et al. 2009). The spectral resolution of the different dataset varies between $R \sim 100$ (ECDFS/*GRAPES* grism), $R \sim 180$ (ECDFS/VIMOS), $R \sim 230$ (COSMOS/VUDS), $R \sim 660$ (ECDFS/FORS2), and $R \sim 2500$ (COSMOS/DEIMOS).

Biases towards dust-poor star-forming galaxies with strong rest-frame UV emission lines (such as Ly α) can be common in purely spectroscopically selected samples. To minimize such biases as much as possible, the spectroscopically observed galaxies have been pre-selected through a variety of different selection methods. The largest fraction of galaxies in *ALPINE* is drawn from the Keck/DEIMOS and VUDS surveys on the COSMOS field. Both surveys include galaxies preselected in various ways, resulting in the most representative and inclusive spectroscopic high-redshift galaxy sample. Specifically, the VUDS survey combines predominantly a photometric redshift selection with a color-selected Lyman Break Galaxy (LBG) selection (Le Fèvre et al. 2015), known as the Lyman-break drop-out technique (see, e.g., Steidel et al. 1996; Dickinson 1998). The Keck/DEIMOS survey (providing 71% of the total *ALPINE* sample) consists of galaxies that are selected by narrow-band surveys at $z \sim 4.5$ (7%) and $z \sim 5.7$ (27%), the drop-out technique (color selection) over the whole redshift range (49%), as well as purely by photometric redshifts (11%). In addition, 4 galaxies are selected by a 4.5 μm excess and one galaxy was preselected through X-ray emission using the Chandra observatory. On the ECDFS field, the galaxies are mostly color-selected. Table 1 summarizes the different selections and corresponding numbers of galaxies and provides a complete list of references. We also list the numbers of galaxies with Ly α emission (76%) and weak Ly α emission or Ly α absorption ($\sim 24\%$). Note that the Keck/DEIMOS and VUDS samples have similar Ly α emission properties. However, note that above $z = 5$, the *ALPINE* sample is strongly dominated by narrow-band selected galaxies.

Figure 2 shows the distribution of redshifts of the *ALPINE* galaxies in the COSMOS and ECDFS fields. The colored histogram bars show stacked numbers of galaxies that are preselected by the different methods discussed above. The bins with galaxies in the ECDFS field are hatched. The narrow-band selected galaxies are

² One of these galaxies, *vc_530029038*, has also been observed by the VUDS survey.

prominent at $z \sim 5.7$ and represent the largest fraction of galaxies at $z > 5$ in *ALPINE*. On the other hand, the $z < 5$ sample consists mostly of color-selected galaxies. The VUDS galaxies are most represented at $z < 5$, while the DEIMOS spectra and the galaxies in ECDFS cover the whole redshift range.

Figure 3 shows the distribution of observed magnitudes as well as rest-frame 1500 Å and ~ 4000 Å luminosity of galaxies selected by the different methods. The photometry that is used is explained in detail in Section 3. The 1500 Å rest-frame luminosity is derived from SED fitting (see Section 4.2 for details). The 4000 Å rest-frame luminosity is derived directly from the UltraVISTA K_s and VLT K_s^v magnitude for galaxies in the COSMOS and GOODS-S field, respectively. The magnitudes and luminosities are not corrected for dust attenuation. Note that the K -band is rest-frame 3000 Å at the highest redshifts ($z = 5.9$), hence at these redshift older and dustier galaxies would be biased to lower luminosities. As expected for spectroscopically selected galaxies, the *ALPINE* sample covers the brighter part of the galaxy magnitude and luminosity distribution. The different selection methods on their own are distributed differently in this parameter space. Most noticeably, the $z \sim 5.7$ narrow-band selected galaxies reside at the faintest luminosities, while the $4.5 \mu\text{m}$ continuum excess selected galaxies are among the brightest. The X-ray Chandra detected galaxy *DC.845652* (green star) at $z = 5.3$ outshines all of the galaxies in UV luminosity.

All in all, although naturally biased to the brightest galaxies, this diverse selection function makes *ALPINE* an exemplary panchromatic survey that enables the study of a representative high- z galaxy sample at UV, optical, and FIR wavelengths.

2.2. Uniform calibration of spectra

All of the rest-frame UV spectra discussed in Section 2.1 are relative flux corrected to remove sensitivity variations across the spectrograph as well as to correct atmospheric absorption features. However, not all of the spectra have been absolute flux calibrated. Hence, we recalibrate the spectra using the Galactic extinction corrected total broad, intermediate, and narrow-band photometry of the *ALPINE* galaxies (see Section 3 for details on the photometry). It turns out that the absolute flux calibrated spectra are in excellent agreement with our measured photometry and the recalibration is negligible in these cases. As the spectra come from different surveys, we convert them to a common format during the recalibration procedure.

To perform the absolute flux calibration, we convolve each of the spectra with the transmission functions of

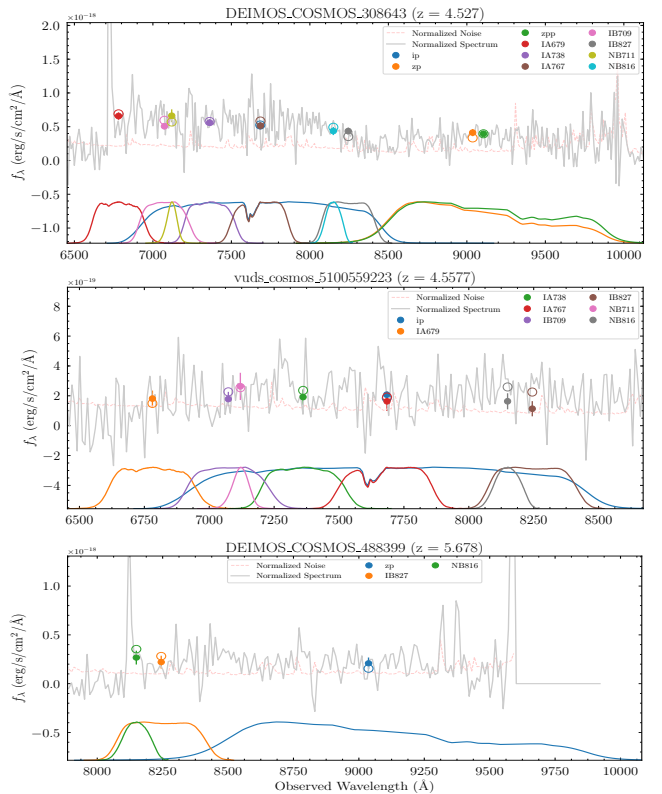


Figure 4. Absolute calibration of rest-frame UV spectra. Shown are three examples at $z = 4.53$, $z = 4.56$, and $z = 5.68$. The spectra are convolved by the filters and the photometry (open circles) is compared to the total and Galactic extinction corrected broad, intermediate, and narrow-band photometry from catalogs (filled circles) described in Section 3.

the various optical broad, intermediate, and narrow-band filters that exist on the COSMOS and ECDFS fields, respectively. On average, we use 4 – 9 filters for galaxies at $z < 5$ and 2 – 4 at $z > 5$. If the filter extends further than the spectrum, we extrapolate the spectrum by its medium continuum value. If the filter extends significantly beyond the spectrum ($> 50\%$), we do not consider the filter. We then compare the photometry obtained from the spectra to the total and Galactic extinction corrected photometry discussed in Section 3, which allows us to obtain an average correction factor for each spectrum. We found that a single number for this correction is enough for the calibration as the spectra already have been relative flux calibrated. Our recalibration corrects for slit-losses and seeing variations. We also scale the variance in order to conserve the S/N of the spectrum. Note that we do not consider undetected spectroscopic fluxes in this procedure, however, we use the constraints gained from the upper limits in the photometry for the calibration. Figure 4 shows three absolute calibrated spectra at $z \sim 4.53$, $z \sim 4.56$ (with

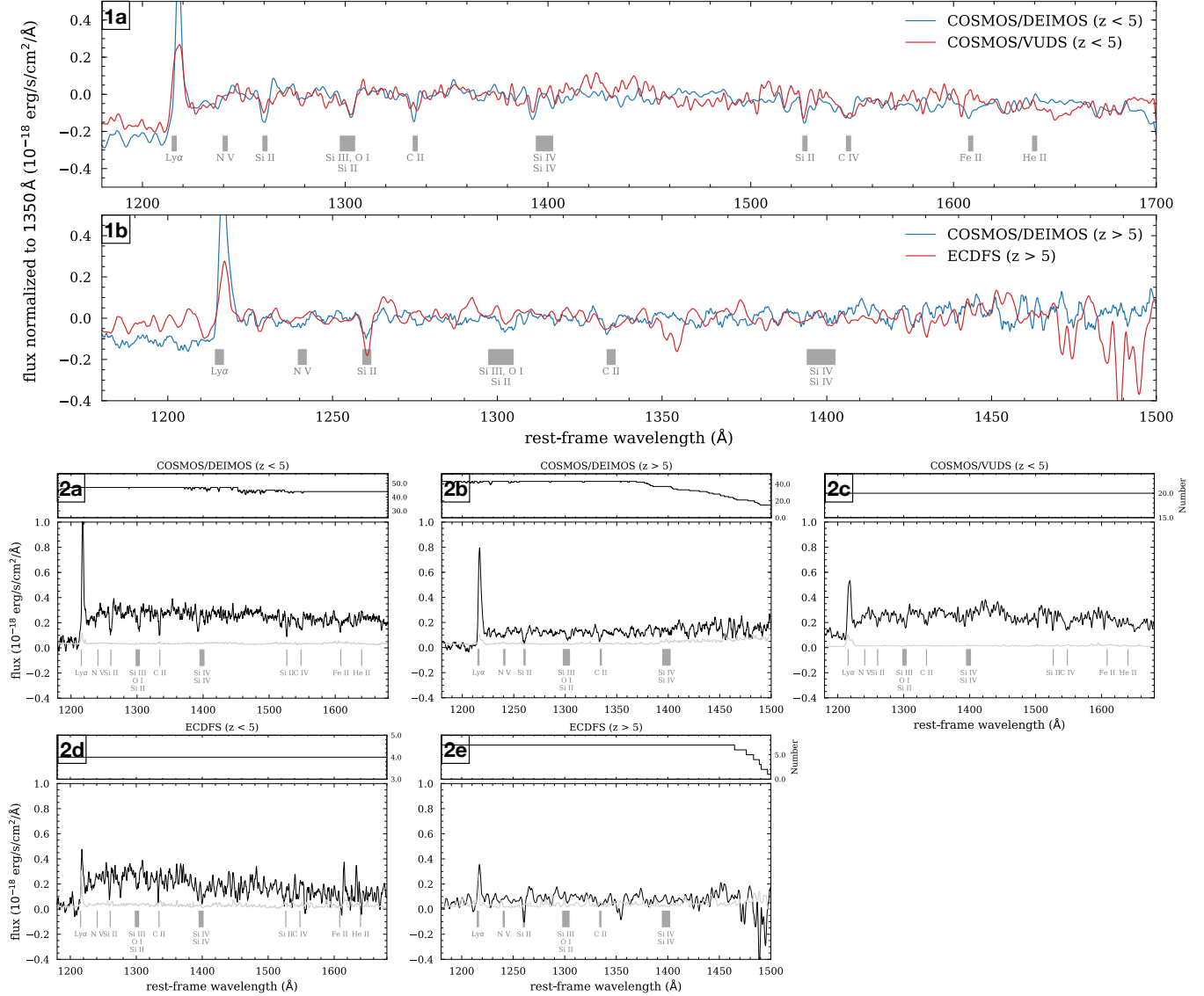


Figure 5. Examples of stacked *ALPINE* spectra. Panels 1a and 1b show stacked spectra at $z < 5$ (in COSMOS from DEIMOS observations and as part of the VUDS survey) and $z > 5$ (on COSMOS from DEIMOS and on ECDFS from VIMOS and FORS2 observations), respectively. The stacks are all normalized to the continuum between 1300 Å and 1400 Å and common emission and absorption features are indicated with gray bars. Note that the VUDS spectra have a lower native resolution ($R \sim 230$) compared to the DEIMOS observations ($R \sim 2500$), therefore the latter have been degraded in resolution using a 1-dimensional Gaussian window function for visual comparison. Panels 2a through 2e show stacks at $z < 5$ and $z > 5$ for the different datasets. The number of spectra included per wavelength is shown on the top of each panel. The uncertainties are indicated by the gray line as well as on the spectra with a light color. The y -axis scale is the same such that the continuum brightness can be compared.

weak Ly α), and $z \sim 5.68$ to visualize our method. The filters that were used for the calibration are indicated in colors.

2.3. Stacked Spectra: Overview over Rest-Frame UV Emission and Absorption Lines in *ALPINE* Galaxies

Figures 5 and 6, show stacks of different spectra. In order to create median-stacks of the spectra, we resam-

ple the spectra to a common wavelength grid and stack them in rest-frame using their respective redshifts derived from [C II] or, if not available, from rest-UV absorption lines or Ly α emission. All stacks are subsequently binned to a resolution of 2 Å for visual purposes to emphasize the UV absorption features. To obtain a per-pixel uncertainty from the sky background for each stack (visualize by the gray line), we simply combine the inverse variances in the individual spectra in quadrature.

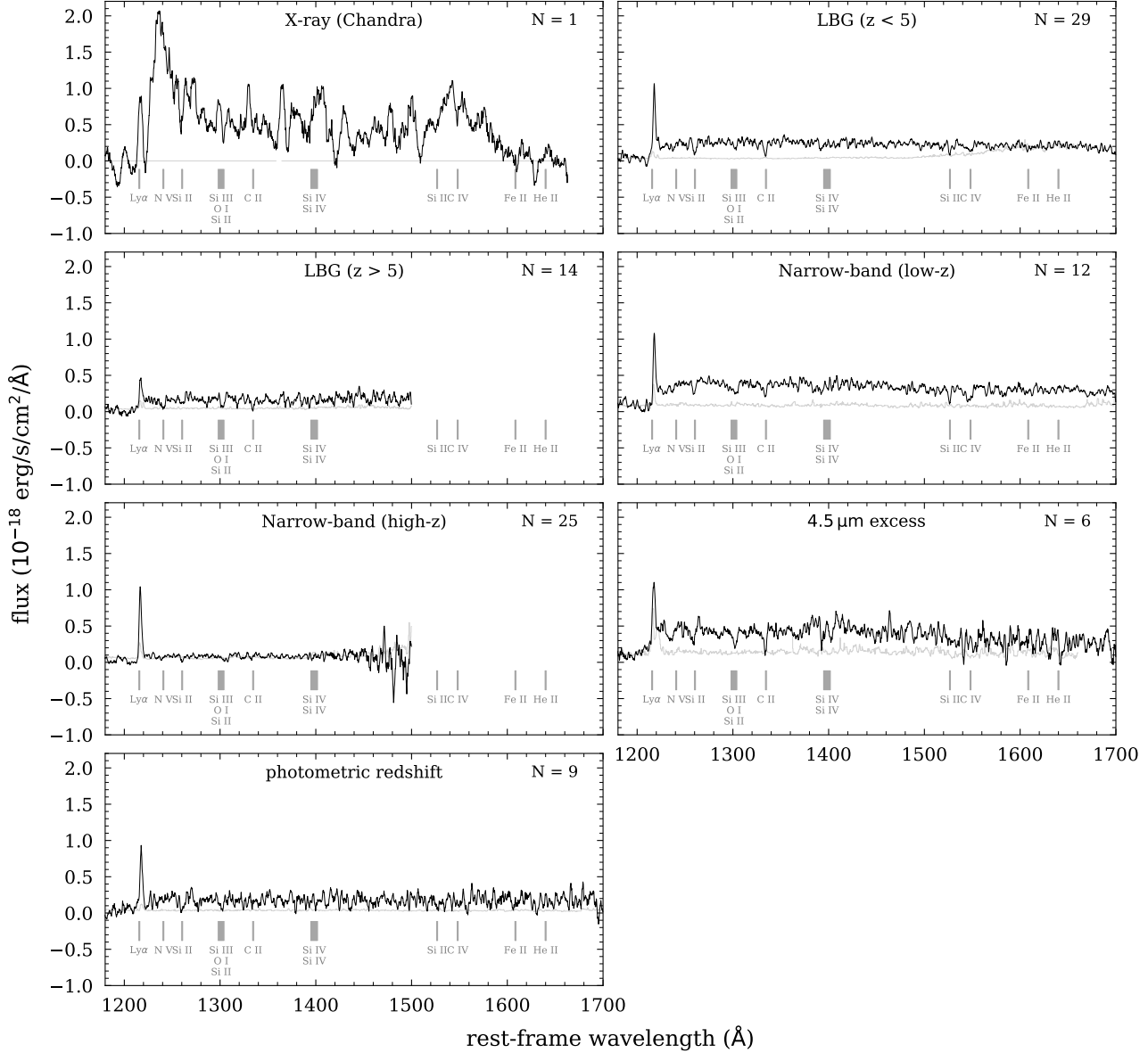


Figure 6. Stacked spectra in COSMOS for each of the selections discussed in Section 2.1 and listed in Table 1. Emission and absorption features are indicated by gray bars and the number of spectra in the stack is shown on the upper right corner. We also show the X-ray detected galaxy (*DC_845652*) at $z = 5.3$, which shows strong and broad N V and C IV emission.

The latter are the original inverse variance that we adjusted to the new normalization described in Section 2.2.

Panels 1a and 1b of Figure 5 compare the full stacked spectra of galaxies at $z < 5$ in COSMOS from observations with DEIMOS and as part of VUDS, as well as at $z > 5$ from observations in COSMOS from DEIMOS and in ECDFS from VIMOS and FORS2. In the former case, we adjust the resolution of the DEIMOS spectra ($R \sim 2500$) to that of the VUDS observations ($R \sim 230$) by applying a 1-dimensional Gaussian smoothing. The spectra are normalized to the median flux in the rest-frame wavelength range between 1300 and 1400 Å be-

fore stacking. For stacks of galaxies at $z > 5$, the rest-frame wavelength reaches up to 1500 Å, while for lower redshift stacks we show wavelengths up to rest-frame 1700 Å. Several prominent spectral features are visible in the stacks in both redshift bins (indicated by gray bars). These include the Ly α emission line and N V at 1241 Å and in addition UV absorption lines such as Si II at 1260 Å, the Si III-O I-Si II complex at 1301 Å, the two Si IV lines at 1398 Å, as well as Si II, C IV, and He II at 1527 Å, 1548 Å, and 1640 Å, respectively. Furthermore, we see indication of Fe II absorption at 1608 Å in the COSMOS/DEIMOS spectra stack at $z < 5$. The

depth of the UV absorption features are comparable for the different observations with the different instruments, verifying similar quality and little biases. However, note that the features in the ECDFS spectra are less pronounced due to the factor ~ 6 smaller number of spectra contributing to the stacks compared to the DEIMOS stacks. Panels 2a through 2e show the stacks for variously selected datasets below and above $z = 5$. The spectra are not normalized before stacking in these cases and the number of spectra per wavelength are shown on the top right for each panel. Note again that the number of high-redshift spectra drops towards redder wavelengths. This has to be kept in mind when analyzing the spectral features in the stacks. Emission and absorption lines are indicated as in the other panels. As expected, the stacked spectra at higher redshifts are fainter, but still significant UV absorption features are present (see also Faisst et al. 2016a; Pahl et al. 2019; Khusanova et al. 2019).

Figure 6 shows stacked spectra in COSMOS observed with DEIMOS for the different selection categories (see also Table 1 and Figure 2). We split the LBG category in galaxies below and above $z = 5$. All the spectra are smoothed with a Savitzky-Golay filter with size of 2 \AA for visualization purposes. The total number of spectra per stack is indicated in the upper left corner. All panels are scaled the same way to emphasize differences in brightness. The X-ray detected galaxy at $z = 5.3$ is UV bright compared to the other stacks and shows strong Nv emission with overlaid Si II absorption as well as broad C IV emission. LBGs (i.e., color-selected galaxies) are preferentially fainter but of similar continuum brightness as narrow-band selected galaxies at $z \sim 4.5$. The latter show significant C II, Si IV, and C IV absorption. As expected, narrow-band selected galaxies at $z \sim 5.7$ show strong Ly α emission and a faint continuum such that the S/N is too low to detect UV absorption features at great significance. The stack of galaxies selected by photometric redshifts shows to first order similar properties as the LBGs. The $4.5 \mu\text{m}$ -excess continuum selected galaxies are on average the continuum brightest galaxies and show significant Ly α emission as well as absorption features.

2.4. Rest-UV Emission and Absorption Lines and Velocity Offsets

2.4.1. Measurements

We measure basic quantities from the individual rest-frame UV spectra. These include the redshift and equivalent width of Ly α emission as well as redshifts from various absorption lines.

The Ly α redshift ($z_{\text{Ly}\alpha}$) is based on the peak of the (asymmetric) Ly α emission to allow a direct comparison with models of Ly α radiative transfer (see, e.g., Hashimoto et al. 2015). The Ly α flux is measured by fitting a Gaussian to the line and for measuring the equivalent width ($\sim f_{\text{line}}^{\text{tot}}/f_{\text{continuum}}$) the continuum redward of the Ly α line is used. These measurements are explained in more detail in Cassata et al. (2019, in prep.).

The absorption redshifts are measured for each individual spectrum, if possible, using the lines Si II (1260.4 \AA), O I (1302.2 \AA)³, C II (1334.5 \AA), Si IV (1393.8 \AA) and Si IV (1402.8 \AA), Si II (1526.7 \AA), and C IV (1549.5 \AA)⁴. The first four are covered by observations in all galaxies, while the coverage of the latter depends on the redshift of the galaxy. Note that some of the above lines are predominantly formed in the ISM (low-ionization interstellar [IS] lines; Si II, O I, C II, Si II), while others are formed in stellar winds (high-ionization wind lines; Si IV or C IV) and therefore can display strong velocity shifts (e.g., Castor & Lamers 1979; Leitherer et al. 2011). To increase the S/N of our measurements, we use all the above lines to derive an absorption line redshift (referred to as $z_{\text{IS+wind}}$), but we compare the individual redshift from the IS (z_{IS}) and wind (z_{wind}) lines to investigate potential systematic differences. Before performing any measurements, we subtract a continuum model from each individual spectrum. The model is derived by fitting a 4th-order polynomial to the spectrum, which is smoothed by a 5 \AA box kernel. We then fit the above absorption lines in five different rest-frame wavelength windows [1240 \AA , 1280 \AA], [1280 \AA , 1320 \AA], [1320 \AA , 1350 \AA], [1370 \AA , 1420 \AA], and [1500 \AA , 1570 \AA]. For the separate fit of the IS and wind lines, we split the last window into two ranges, namely [1510 \AA , 1540 \AA] and [1530 \AA , 1570 \AA] to separate the IS line Si II and the wind line C IV, respectively. The absorption lines can be significantly asymmetric due to stellar winds and the effect of optical depth. Fitting a single Gaussian to them could therefore bias the redshift measurements. Instead, we use the stacked spectrum of LBGs at $z \sim 3$ from Shapley et al. (2006) as a template, which we cross-correlate to the observed data within the wavelength range of a given window by χ^2 minimization. We let the redshift vary within a velocity range of $\pm 600 \text{ km s}^{-1}$ (corresponding to roughly 0.01 in redshift) around a prior absorption redshift, which is obtained by a manual cross-correlation of the same template to all

³ Here we refer to the O I absorption line complex consisting of Si III, C II, O I, and Si II.

⁴ This absorption consists of two lines (1548.2 \AA and 1550.8 \AA) and here we give the average wavelength.

possible absorption lines at once using the interacting redshift-fitting tool `SpecPro`⁵ (Masters & Capak 2011). We found that this approach significantly removes degeneracies in the fit and at the same time allows a visual inspection of all the spectra to flag the ones with low S/N where no reasonable fit can be obtained⁶. For each galaxy, the so obtained $\chi^2(z)$ distribution is then converted into a probability density function $p(z)$ for each of the windows. These are combined, by choosing the necessary absorption lines, to a total probability $P(z)$ from which the final absorption line redshifts ($z_{\text{IS+wind}}$, z_{wind} , or z_{IS}) are derived. The errors on these redshifts are derived by repeating this measurement 200 times, thereby perturbing the fluxes according to a Gaussian error distribution with σ defined by the average flux noise of the continuum. Typical uncertainties are on the order of $\pm 100 \text{ km s}^{-1}$.

As mentioned in Section 2.1, 6 galaxies in COSMOS have been observed by the Keck/DEIMOS and VUDS spectroscopic surveys. Therefore there are two measurements for each of these galaxies. Specifically, for *vc_5100559223*, *vc_5100822662*, *vc_5101218326*, and *vc_5101244930*, the IS+wind redshift measurements agree within 200 km s^{-1} , 280 km s^{-1} , 70 km s^{-1} , and 110 km s^{-1} . These values are on the order of the measurement uncertainties. Note that while the VUDS slits are oriented east-west, the DEIMOS slits can be oriented north-south or in any other angle. This different orientation could also be responsible for the differences in velocity offsets. On the other hand, for *vc_5101288969* and *vc_510786441*, we find significant differences of 1290 km s^{-1} and 1010 km s^{-1} . A close inspection of the spectra shows that these are very low in S/N. Also, both have low visual quality flags (-99 and 1 , indicating not robust measurements are possible) and their redshifts are fit with less than 3 lines, hence should not be trusted. For all 6 spectra we decided to prefer the VUDS observations because of their slightly better S/N at a cost of lower resolution.

2.4.2. Velocity Offsets with respect to [CII] FIR Redshifts

The detection of [CII] by ALMA provides the systemic redshift of a galaxy. This enables us to study velocity offsets of rest-frame UV absorption lines and Ly α emission that will inform further about the properties of the ISM in these galaxies similarly to studies at lower redshifts using H α and CII λ 1909 (e.g., Steidel et al. 2010;

⁵ <http://specpro.caltech.edu>

⁶ The value of this visual flag is -99 if the S/N is too low to obtain a redshift, and 1 and 2 for reliable and very reliable redshift measurements, respectively.

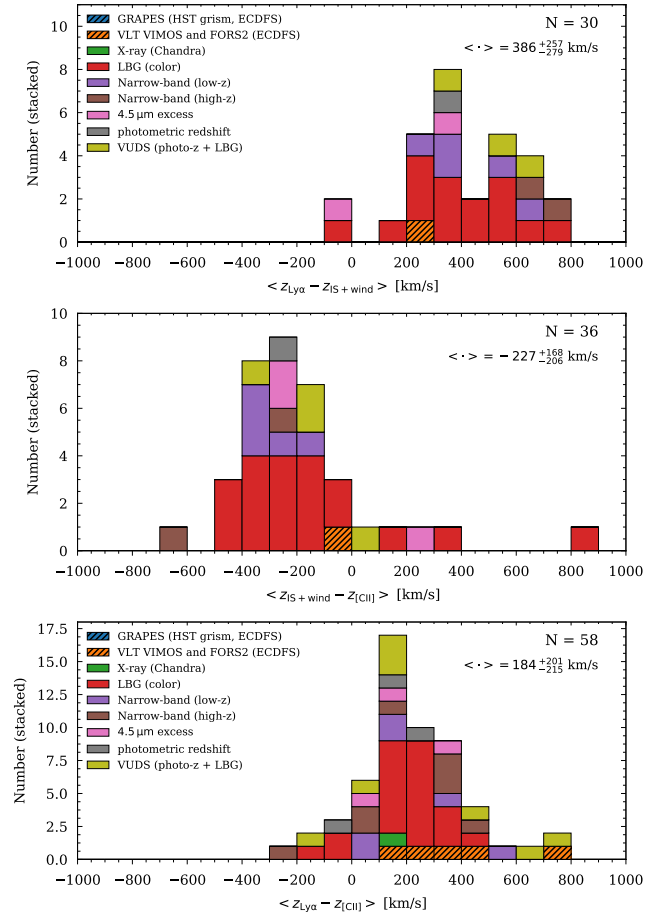


Figure 7. Stacked histograms of velocity offsets between redshifts derived from different spectral features. The number of galaxies and median of the distribution (including scatter) are indicated. Shown are the velocity offsets between Ly α emission and IS+wind absorption lines (*top panel*), as well as between Ly α , IS+wind, and systemic redshift (*middle and bottom panel*). The latter two are in detail discussed in a forthcoming paper (Cassata et al. 2019, *in prep.*). The average errors are on the order of $\pm 100 \text{ km s}^{-1}$, which corresponds to the size of the bins. We do not find any significant biases introduced by the different selection methods (color coded as in previous figures).

Marchi et al. 2019). Here we give an overview of the velocity properties and compare them for galaxies with high and low specific SFRs.

In the following, we define the velocity difference for two redshifts (z_1 and z_2) as $\langle z_1 - z_2 \rangle \equiv \Delta v_{12} = c \times (\frac{1+z_1}{1+z_2} - 1)$ where $c = 2.998 \times 10^5 \text{ km s}^{-1}$. The measurement of the [CII] redshifts are detailed in Bethermin et al. (*in prep.*). They are defined as the peak of a Gaussian fit to the [CII] line with spectral resolution of 25 km s^{-1} . The uncertainty of the redshift measurements was estimated by a Monte Carlo simulations with perturbed fluxes according to the error per spectral bin. The average uncertainty is roughly $50 - 60 \text{ km s}^{-1}$. For the

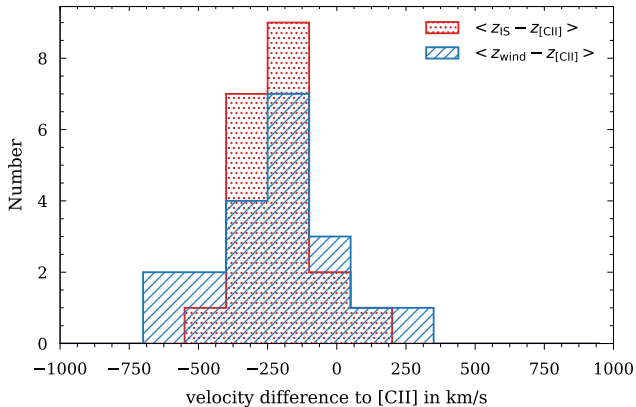


Figure 8. Histogram of velocity offset with respect to systemic (defined by the $[\text{CII}]\lambda 158\mu\text{m}$ redshift) for IS (red; O I, C II, and Si II) and stellar wind affected absorption lines (blue; Si IV and C IV). The average errors are on the order of $\sim 200 \text{ km s}^{-1}$, which corresponds to the size of the bins.

absorption lines, we require that $z_{\text{IS}+\text{wind}}$ is measured from at least three absorption lines and we only show galaxies that have not been flagged by our visual inspection with `SpecPro` as unreliable (flag -99). The average intrinsic measurement error per galaxy is $\pm 100 \text{ km s}^{-1}$. In relation to that, a systematic uncertainty of 0.5 \AA in the rest-frame wavelength of the absorption lines (e.g., due to calibration issues) turns into a velocity shift of $\sim 120 \text{ km s}^{-1}$.

Figure 7 shows stacked histograms of velocity differences. The number of galaxies used as well as the median of the distribution with scatter (*not* error on the median) are indicated as well. The upper panel compares the velocities measured from $\text{Ly}\alpha$ and the IS+wind absorption lines. We find a median offset on the order of 390 km s^{-1} , which is consistent with other measurements at the same redshifts (see, e.g., Faisst et al. 2016a; Pahl et al. 2019) as well as at $z \sim 2 - 3$ (Steidel et al. 2010). The center and bottom panels compare the IS+wind and $\text{Ly}\alpha$ redshifts to the systemic redshift (here defined as the $[\text{CII}]\lambda 158 \mu\text{m}$ redshift, Bethermin et al. in prep.). For the former we find an offset of -230 km s^{-1} and for the latter we find 180 km s^{-1} . These negative and positive velocity offsets can be related in a simple physical model involving the resonant scattering of $\text{Ly}\alpha$ photons and outflowing gas in the outskirts of galaxies (see detailed discussion in Steidel et al. 2010). The redshifted $\text{Ly}\alpha$ emission line (with respect to systemic) can be explained by resonant scattering of the $\text{Ly}\alpha$ photons. Preferentially, red-shifted $\text{Ly}\alpha$ photons scattered from the back of the galaxy can make it unscattered through the intervening gas inside the galaxy along the line of sight. The blueshift of IS absorption may depend on the outflow velocity of the absorbing gas as well as its covering

fraction (or optical depth) inside the galaxy along the line of sight towards the observer. For a more in-depth discussion we refer to a companion paper by Cassata et al. (2019, in prep.). Overall, we do not see a significant dependence of the velocity differences on the various selection techniques (color-coded in the figure).

Figure 8 compares the velocity offsets between IS (Si II, O I, C II, Si II) and wind (Si IV, C IV) lines. We require that at least three IS lines and one wind line is measured. In addition, only galaxies that pass our visual inspection are used. Overall, we do not see any statistical difference between IS and wind lines, although there is a tail towards higher blueshifts in the case of wind lines. However, wind and outflows may be increased in galaxies with high and spatially dense star formation and young stellar populations. Therefore we would expect different velocity shifts for the absorption lines with respect to the systemic redshift for highly star-forming galaxies. In Figure 9, we investigate this picture by stacking galaxies at the extreme ends of the sSFR distribution (we refer to Section 4 for details on the measurement of the physical properties of our galaxies), namely low ($< 4 \text{ Gyr}^{-1}$) and high ($> 5 \text{ Gyr}^{-1}$) sSFR, in their corresponding rest-frames defined by the systemic redshift (i.e., $[\text{CII}]\lambda 158\mu\text{m}$ redshift). The sSFR is a good proxy of the star-formation density in a galaxy as well as the age of the current stellar population (see, e.g., Cowie et al. 2011). We show the stacked spectra in five wavelength regions covering prominent absorption lines for each sSFR bin. The vertical dashed lines show the different absorption lines in the $[\text{CII}]$ rest-frame. First, we verify that the shifts between IS and wind lines are very similar for each sSFR bin (in concordance with Figure 7). However, intriguing is that in the low sSFR stack, all absorption lines agree well with the $[\text{CII}]$ redshift, while in the high sSFR stack the lines are significantly blue shifted by $300 - 400 \text{ km s}^{-1}$. We also note that in the high sSFR stack, the C IV line shows a noticeable P-Cygni profile indicative of strong winds and outflows (Castor & Lamers 1979). These findings fit well into a picture of strong winds and outflows produced by the high star-formation in these galaxies, which is also in line with recent results obtained through the stacking of ALPINE $[\text{CII}]$ spectra (Ginolfi et al. 2019).

2.4.3. How well does $[\text{CII}]$ trace systemic redshift? Comparison to optical $[\text{OII}]$ emission

The extended nature of $[\text{CII}]$ may be indicative of its origin in the diffuse interstellar medium in addition to PDRs (Stacey et al. 1991; Gullberg et al. 2015; Vallini et al. 2015; Faisst et al. 2017). Moreover, recent work by Ginolfi et al. (2019) shows that $[\text{CII}]$ emission is significantly affected by large-scale outflows caused by high

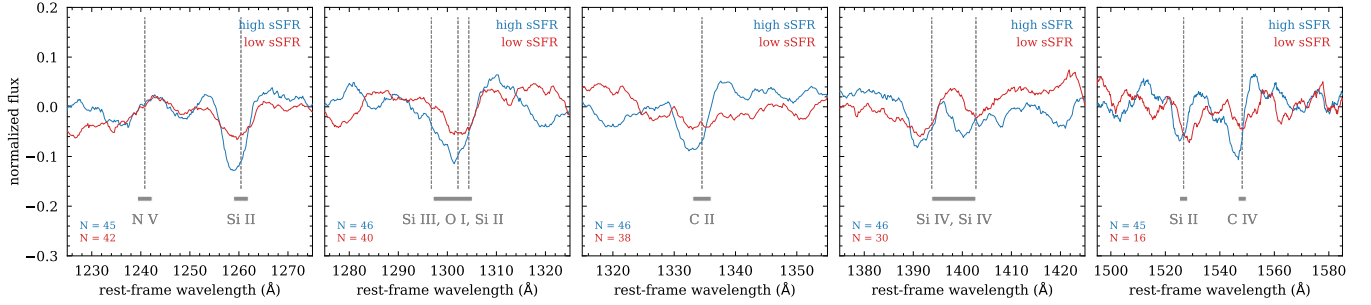


Figure 9. Stacked spectra (in C II systemic redshift) in two bins of sSFR (red: $< 4 \text{ Gyr}^{-1}$, blue: $> 5 \text{ Gyr}^{-1}$) for five wavelength regions covering prominent rest-UV absorption lines. The average number of spectra in each bin is indicated together with the prominent absorption and emission lines. We note systematically stronger blue shifts of all absorption lines for the high sSFR stack. Particularly, note the strong blue-shift of the high-ionization wind lines. The C IV lines in the high sSFR bin also show indication of a more pronounced P-Cygni profile, indicative of strong stellar winds and outflows in high sSFR galaxies.

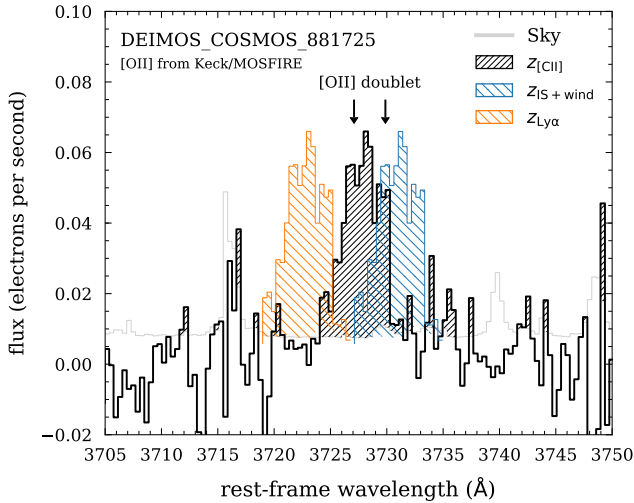


Figure 10. MOSFIRE observations of the optical [O II] line of *DC_881725* at a [C II] redshift of $z_{\text{[C II]}} = 4.5777$ (black line). The location of the [O II] doublet in the [C II] rest-frame is indicated by the black arrows. We find no velocity offset between the optical [O II] lines and the far-infrared [C II] line, indicating that both species trace the same systemic redshift. In blue and orange, we show the [O II] emission in the rest-frame defined by the IS+wind and Ly α redshift, respectively. As seen in Figure 7, the lines are significantly shifted to the blue and red.

star-formation in these galaxies. However, as shown by the same study, the outflows seem to be symmetric and therefore we do not expect them to significantly change the centroid of the [C II] emission line.

During January 13-15, 2019, we were able to obtain a near-IR spectrum of one of our *ALPINE* galaxies (*DC_881725* at $z_{\text{[C II]}} = 4.5777$) using the *Multi-Object Spectrometer For Infra-Red Exploration* (MOSFIRE, McLean et al. 2010, 2012) at the 10-meter Keck I telescope on Mauna Kea in Hawaii. The observations of a total on-source integration time of 24×3 min in *K* band ($1.92 - 2.40 \mu\text{m}$) were carried out under clear weather

conditions with an excellent average seeing FWHM of $0.3'' - 0.4''$. We performed a standard data reduction using the MOSFIRE data reduction pipeline⁷ (Version 2018). From the produced 2-dimensional spectrum and variance map, we extract the 1-dimensional spectrum at the spatial location of the galaxy using a weighted mean across ± 3.5 spatial pixels ($0.18''/\text{px}$).

We are able to detect the optical [O II] doublet (3727.09 \AA and 3729.88 \AA) at the spatial position of the galaxy at a level of $> 5\sigma$. Note that this is the first detection of optical [O II] in a galaxy with [C II] measurement from ALMA, which allows us for the first time to compare this two lines at these redshifts. In Figure 10, we show the final spectrum in the rest-frame of the [C II] emission. The width of $\sim 4 \text{ \AA}$ includes both [O II] lines (indicated by the two black arrows). The position of the line agrees perfectly with the [C II] redshift derived from ALMA, indicating that [C II] traces the same systemic redshift. In addition, we show in blue and orange the [O II] line in the rest-frame of the absorption lines ($z_{\text{IS+wind}}$) and Ly α ($z_{\text{Ly}\alpha}$). As shown in Figure 7, these features are significantly blue and red shifted with respect to the [C II] rest-frame.

3. PHOTOMETRY FROM GROUND AND SPACE

In this section, we summarize the ground- and space-based photometric data that are available for the *ALPINE* galaxies in the COSMOS (105 galaxies) and ECDFS (13 galaxies) fields. Although these fields differ in survey depth, reduction methods, and number and type of photometric filters used, we find that their overall photometric measurements are comparable after their conversion to total magnitudes and the correction for the specific biases of each survey. Therefore, we can treat them separately to first order for the

⁷ <https://keck-datareductionpipelines.github.io/MosfireDRP/>

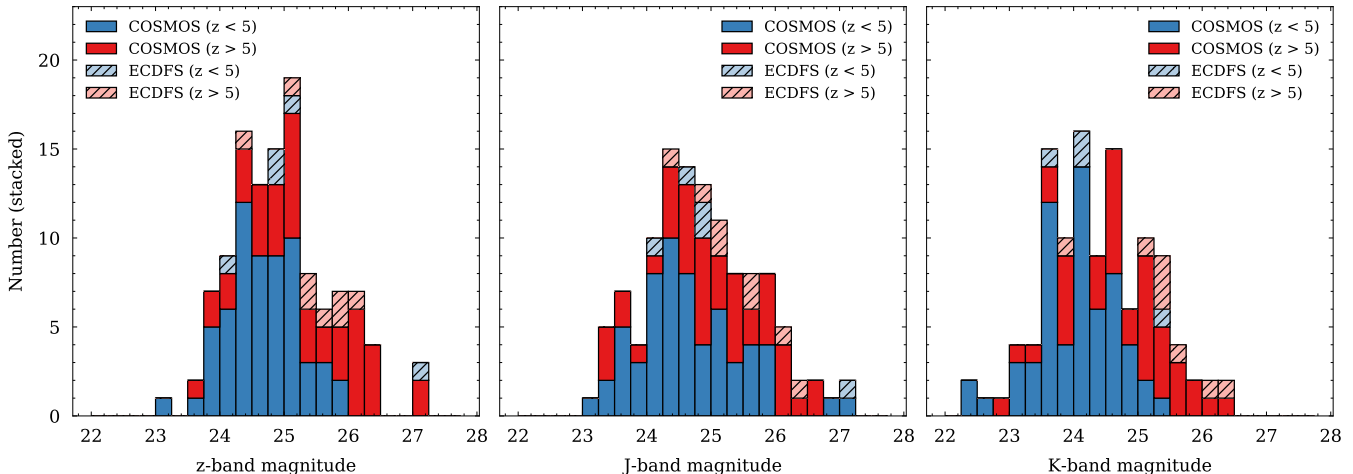


Figure 11. Stacked histograms of the magnitude distribution for the *ALPINE* galaxies in the COSMOS (solid) and ECDFS (hatched) fields. The blue and red color-coding indicates galaxies at $z < 5$ and $z > 5$, respectively. The magnitudes (from left to right) correspond to z^{++} , J , and K_s bands for COSMOS and $F850LP$, J^v , and K_s^v bands for ECDFS (see Tables 2 and 3 for more information on the filters).

matter of measuring various physical properties of the galaxies. The basis catalogs to which we match the *ALPINE* galaxies in the COSMOS and ECDFS field are the *COSMOS2015*⁸ (Laigle et al. 2016) and the *3D-HST*⁹ (Brammer et al. 2012; Skelton et al. 2014) catalog, respectively. A summary of the different data available on the two fields including filter names, wavelengths, 3σ depths, and references to the measurements are given in Tables 2 and 3, respectively. In the following, we describe these data in more detail.

3.1. Photometry on the ECDFS field

The photometry for the galaxies on the ECDFS field is taken directly from the *3D-HST* catalog, which provides ground-based observations as well as a wealth of data from HST imaging. The photometry (total fluxes and magnitudes) is corrected for Galactic extinction, PSF size as well as other biases, therefore no further correction are applied. The *ALPINE* galaxies are matched visually to the spatially closest *3D-HST* counterpart using the HST WFC3/IR $F160W$ image as reference. The spectroscopic redshifts match the photometric redshifts within their uncertainty ($\sim 0.1 - 0.2$), ensuring that we identified the correct counterpart.

The ground-based photometry available in ECDFS (including references) is listed in Table 2. Summarizing, this includes the $U38$, b , v , R_c , and I broad-band filters from the Wide Field Imager on the 2.2 meter MPG/ESO telescope, the U and R bands from VIMOS on the VLT,

the near-IR filters J^v , H^v , and K_s^v from ISAAC on the VLT, J_w and K_s^w data taken by WIRCcam on the CFHT, as well as 14 intermediate-band filter from the Suprime-Cam on the Subaru telescope. For galaxies at $z = 4.5$ and 5.5 , the Lyman-break falls roughly in the v and the R_c -band and therefore the galaxies are expected to be only faintly (or not at all) visible in these and blue-ward filters. On the other hand, the galaxies are bright at observed near-IR wavelengths, i.e., filters red-ward of z -band (corresponding to roughly the $F850LP$ filter). Figure 11 shows the stacked $F850LP$ (z), J^v (J) and K_s^v (K) magnitude distributions of the ECDFS *ALPINE* galaxies split in $z < 5$ (hatched blue) and $z > 5$ (hatched red). As expected, the latter sample occupies slightly fainter magnitudes.

The space-based photometry includes the four Spitzer bands at $3.6 \mu\text{m}$, $4.5 \mu\text{m}$, $5.8 \mu\text{m}$, and $8.0 \mu\text{m}$. In addition, the public *3D-HST* catalog includes a wealth of HST photometry. Specifically, it contains measurements in the ACS bands $F435W$, $F606W$, $F775W$, $F814W$, and $F850LP$ as well as in the WFC3/IR bands $F125W$, and $F160W$ bands for all 13 *ALPINE* galaxies. Only 10 galaxies have measurements in the WFC3/IR band $F140W$. The HST photometry is measured on PSF-matched images. As described in Skelton et al. (2014), the Spitzer and ground-based photometry are measured using the MOPHONGO (Labbé et al. 2006; Wuyts et al. 2007; Whitaker et al. 2011), which uses a high-resolution image (here the HST imaging) as spatial prior to estimate the contributions from neighboring blended sources in the lower resolution image. The different depths of these observations as well as references are listed in Table 2. A query of the Barbara A. Mikul-

⁸ <http://cosmos.astro.caltech.edu/page/photom>

⁹ <https://3dht.research.yale.edu/Data.php>

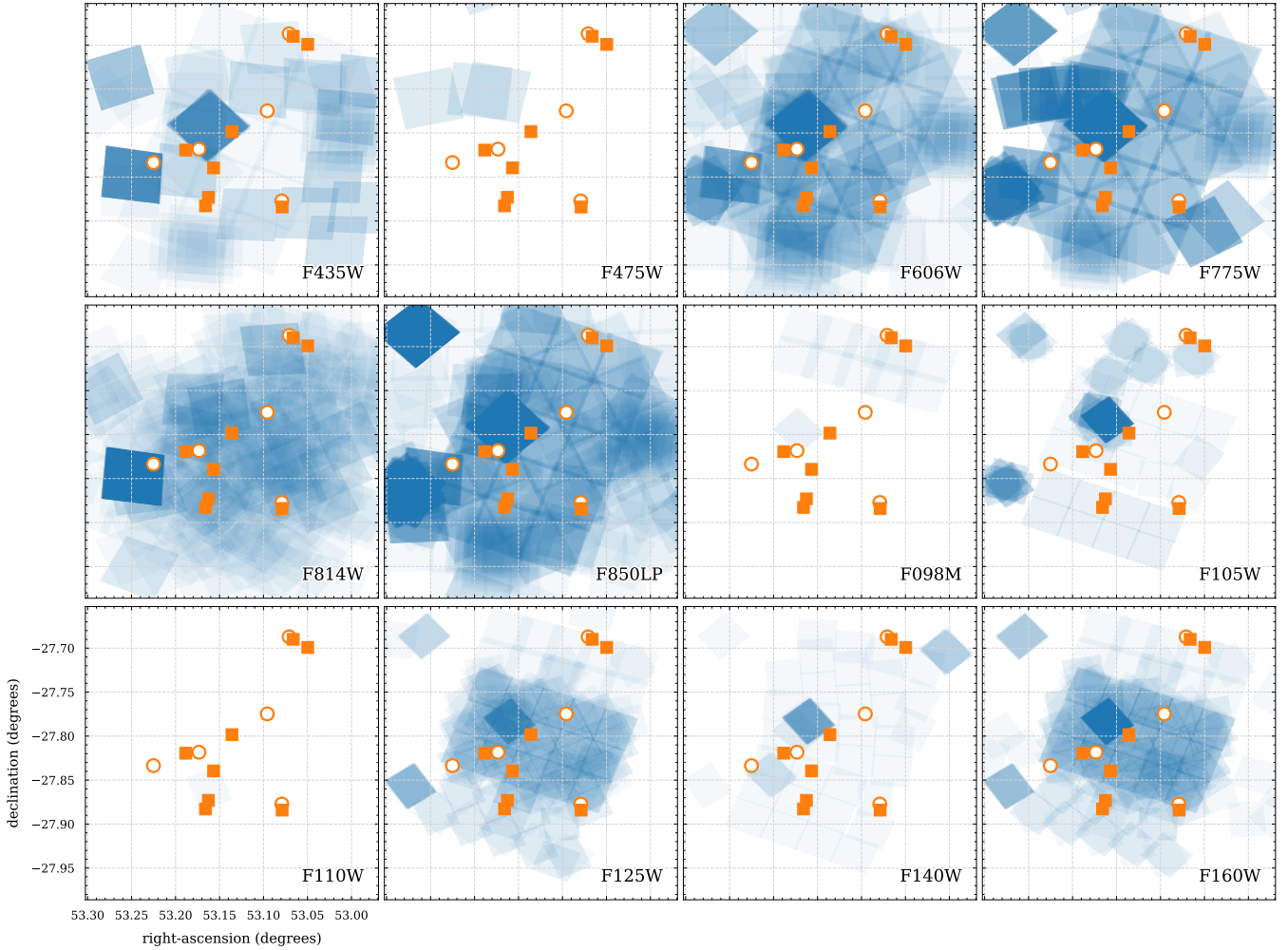


Figure 12. HST pointing footprints on the ECDFS field (blue) for different HST ACS and WFC3/IR filters. Darker colors mean more observations. The *ALPINE* galaxies are indicated by orange circles and squares for $z < 5$ and $z > 5$, respectively.

ski Archive for Space Telescopes (MAST¹⁰) using the *mastquery* Python package¹¹ shows that in addition to the HST measurements contained in the *3D-HST* catalog, four, ten, and two galaxies have coverage in the WFC3/IR bands *F098M*, *F105W*, and *F110W*, respectively. None of the galaxies has ACS *F475W* coverage. These additional data that are not published in the *3D-HST* catalog come from various other observation programs in and around the ECDFS field. We subsequently measure this additional photometry for all *ALPINE* galaxies in ECDFS using *SExtractor* (version 2.19.5, Bertin & Arnouts 1996) in different aperture sizes (0.7'' and 3'') as well as auto magnitudes. For this, we first create a mosaic of all the HST pointings that overlap with

the *ALPINE* galaxies using the *AWS-drizzler*¹² tool that is part of the *grizli*¹³ Python package (Brammer, in prep.). We use a 0.06'' pixel scale and all HST images are registered to Gaia (see Section 3.3). *SExtractor* is run with relative *THRESH_TYPE*, and we set *DETECT_MINAREA*, *DETECT_THRESH*, *DEBLEND_MINCONT*, and *DEBLEND_NTHRESH* to 3, 1.5, 1.5, 0.001, and 64, respectively. If no object is detected above the threshold (1.5σ) within 0.7'' (roughly the ground-based seeing) of the original *ALPINE* coordinates, we consider the galaxy as undetected in a given band and replace its flux by a 1σ limit that is computed from the RMS noise at the position of the galaxy. The photometry measured by *SExtractor* is subsequently corrected for galactic foreground extinction, which we assume to be constant

¹⁰ <https://mast.stsci.edu>

¹¹ <https://github.com/gbrammer/mastquery>

¹² <https://github.com/grizli-project/grizli-aws>

¹³ <https://github.com/gbrammer/grizli>

for all galaxies in ECDSF at $E(B - V) = 0.0069$ mag. Figure 12 summarizes the HST data available for the galaxies in the ECDFS field. The blue squares show the layout of all the HST pointings as of October 2019, with darker shades of blue indicating more observations. The *ALPINE* galaxies at $z < 5$ and $z > 5$ are indicated with orange circles and squares, respectively.

3.2. Photometry on the COSMOS field

Most of the *ALPINE* galaxies (105 out of 118) reside in the COSMOS field and we match them to the latest photometric measurements presented in the *COSMOS2015* catalog. The matching is again done on a galaxy-by-galaxy basis using the HST/ACS *F814W* as well as UltraVISTA K_s images as references. We also match against the photometric redshifts given in the catalog in order to identify the correct counterpart¹⁴.

In Table 3, we list all the photometric measurements available for the *ALPINE* galaxies on the COSMOS field. Summarizing, these include u^* -band observations from MegaCam on CFHT, the B , V , r^+ , i^+ , z^{++} as well as 12 intermediate-band and 2 narrow-band filters from the Suprime-Cam on Subaru, the Y_{HSC} -band from the Hyper Suprime-Cam on Subaru as well as near-IR bands H_w and K_s^w from WIRCam on CFHT and Y , J , H , and K_s from VIRCAM on the VISTA telescope. In addition, the galaxies are covered by the four Spitzer channels from $3.6\ \mu\text{m}$ to $8.0\ \mu\text{m}$ from the SPLASH survey¹⁵ (Capak et al. 2012; Steinhardt et al. 2014; Laigle et al. 2016). As described in (Laigle et al. 2016), the Spitzer photometry is measured using IRACLEAN (Hsieh et al. 2012), which uses positional priors from higher resolution imaging (in this case the $zYJKHK_s$ detection χ^2 -image) to deblend the photometry.

Contrary to the *3D-HST* photometry catalog, the fluxes and magnitudes in the *COSMOS2015* catalog are not total and not corrected for systematic biases and Galactic extinction. To perform these corrections, we follow the steps outlined in the appendix of Laigle et al. (2016). Specifically, we use the $3''$ diameter aperture magnitudes (\mathcal{M}^3), which we correct for photometric (o_i , see their equation 4) and systematic offsets (s_f , see their table 3) by applying

$$\mathcal{M}_{i,f}^{\text{tot,uncorr}} = \mathcal{M}_{i,f}^3 + o_i - s_f, \quad (1)$$

where i is the object identifier and f denotes the different filters. The total magnitudes are subsequently

corrected for Galactic extinction by applying

$$\mathcal{M}_{i,f}^{\text{tot}} = \mathcal{M}_{i,f}^{\text{tot,uncorr}} - \text{EBV}_i \times F_f, \quad (2)$$

where EBV_i is the Galactic extinction from the Schlegel et al. (1998) maps on COSMOS for each object as given in the catalog and F_f are the extinction factors per filter given in table 3 of Laigle et al. (2016).

Figure 11 shows the stacked magnitude distribution in z^{++} (z), J , and K_s (K) bands for the $z < 5$ (blue) and $z > 5$ (red) sub-samples. As expected, the high-redshift galaxies are fainter in all bands. In addition, we find the magnitude distributions between the galaxies in ECDFS and COSMOS to be similar. This indicates no major discrepancies in photometric, hence physical properties between the two samples.

In terms of HST imaging, all galaxies except one are observed in ACS *F814W* (Scoville et al. 2007a; Koekemoer et al. 2007). In addition to this, a MAST-search shows that several galaxies are covered by other observing programs in the ACS bands *F435W* (3), *F475W* (5), *F606W* (21), and *F850LP* (5) as well as in the WFC3/IR bands, *F105W* (11), *F110W* (5), *F125W* (16), *F140W* (13), and *F160W* (53)¹⁶. Note that the observations in *F160W* primarily come from the CANDELS survey (covering the central part of COSMOS, Grogin et al. 2011; Koekemoer et al. 2011) as well as the ‘‘drift and shift’’ (DASH, Momcheva et al. 2017) survey. While the CANDELS imaging is deep (> 27.5 magnitudes at 3σ), the data from the DASH survey is much shallower (25.0 magnitudes at 3σ) and therefore only half of the galaxies are detected. Furthermore, the spatial sampling in the latter does not allow a detailed study of the structure of the galaxies. Figure 13 summarizes the HST pointings on the COSMOS field (blue). The CANDELS area in the center of the COSMOS field as well as the three DASH stripes are evident. The location of the *ALPINE* galaxies is indicated with circles ($z < 5$) and squares ($z > 5$). The photometry available is summarized in Table 3 including depths (where applicable) and references.

In order to measure the photometry in these HST bands, we use **SExtractor** in the same way as described in Section 3.1. We first create a mosaic ($0.06''$ pixel sizes and registered to Gaia) using the **AWS-drizzler**. We subsequently measure the HST photometry of on each of the images for all *ALPINE* galaxies with coverage using **SExtractor** in apertures ($0.7''$ and $3''$) as well as auto magnitudes. If no object is detected above the set threshold level within $0.7''$ of the original *ALPINE*

¹⁴ The photometric redshifts given in the *COSMOS2015* catalog are consistent within 0.2 with our spectroscopic redshifts for more than 95% of all cases.

¹⁵ <https://splash.caltech.edu>

¹⁶ There is also data in the *F098W* filter, however, unfortunately no *ALPINE* galaxies are covered.

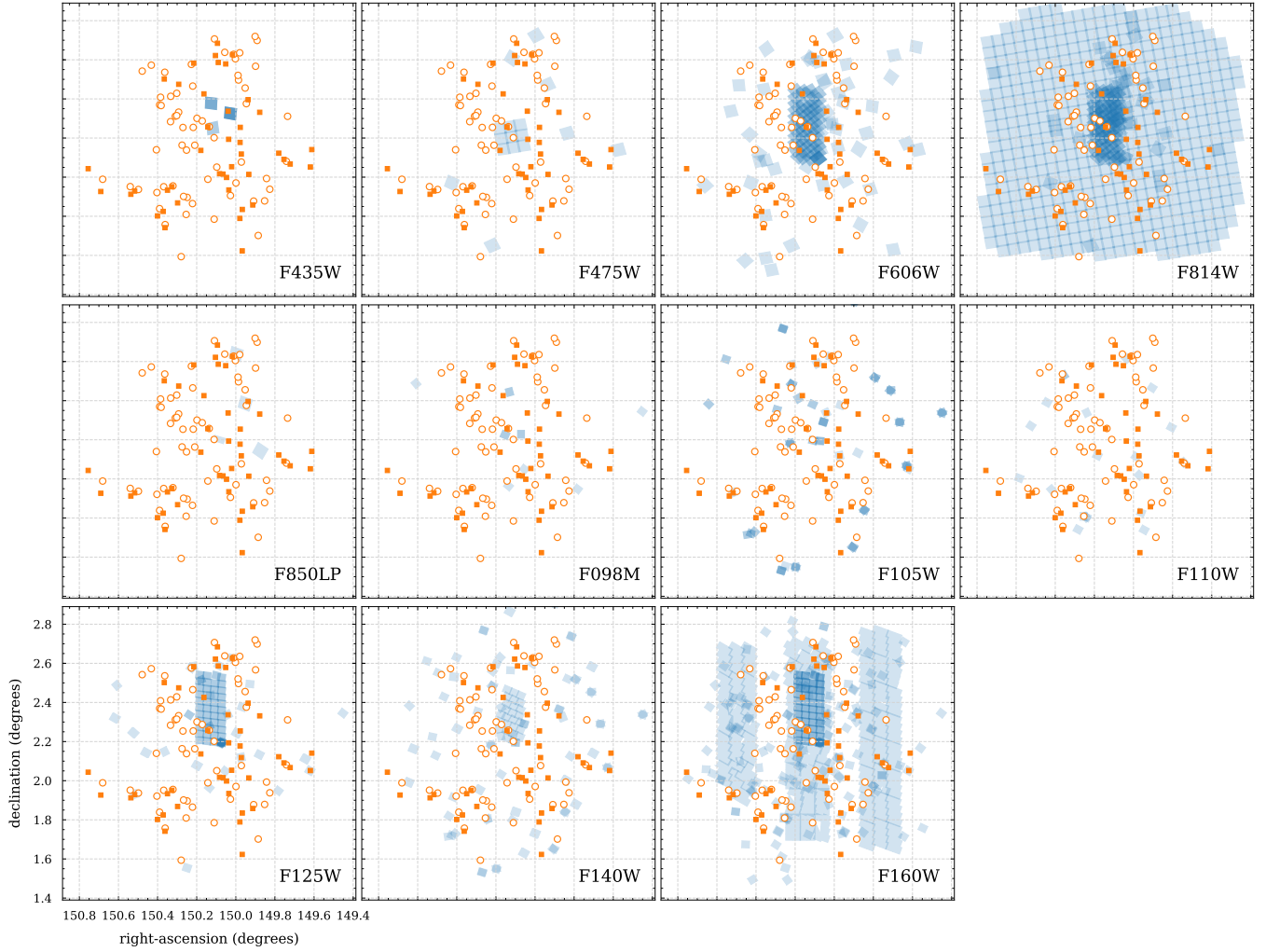


Figure 13. HST pointing footprints on the COSMOS field (blue) for different HST ACS and WFC3/IR filters. Darker colors mean more observations. The *ALPINE* galaxies are indicated by orange circles and squares for $z < 5$ and $z > 5$, respectively.

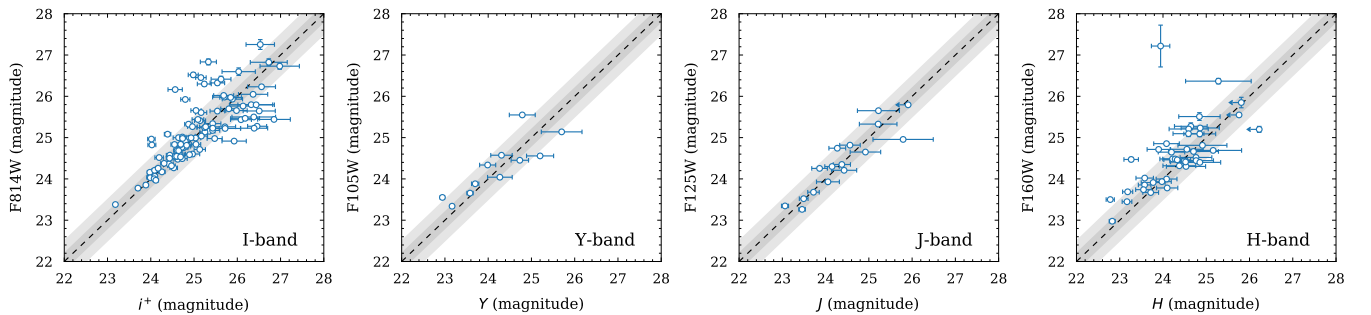


Figure 14. Comparison of ground-based and HST-based photometry (see text for details) in four filters on the COSMOS field. The dark gray region indicates ± 0.2 magnitude and the light gray region indicates ± 0.5 magnitude differences. The photometry agrees well with an expected increase in scatter at fainter magnitudes. We observe a systematic offset towards brighter ground-based magnitudes at bright (< 23.4 AB) H -band magnitudes.

coordinates, we consider the galaxy as undetected in a given band. Similar to Equation 2, we correct the HST photometry for galactic foreground extinction using the Schlegel et al. (1998) extinction map. We compare these measurements to the ground-based photometry, by first performing a PSF matching by smoothing the original HST images with a Gaussian kernel with FWHM of $0.7''$ and measure the photometry in a $3''$ aperture (as used in the *COSMOS2015* catalog). Figure 14 compares the ground-based (i^+ , Y , J , H) with the HST ($F814W$, $F105W$, $F125W$, $F160W$) photometry in approximately matching filter bands. The overall agreement is on average 0.2 magnitudes (dark gray region) with an expected increase of scatter at fainter magnitudes. For the four brightest sources in H -band (< 23.4 AB), the ground-based measured photometry is systematically up to 0.5 magnitudes brighter in three out of four cases. Due to the low number of galaxies, it is difficult to investigate this statistically. A more detailed measurement of the HST photometry including deblending of specific sources such as merging or clumpy galaxies, will be provided in a forthcoming paper.

3.3. Astrometric offsets between ALMA and ancillary data

Astrometric accuracy is crucial in many cases. First, accurate spatial offsets of light emission from rest-frame UV, optical, and sub-mm wavelengths reveal the properties of the interstellar medium such as the location and interplay of stars, dust, and gas. Second, the robustness of the identification of sub-mm counterparts needs a high astrometric accuracy of all involved datasets. As described in Sections 3.1 and 3.2, the HST images produced for the *ALPINE* galaxies are all aligned to Gaia. Our tests show that the average offsets are less than 15 milli-arcseconds (mas) in both right-ascension and declination with a scatter of no more than 30 mas (G. Brammer, private communication). Unfortunately, the positional accuracy for current catalogs (such as *3D-HST* or *COSMOS2015* that are used here) are lower and we expect significant offsets between those astrometric solution and ALMA data products. In the following, we characterize these offsets.

According to the technical handbook, ALMA observations are currently registered to the *International Celestial Reference Frame* (ICRF) to an accuracy better than ~ 5 mas. The ICRF is based on hundreds of extragalactic radio sources such as quasars distributed over the whole sky. The positional accuracy Δp of single observations can be estimated by

$$\Delta p = \frac{70000}{\nu \cdot B \cdot \sigma}, \quad (3)$$

where ν is the observed frequency in GHz, B is the maximum baseline length in kilometers, and σ is the S/N at the peak of emission. For *ALPINE* ($\nu = 330$ GHz and $B = 0.2$ km for C43-1) this leads to $\Delta p = 1060/\sigma$. The calibrators are detected well above 50σ , which leads to an absolute positional accuracy of ~ 20 mas or better.

To check the astrometric alignment of the photometric catalogs used here, we make use of the Gaia DR2 catalog (Mignard et al. 2018), which provides currently the most accurate absolute astrometry. As shown in Mignard & Klioner (2018), there are no significant offsets between this reference frame and the ICRF frame used by ALMA, hence this test directly reveals potential differences in astrometry between the *3D-HST* and *COSMOS2015* catalogs and our ALMA observations. Using the proper motion information of the stars from Gaia, we project their positions back in time to the year of calibration of the data products by using the equations

$$\begin{aligned} \Delta\alpha &= \cos(\delta) \cdot \mathcal{P}_\alpha \cdot (t_{\text{ref}} - t_{\text{gaia}}), \\ \Delta\delta &= \mathcal{P}_\delta \cdot (t_{\text{ref}} - t_{\text{gaia}}), \end{aligned} \quad (4)$$

where α and δ denote the right-ascension and declination (and \mathcal{P}_α and \mathcal{P}_δ their proper motion), t_{gaia} is the Gaia reference frame in years (here 2015.5), and t_{ref} is the reference frame of the calibration of the catalogs. To increase accuracy, we only include stars with a proper motion in both coordinates of less than 5 mas yr^{-1} in the following. Note that no parallax motion is included in the above formulae, which would result in less than 5 mas yr^{-1} astrometric shifts.

The *COSMOS2015* catalog is calibrated to the MegaCam i -band data that was taken in 2004 (Laigle et al. 2016). For ECDFS, the catalog (*3D-HST*) is calibrated to the same reference system as the CANDELS HST images, namely ground-based R -band data taken in 2001 (Koekemoer et al. 2011; Skelton et al. 2014). However, the exact year is not important as we have selected stars with a relatively slow proper motion. In order to select stars on the COSMOS field, we use the ACS/F814W **SExtractor** catalog (Scoville et al. 2007a) and select sources with a magnitude brighter than 23 AB and **SExtractor** star/galaxy classifier value of > 0.8 . These stars are then matched to the *COSMOS2015* catalog to obtain their position in that catalog. For ECDFS we extract stars directly from the *3D-HST* catalog by selecting sources brighter than 23 AB in F160W with **star_flag** = 1 and a **SExtractor** star/galaxy classifier value larger than 0.8. Other selections (e.g., different magnitude cuts) do not affect the following results. The Gaia stars are then matched to the star catalogs in COSMOS and ECDFS to obtain the astrometric offsets. In

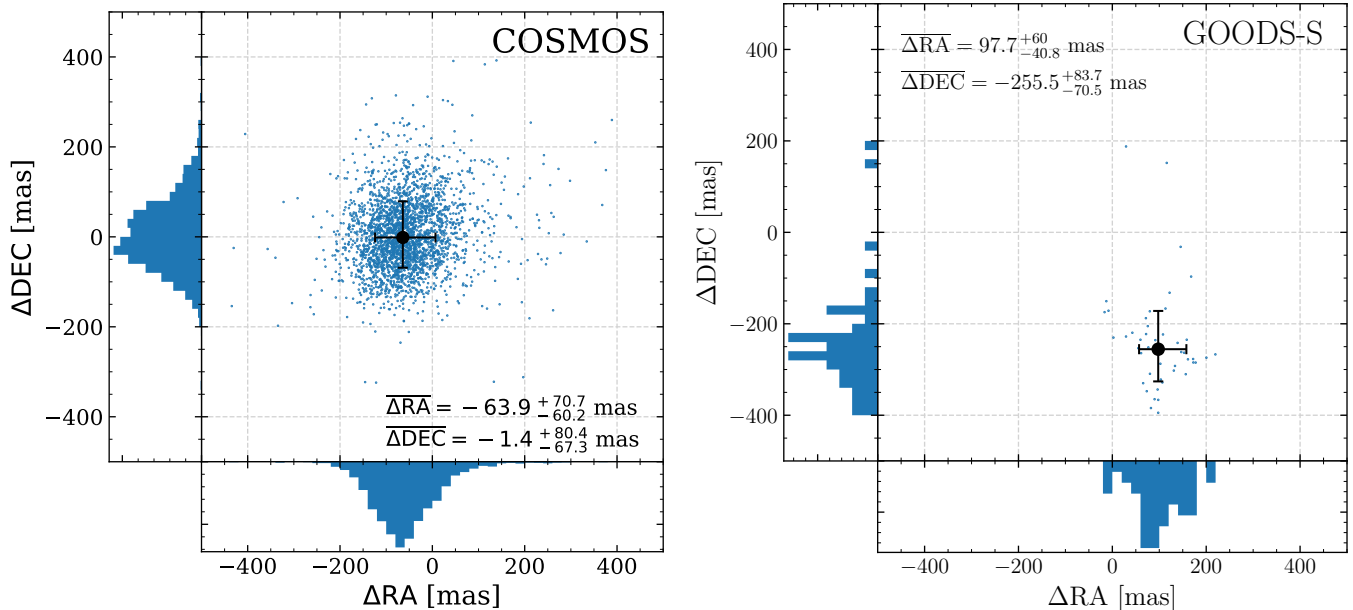


Figure 15. Scatter diagrams and histograms of offsets between the Gaia reference frame and the *COSMOS2015* (left) and *3D-HST* (ECDFS, right) catalogs. The offsets are in the sense “Gaia – COSMOS” and “Gaia – ECDFS”, respectively. For COSMOS we find only a systematic offsets in right-ascension direction of -64 mas. For ECDFS, the offsets are large in both directions. In addition to this, we measure a scatter in the astrometry of ~ 100 mas for both fields in both coordinates.

total, 47 and 2724 Gaia stars are used in ECDFS and COSMOS, respectively.

Figure 15 shows scatter plots and histograms comparing the position of the Gaia stars to the positions in the catalogs. We find significant systematic offsets in the astrometry in ECDFS of 98 mas in right-ascension and -256 mas in declination. These offsets are consistent with what was found in earlier studies (Dunlop et al. 2017; Franco et al. 2018; Whitaker et al. 2019). For COSMOS we only find a significant offset in right-ascension of -64 mas. In addition to that, there is a significant scatter in the astrometry on the order of 100 mas in both coordinates in both fields.

To compute the astrometric offset of individual *ALPINE* galaxies, we make use of the fact that the HST images are already aligned to the Gaia reference frame (see details in Sections 3.1 and 3.2). Specifically, we compute the offsets between the coordinates measured on the ACS/F814W images and the original coordinates from the *3D-HST* or *COSMOS2015* catalog. If no ACS F814W image is available or if the galaxy is not detected (which happens for redshifts $z > 5$), we use the deepest image red of F814W. If none is available (in four cases), we report the average offset as shown in Figure 15.

Note that the coordinates given in the final ancillary data catalog are not corrected for these offsets. However, we give the offsets for each galaxy in the columns `delta.RA` and `delta.DEC`, which can be *added* to

the original coordinates to obtain Gaia-corrected right-ascensions and declinations (see Appendix A).

4. PHYSICAL PROPERTIES

In this section, we detail measurements of various basic physical properties of the *ALPINE* galaxies that are based on their total, extinction corrected photometry described in Section 3. These include physical quantities from SED fitting such as stellar masses, SFRs, ages, and dust attenuation (§4.1), and UV continuum slopes (§4.3), as well as quantities directly derived from the photometry such as UV magnitudes and luminosities (§4.2) and estimates of the $H\alpha$ luminosity and equivalent width from Spitzer colors (§4.4).

4.1. Stellar mass and SFRs from SED fitting

4.1.1. Fitting Method

For consistency and comparability with other studies on the COSMOS field, we choose the *LePhare* SED fitting code¹⁷ (Arnouts et al. 1999; Ilbert et al. 2006) to derive stellar masses, SFRs, light-weighted stellar population ages, absolute magnitudes, optical dust reddening, and UV continuum slopes of the *ALPINE* galaxies.

¹⁷ <http://www.cfht.hawaii.edu/~arnouts/lephare.html>

Table 2. Photometry available for galaxies on the ECDFS field.

| Observatory/Instrument | Filter | Central λ (Å) | 3σ depth (mag) | Ref. |
|------------------------|----------------------------------|--------------------------|--------------------------|------|
| Ground-based | | | | |
| MPG-ESO/WFI | <i>U</i> 38 | 3633.3 | 27.3 | 1 |
| | <i>b</i> | 4571.2 | 26.6 | 1 |
| | <i>v</i> | 5377.0 | 26.6 | 1 |
| | <i>R_c</i> | 6536.3 | 26.9 | 1 |
| VLT/VIMOS | <i>I</i> | 9920.2 | 26.5 | 1 |
| | <i>U</i> | 3720.5 | 28.6 | 2 |
| VLT/ISAAC | <i>R</i> | 6449.7 | 27.8 | 2 |
| | <i>J^v</i> | 12492.2 | 25.6 | 3 |
| CFHT/WIRCam | <i>H^v</i> | 16519.9 | 25.1 | 3 |
| | <i>K_s^v</i> | 21638.3 | 25.0 | 3 |
| | <i>J_w</i> | 12544.6 | 25.1 | 4 |
| Subaru/Suprime-Cam | <i>K_s^w</i> | 21590.4 | 24.5 | 4 |
| | <i>IA427</i> | 4263.4 | 25.7 | 5 |
| | <i>IA445</i> | 4456.0 | 25.7 | 5 |
| | <i>IA505</i> | 5062.5 | 25.8 | 5 |
| | <i>IA527</i> | 5261.1 | 26.7 | 5 |
| | <i>IA550</i> | 5512.0 | 26.0 | 5 |
| | <i>IA574</i> | 5764.8 | 25.7 | 5 |
| | <i>IA598</i> | 6000.0 | 26.6 | 5 |
| | <i>IA624</i> | 6233.1 | 26.5 | 5 |
| | <i>IA651</i> | 6502.0 | 26.7 | 5 |
| | <i>IA679</i> | 6781.1 | 26.6 | 5 |
| | <i>IA738</i> | 7371.0 | 26.5 | 5 |
| | <i>IA767</i> | 7684.9 | 25.5 | 5 |
| | <i>IA797</i> | 7981.0 | 25.2 | 5 |
| <i>IA856</i> | 8566.0 | 25.0 | 5 | |
| Space-based | | | | |
| HST/ACS | <i>F435W</i> | 4328.7 | 29.1 | 6 |
| | <i>F606W</i> | 5924.8 | 29.1 (29.0) | 6,7 |
| | <i>F775W</i> | 7704.8 | 28.4 | 6 |
| | <i>F814W</i> | 8058.2 | 28.9 | 7 |
| HST/WFC3 | <i>F850LP</i> | 9181.2 | 27.9 | 6 |
| | <i>F125W</i> | 12516.3 | 27.6 | 8 |
| | <i>F140W</i> | 13969.4 | 26.7 | 9 |
| | <i>F160W</i> | 15391.1 | 27.7 | 8 |
| <i>Spitzer</i> /IRAC | <i>ch₁</i> | 35634.3 | $\sim 26.0^a$ | 10 |
| | <i>ch₂</i> | 45110.1 | $\sim 26.0^a$ | 10 |
| | <i>ch₃</i> | 57593.4 | 24.4 | 11 |
| | <i>ch₄</i> | 79594.9 | 24.3 | 11 |

^aThe exposure time varies between 10 ks and 300 ks (corresponding to roughly 1.8 in magnitudes).

References: (1) Hildebrandt et al. (2006); Erben et al. (2005), (2) Nonino et al. (2009), (3) Wuyts et al. (2008); Retzlaff et al. (2010), (4) Hsieh et al. (2012), (5) Cardamone et al. (2010), (6) Giavalisco et al. (2004), (7) Koekemoer et al. (2011), (8) Grogin et al. (2011); Koekemoer et al. (2011), (9) Brammer et al. (2012); van Dokkum et al. (2013), (10) Ashby et al. (2013); Guo et al. (2013), (11) Dickinson et al. (2003)

Table 3. Photometry available on the COSMOS field.

| Observatory/Instrument | Filter | Central λ (Å) | 3σ depth (mag) [†] | Ref. | |
|------------------------|--------------------------|----------------------------------|---------------------------------------|--------------------------|---|
| Ground-based | | | | | |
| CFHT/MegaCam | <i>u[*]</i> | 3823.3 | 26.6 | 1 | |
| Subaru/Suprime-Cam | <i>B</i> | 4458.3 | 27.0 | 1,2 | |
| | <i>V</i> | 5477.8 | 26.2 | 1,2 | |
| | <i>r⁺</i> | 6288.7 | 26.5 | 1,2 | |
| | <i>i⁺</i> | 7683.9 | 26.2 | 1,2 | |
| | <i>z⁺⁺</i> | 9105.7 | 25.9 | 1,2 | |
| | <i>IA427</i> | 4263.4 | 25.9 | 1,2 | |
| | <i>IA464</i> | 4635.1 | 25.9 | 1,2 | |
| | <i>IA484</i> | 4849.2 | 25.9 | 1,2 | |
| | <i>IA505</i> | 5062.5 | 25.7 | 1,2 | |
| | <i>IA527</i> | 5261.1 | 26.1 | 1,2 | |
| | <i>IA574</i> | 5764.8 | 25.5 | 1,2 | |
| | <i>IA624</i> | 6233.1 | 25.9 | 1,2 | |
| | <i>IA679</i> | 6781.1 | 25.4 | 1,2 | |
| | <i>IA709</i> | 7073.6 | 25.7 | 1,2 | |
| Subaru/HSC | <i>IA738</i> | 7361.6 | 25.6 | 1,2 | |
| | <i>IA767</i> | 7684.9 | 25.3 | 1,2 | |
| | <i>IA827</i> | 8244.5 | 25.2 | 1,2 | |
| | <i>NB711</i> | 7119.9 | 25.1 | 1,2 | |
| | <i>NB816</i> | 8149.4 | 25.2 | 1,2 | |
| | <i>Y_{HSC}</i> | 9791.4 | 24.4 | 1 | |
| | CFHT/WIRCam | <i>H_w</i> | 16311.4 | 23.5 | 1 |
| | | <i>K_s^w</i> | 21590.4 | 23.4 | 1 |
| | VISTA/VIRCAM | <i>Y</i> | 10214.2 | 24.8 (25.3) ^a | 1 |
| | | <i>J</i> | 12534.6 | 24.7 (24.9) ^a | 1 |
| | | <i>H</i> | 16453.4 | 24.3 (24.6) ^a | 1 |
| | | <i>K_s</i> | 21539.9 | 24.0 (24.7) ^a | 1 |
| | Space-based | | | | |
| | HST/ACS | <i>F435W</i> | 4328.7 | — ^b | — |
| <i>F475W</i> | | 4792.3 | — ^b | — | |
| <i>F606W</i> | | 5924.8 | — ^b | — | |
| <i>F814W</i> | | 8058.2 | 29.2 | 3 | |
| <i>F850LP</i> | | 9181.2 | — ^b | — | |
| HST/WFC3 | | <i>F098M</i> | 9877.4 | — ^b | — |
| | | <i>F105W</i> | 10584.9 | — ^b | — |
| | | <i>F110W</i> | 11623.8 | — ^b | — |
| | | <i>F125W^c</i> | 12516.3 | 27.6 ^{b,c} | 4 |
| <i>Spitzer</i> /IRAC | | <i>F140W</i> | 13969.4 | — ^b | — |
| | <i>F160W^c</i> | 15391.1 | 27.5 (25.0) ^{b,c,d} | 4,5 | |
| | <i>ch₁</i> | 35634.3 | 25.5 | 1,6,7 | |
| | <i>ch₂</i> | 45110.1 | 25.5 | 1,6,7 | |
| <i>Spitzer</i> /IRAC | <i>ch₃</i> | 57593.4 | 23.0 | 1,7 | |
| | <i>ch₄</i> | 79594.9 | 22.9 | 1,7 | |

[†] Depth is measured in 3'' aperture for ground-based photometry.

^a Depths of the ultra-deep area are given in parenthesis.

^b Ancillary pointings, therefore depth varies depending on the specific observations.

^c Most of these data come from the CANDELS survey and their depth is indicated.

^d Some of the F160W data comes from the DASH survey (depth given in parenthesis).

References: (1) see Laigle et al. (2016), (2) Taniguchi et al. (2007, 2015) (3) Scoville et al. (2007b); Koekemoer et al. (2007), (4) Grogin et al. (2011); Koekemoer et al. (2011), (5) Momcheva et al. (2017), (6) Capak et al. (2012); Steinhardt et al. (2014), (7) Sanders et al. (2007)

Importantly, stellar masses, SFR, and sSFR values are computed from the marginalized probability distribution functions over all the models and uncertainties are given in $\pm 1\sigma$ of this distribution.

We use a set of synthetic templates based on the Bruzual & Charlot (2003) stellar population library, which we tune to represent best galaxies at redshifts between $4 < z < 6$. In detail, we use a series of different star-formation histories (SFH) based on exponentially declining (with $\tau = 0.1, 0.3, 1.0,$ and 3.0 Gyrs), delayed¹⁸ (with $\tau = 0.1, 0.5, 1.0,$ and 3.0 Gyrs), and constant star formation. We add dust attenuation corresponding to a stellar $E_s(B - V)$ from 0 to 0.5 spaced in steps of 0.05 assuming a Calzetti et al. (2000) dust attenuation law. To account for metallicity dependence, we use a solar (Z_\odot) and $0.2Z_\odot$ metallicity. We also adopt a Chabrier (2003) IMF in the following. The model SEDs are generated for logarithmically spaced ages starting from 50 Myrs to the age of the universe at the redshift of each galaxy. To each SED, various rest-frame UV and optical emission lines are added following the description in Ilbert et al. (2009) by using common conversions outlined in Kennicutt (1998). Specifically, the UV luminosity at 2300 \AA is converted to a SFR using the relation $\text{SFR} (M_\odot \text{ yr}^{-1}) = 1.4 \times 10^{-28} L_\nu (\text{erg s}^{-1} \text{ Hz}^{-1})$ and subsequently translated to an [O II] emission line flux using the relation $\text{SFR} (M_\odot \text{ yr}^{-1}) = (1.4 \pm 0.4) \times 10^{-41} L_{[\text{O II}]} (\text{erg s}^{-1})$. Other emission lines ($\text{Ly}\alpha$, [O III], $\text{H}\beta$, $\text{H}\alpha$) are derived by assuming specific ratios to [O II] that are calibrated by observations (see detailed description with references in Ilbert et al. 2009).

The models are fit to the photometry described in Section 3 (and listed in Tables 2 and 3). Specifically, for the galaxies in the ECDFS field we use the ground-based observations in U , R , J^v , H^v , and K_s^v , as well as the intermediate-bands $IA427$, $IA505$, $IA527$, $IA574$, $IA624$, $IA679$, $IA738$, $IA767$, and $IA856$, and all four Spitzer channels ch_1 , ch_2 , ch_3 , and ch_4 . We also include observations in the HST filters $F435W$, $F606W$, $F775W$, $F814W$, $F850LP$, $F125W$, $F140W$, and $F160W$ that are properly combined with the ground-based and Spitzer measurements in the *3D-HST* catalog. For galaxies in the COSMOS field, we include the ground-based observations in u^* , B , V , r^+ , i^+ , z^{++} , Y , Y_{HSC} , J , H , H_w , K_s , and K_s^w , as well as the intermediate-bands $IA427$, $IA464$, $IA484$, $IA505$, $IA527$, $IA574$, $IA624$, $IA679$, $IA709$, $IA738$, $IA767$,

and $IA827$. We use all four Spitzer channels but no HST observations as only the one filter ($F814W$) exists for all galaxies.

The fits are performed in flux density space (f_ν in Jansky), which has several advantages compared to magnitude space. Specifically, it allows a proper statistical treatment of limits in the data of all bands. While in the case of magnitude limits an arbitrary significance level (e.g., 1σ , 3σ) has to be defined in order to use them in SED fitting, in flux density space no arbitrary choice needs to be made by the user as the limits manifest themselves only in the error bars of those bands where no flux is measured. This is important as slightly different levels of significance set for the limits can have profound effects on the output parameters, especially in cases where limits are imposed in astrophysically important parts of the rest-frame spectra (e.g., the Balmer break). In addition, some SED codes, including *Le Phare*, have difficulties dealing with limits (in the case of magnitudes) in a statistically consistent manner, and, instead, remove from consideration any models that slightly exceed these limits. Moving to flux density space for all fits alleviates these concerns.

To avoid artificially small errors that would dominate the χ^2 budget of a fit of a given galaxy, we rescale the official flux density errors by a factor of 1.1 and add the following systematic errors prior to fitting in different filters: 0.01 mag for all ground-based UV/optical broad-band measurements; 0.05 mag for all ground-based UV/optical intermediate-bands and near-IR broad-band measurements; 0.1 mag for Spitzer $3.6 \mu\text{m}$ and $4.5 \mu\text{m}$ and 0.3 mag for Spitzer $5.8 \mu\text{m}$ and $8.0 \mu\text{m}$ measurements. Such an approach is a common practice for SED-fitting, specifically including photometry on the COSMOS field (e.g., Ilbert et al. 2006, 2009, 2013), and is found to mitigate issues associated with poorly measured bands, poorly estimated zero points, or inhomogeneous methods of measuring photometry.

The large PSF sizes of the Spitzer observations result in a large risk of blended photometry. This can lead to an overestimation of flux and hence to an overestimation of stellar masses¹⁹. A cleaner and manual deblending of the Spitzer photometry (e.g., using a position prior from HST imaging) is possible and will be pursued in a forthcoming paper. In the following, we flag galaxies that have a bright companion galaxy within a Spitzer $4.5 \mu\text{m}$ PSF FWHM ($2.5''$) based on the ground-based and HST imaging data. In total, one-third of the galax-

¹⁸ The delayed SFR is parameterized as $\psi(t) \propto \tau^{-2} t e^{-t/\tau}$ such that $\psi(t)$ is maximal at $t = \tau$.

¹⁹ Note that the stellar masses are primarily constrained through the Spitzer photometry that covers rest-frame wavelengths redward of the Balmer break.

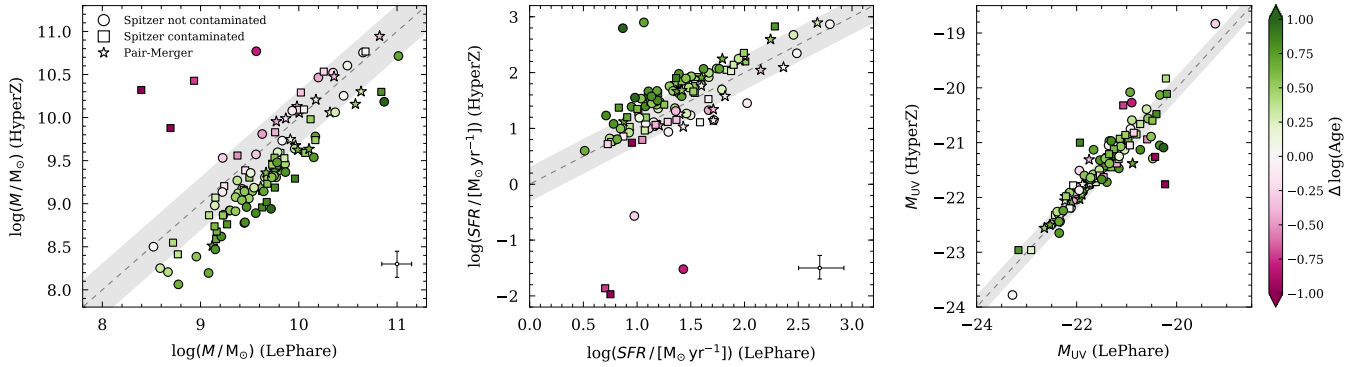


Figure 16. Comparison of stellar mass (left), SED-derived SFR (middle), and absolute rest-frame UV magnitude (right) measured by **LePhare** and **HyperZ**. The symbols are color-coded by the logarithmic difference in stellar population age (note that the scale is the same for all panels). The squares denote galaxies whose Spitzer photometry is blended with a nearby bright galaxy or star. The star-symbols denote mergers based on the classification in [Le Fèvre et al. \(2019\)](#). The 1-to-1 relation is shown as dashed line and a ± 0.3 margin is shown by the gray band. The systematic differences in stellar masses derived by **HyperZ** are likely caused by different implementations of rest-frame optical emission lines, which affect most the measurement of stellar masses (based on rest-frame optical light).

ies have contaminated Spitzer photometry to some degree. For 19% of the galaxies, the Spitzer photometry is severely contaminated and should not be trusted. We checked our simple flagging scheme against the contamination flags given in the *3D-HST* catalog, which are based on the flux fraction that is overlapping with the galaxy for which the photometry is measured. For the 13 *ALPINE* galaxies in ECDFS, we find excellent agreement between both classifications. The Spitzer contamination flags are included in the ancillary data catalog (column `spitzer_cont`).

4.1.2. Systematic Uncertainties in Physical Properties from Modeling Assumptions

Depending on their exact methods, different SED fitting codes may measure different physical properties even with the same photometry provided as input. In addition to more physical reasons (such as different assumptions on the stellar population models and implementation of emission lines), the different treatment of undetected fluxes (or fitting in magnitude space), varying minimization techniques and weightings, and different scaling of the error of the input photometry can contribute to these discrepancies.

To investigate the amplitude of such differences, we compare the measurements from **LePhare** to a modified version of the **HyperZ** code ([Bolzonella et al. 2000](#)) that includes the effects of nebular emission ([Schaerer & de Barros 2009](#)), to estimate such systematic uncertainties in the fitted parameters. To minimize the degeneracy with other assumptions, we run **HyperZ** on the exact same photometry and with the exact same model SEDs (i.e., same metallicity, age, SFH, and dust attenuation law) as described in Section 4.1.1. Figure 16 compares

the stellar mass (left), SED-derived SFR (middle), and absolute UV magnitude (right, see also Section 4.2) derived by the two codes. The symbols are color-coded by difference in stellar population age (positive values indicate younger ages derived by **HyperZ**). We find that the stellar masses derived by **HyperZ** are systematically smaller by 0.3–0.4 dex. Similarly, the SFRs are systematically larger by ~ 0.3 dex.

As expected, the absolute UV magnitudes are largely in agreement, as they are to first order independent of the physical parameters, and just represent a translation of the fitted UV flux.

The differences in stellar mass and SFR are due to the effect of nebular emission, which results in younger ages and larger emission line corrections of the intrinsic rest-frame optical continuum (observed by the Spitzer broad-bands) in the **HyperZ** models, and therefore directly affects the stellar mass measurements (see, e.g., [de Barros et al. 2014](#)). This is confirmed by the fact that the stellar masses and SFR measured by the two codes agree well (within a factor of two) if the emission lines are turned off. The effect of nebular emission found by **HyperZ** may be overestimated for the *ALPINE* galaxies, e.g., if the emission lines are more strongly attenuated than the continuum (see Section 4.4). For consistency and comparability with other studies on the COSMOS field, we choose the **LePhare** fitting results as the default.

Next to the systematic offset discussed above, we also find four galaxies (*DC_472215*, *DC_503575*, *DC_722679*, *DC_790930*) whose stellar mass measurements are significantly discrepant, by more than one order of magnitude, between the two codes. Specifically, they are fitted with an old, low-SFR, and massive galaxy tem-

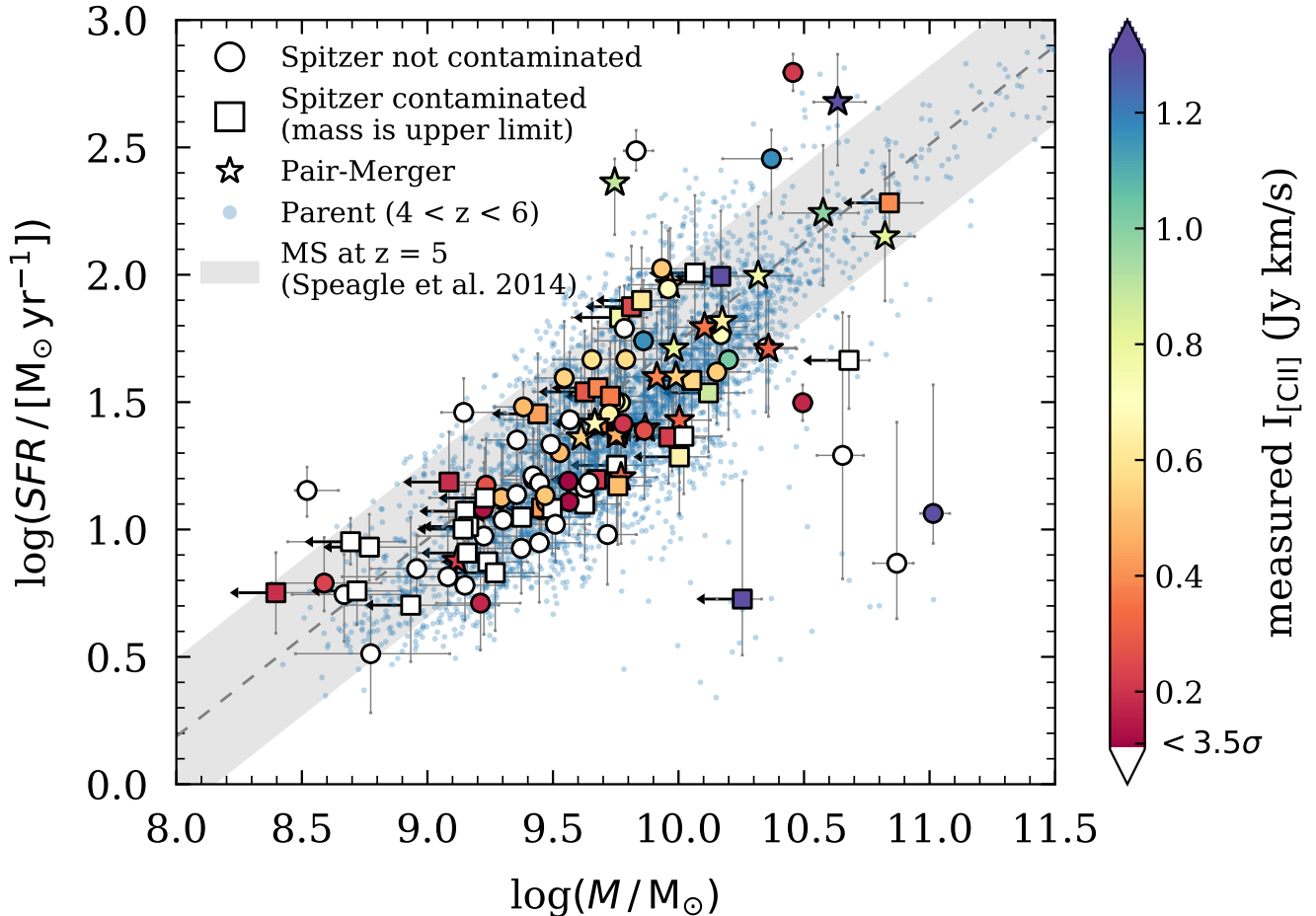


Figure 17. Relation between stellar mass and SFR (main-sequence) of our *ALPINE* galaxies compared to all *COSMOS* galaxies at $4 < z < 6$ (blue points) and the main-sequence parameterization at $z = 5$ by [Speagle et al. \(2014\)](#) (gray band with ± 0.3 dex width). Galaxies with contaminated Spitzer photometry are marked with squares (their stellar mass is likely an upper limit) and mergers (classification by [Le Fèvre et al. 2019](#)) are shown as stars. The color denotes the [C II] flux in Jy km s^{-1} measured by *ALPINE*. Galaxies that are not detected at the 3.5σ level are shown with white face color.

plate with *HyperZ*, while a young, high-SFR, and low-mass galaxy template is preferred by *LePhare*. Three of these outliers have significantly contaminated Spitzer photometry (indicated by the squares). As a consequence, the apparent Spitzer fluxes and stellar masses are overestimated and the optical colors are artificially reddened, which makes their stellar masses largely unreliable. Furthermore, we artificially increased the errors of the Spitzer photometry in our *LePhare* measurements (see Section 4.1.1), hence they have smaller weights, which might reduce the effect of photometric contamination on the fit.

In addition, we investigate the effect of different dust reddening laws on the *LePhare* measurements. For this, we compare a [Calzetti et al.](#) reddening with a Small Magellanic Cloud (SMC, [Prevot et al. 1984](#)) reddening. The latter might be more suitable for metal poor low-mass galaxies. Running *LePhare* with the same set-

tings but adopting a SMC reddening curve, we find only small changes in the stellar mass and SFR measurements. Specifically, for the former we find an average offset towards lower stellar masses in the case of SMC dust of 0.05 dex and a maximal offset of 0.2 dex. For latter we find similar offsets towards lower SFRs in the case of SMC dust.

Finally, we note that the galaxy properties derived here are consistent within a factor of two with the ones published in the *COSMOS2015* catalog (based on *photometric* redshifts). We conclude this from comparing galaxies with the same spectroscopic and photometric redshift within 0.1.

4.1.3. The *ALPINE* galaxies on the $z = 5$ main-sequence and [C II] fluxes

Figure 17 summarizes the results of this section by showing the relation between stellar mass and SFR (the

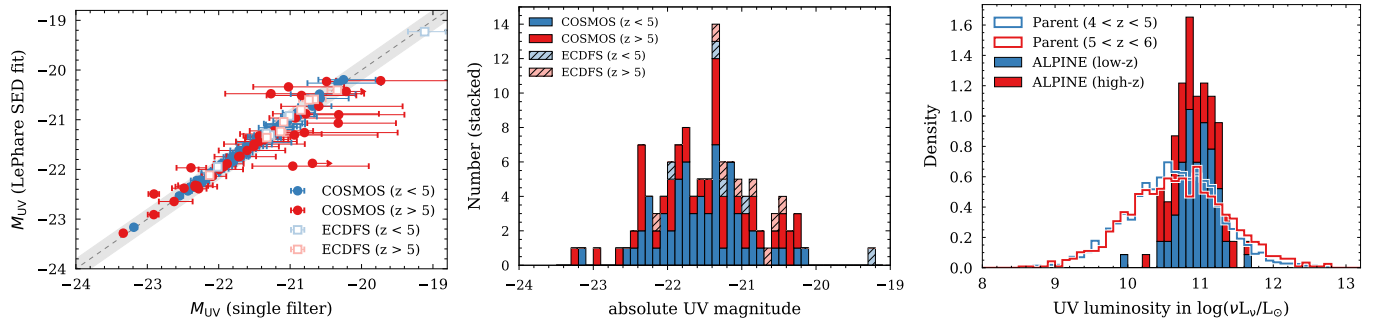


Figure 18. *Left:* Comparison of absolute UV magnitudes derived from *LePhare* and from one single filter close to rest-frame 1500 Å. The scatter at fainter magnitudes is a S/N effect in the latter measurement. The gray stripe shows ± 0.3 magnitudes around the 1-to-1 line. *Middle:* Distribution of absolute UV magnitudes of the whole *ALPINE* sample. *Right:* The UV luminosity distribution of *ALPINE* galaxies in relation to a parent sample from the *COSMOS2015* catalog selected in the same redshift range. *ALPINE* galaxies occupy brighter luminosity, caused by the selection in M_{UV} (see Section 2.1).

main-sequence) of our *ALPINE* galaxies together with the [C II] emission (in Jy km s^{-1}) measured by ALMA (in color). The measurements are compared to all galaxies (with photometric redshifts) at $4 < z < 6$ in the *COSMOS2015* catalog (blue points) as well as the main-sequence parameterization by Speagle et al. (2014) at $z = 5$ (gray band with ± 0.3 dex width).

The comparison to the photometrically selected COSMOS parent sample indicates that the *ALPINE* sample is a fair representation of the overall population of star-forming $z > 4$ galaxies. The sample also includes at higher stellar masses galaxies that lie $2 - 3\sigma$ below the main-sequence. Note that two of these galaxies at $\log(M/M_{\odot}) \sim 10.3$ and 10.7 have contaminated Spitzer photometry, and therefore their stellar masses are upper limits. Other two galaxies at $\log(M/M_{\odot}) \sim 10.6$ and 10.9 do not show [C II] emission, which is expected if they are systems of low SFR below the main-sequence. The galaxy with [C II] detection at $\log(M/M_{\odot}) \sim 10.1$ is classified as “extended dispersion dominated” by our [C II] morpho-kinematic classification (see Le Fèvre et al. 2019) and the HST/ACS imaging suggest a clumpy morphology. Although significantly below the main-sequence, [C II] is still detected in that galaxy, perhaps indicative of dust-obscured star-formation.

The color-coding of the points suggests a [C II] emission increase along the star-forming main-sequence. Furthermore, the fraction of [C II] detected galaxies significantly drops below $\log(M/M_{\odot}) \sim 9.3$ or a SFR of less than $\sim 10 M_{\odot} \text{ yr}^{-1}$. This could be due to the effect of metallicity on the [C II] line strength by either indirectly a higher ionization state or directly through lower Carbon abundance (e.g., Narayanan et al. 2017). The relationship between star formation and [C II] emission will be studied in more detail in a forthcoming paper (Schaerer et al. in prep.).

Note that there are galaxies with a SFR of less than $\sim 10 M_{\odot} \text{ yr}^{-1}$ in our sample, contrary to our initial selection. We emphasize that the initial selection was based on the observed absolute UV magnitude and not on any property derived from SED fitting (such as SFR). This discrepancy is therefore expected within the uncertainty of measuring SFRs from SED fitting.

4.2. Measurement of UV magnitudes and luminosities

The UV luminosities and absolute UV magnitudes at rest-frame 1500 Å (not dust corrected) are measured during the SED-fitting process with *LePhare* and are defined by the transmission curve of the *GALEX* FUV filter (~ 1500 Å). As shown in Section 4.1.2, the absolute UV magnitudes measured by *LePhare* and *HyperZ* are in very good agreement.

We also compare these measurements to a more direct method by using the observed flux in a single filter that is closest to rest-frame 1500 Å (Subaru z^{++} filter at $z < 5$ and UltraVISTA Y or Y_{HSC} band at $z > 5$ for galaxies in COSMOS and the HST filter $F850LP$ for all the galaxies in ECDFS). The left panel in Figure 18 shows a very good agreement between the two methods. The scatter is mainly due to the low S/N of the single-filter measurements of the second method (indicated by the large error bars). The scatter is enhanced for galaxies at $z > 5$ also due to the fact that the UltraVISTA Y -band observations are less deep than the z^{++} observations used for $z < 5$ galaxies. In the following, we will use the more robust absolute UV magnitude from *LePhare* as they depend less on the S/N of single observations.

The middle panel in Figure 18 shows the distribution of absolute UV magnitudes for galaxies in the COSMOS and ECDFS fields in two redshift bins as in the previous figures. The bulk of galaxies are between M_{UV} of -22.7 and -20.2 (consistent with the faint absolute UV mag-

nitude limit of the survey, see Section 1.2). One of the galaxies in ECDFS (*CANDELS_GOODSS_37*) is significantly fainter ($M_{UV} = -19.2$). This galaxy has been added to the sample to fill in an empty frequency window. The measurement of the absolute UV magnitude from single band and SED fit agree and the galaxy is compact and isolated (i.e., no contamination in the photometry). The fit to its photometry with *LePhare* suggests a dust-free, low-mass ($\log(M/M_{\odot}) = 9.22$) galaxy that is forming stars at a rate typical for the main-sequence ($\log(\text{SFR}/[M_{\odot} \text{ yr}^{-1}]) = 0.97$).

The right panel of Figure 18 compares the distribution of the UV luminosity of the *ALPINE* galaxies (stacked filled histogram for low and high redshift) to the same parent sample selected from the *COSMOS2015* catalog and used in Figure 17 split in two redshift bins (empty histogram). As expected, the absolute UV magnitude cut applied for the selection of the *ALPINE* sample (see Section 2.1) causes a bias towards the brighter end of the parent distribution.

4.3. UV continuum slopes

4.3.1. Method

The UV continuum slope (β , defined as $f_{\lambda} \propto \lambda^{\beta}$) generally correlates with the attenuation of stellar light by dust and is therefore an important tool to study the dust properties of galaxies especially at high redshifts (e.g., Meurer et al. 1999; Bouwens et al. 2009; Finkelstein et al. 2012). The UV continuum slope of a galaxy can be derived by various methods. Here, we compute β from the best-fit SEDs derived by *LePhare*. Compared to deriving the slopes directly from the observed photometry by a linear fit, this approach results in less biased β measurements in the case of low S/N observations (e.g., Finkelstein et al. 2012; Barisic et al. 2017). This is particularly true for the *ALPINE* galaxies, whose rest-frame UV continuum is predominantly covered by relatively shallow ground-based imaging. Deep HST coverage by a sufficient number of bands of this wavelength range is only available for a small fraction of the galaxies.

The β slopes are derived by a robust linear fit (to avoid the fit being affected by any absorption or emission lines) to the logarithmic slope of the best-fit *LePhare* SED in the wavelength range between 1300 Å and 2300 Å. To quantify uncertainties, we perturb the fluxes of each filter according to their individual errors assuming a Gaussian error distribution, refit the galaxies, and re-measure β from the resultant best-fit SED. For each galaxy we repeat this procedure 1000 times to produce a probability density function. The uncertainties for β quoted

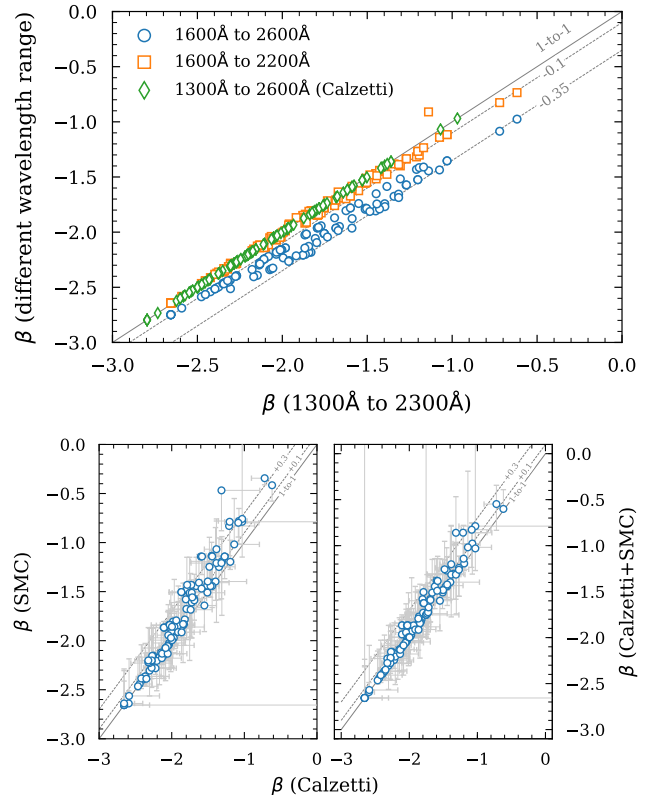


Figure 19. Dependence of UV continuum slope β on the definition of the wavelength regions and assumption of dust attenuation law. The solid line shows the 1-to-1 relation and the dashed lines show different offsets. *Top:* Dependence of β on the adopted wavelength window (with respect to our choice, 1300 Å to 2300 Å). *Bottom:* Dependence of β on the assumed dust attenuation law. Using an SMC dust attenuation results in redder slopes compared to a Calzetti reddening law.

here are the 1σ percentiles of this distribution and are on average on the order of $\Delta\beta = 0.2 - 0.3$.

4.3.2. Systematic Uncertainties and Dependencies on Dust Attenuation

In addition to photometric uncertainties, several model assumptions affect the measurement of β . We found that the two most important ones are the wavelength range over which β is fit and the assumed dust attenuation law.

We choose the wavelength range over which β is measured to be consistent with the definition of several other studies (Calzetti et al. 1994; Meurer et al. 1999; Finkelstein et al. 2012; Bouwens et al. 2014; Barisic et al. 2017; Fudamoto et al. 2017). In the upper panel of Figure 19, we demonstrate how the β measured for our *ALPINE* galaxies would change if different wavelength ranges are used. First, we do not find any differences in our measurements compared to the definition by Calzetti et al. (1994), who use 10 discrete fitting windows between

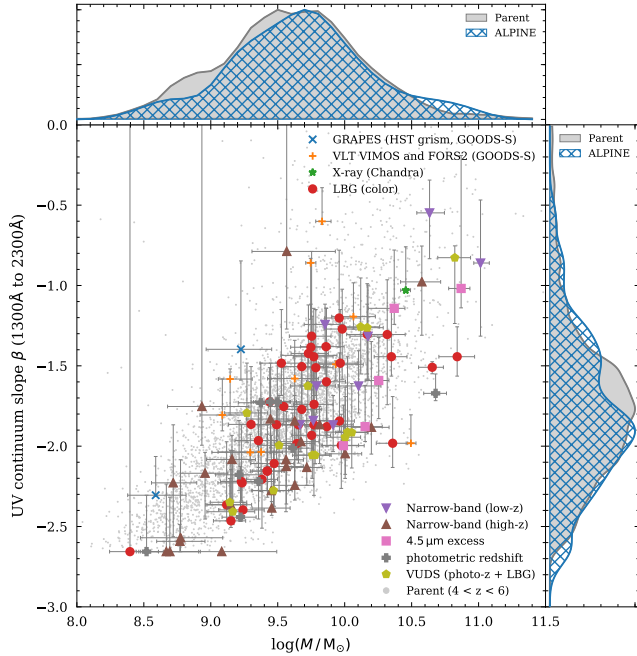


Figure 20. Comparison of UV slopes and stellar mass. The offset panels show kernel density estimates of the β and stellar mass distribution. The *ALPINE* galaxies (large symbols) are split into their method of selection (see Section 2.1). We also show the data from our parent sample at $4 < z < 5$ (gray dots). Statistically, our *ALPINE* peaks at ~ 0.2 dex higher stellar masses and ~ 0.3 bluer β .

1300 Å and 2600 Å to avoid strong absorption and emission lines (green diamonds). The other symbols show the comparison to different wavelength ranges and we notice significant offsets from our measurements. For example, defining β between 1600 Å and 2200 Å results in up to $\Delta\beta = 0.1$ bluer slopes (orange squares). Using a significantly redder wavelength range, 1600 Å to 2600 Å, leads to $0.1 - 0.35$ bluer slopes (blue circles) compared to our definition. Note that the offset varies as a function of β itself – specifically, differences are enhanced towards redder slopes.

The second, more physically driven, quantity that affects the measurement of β is the assumed dust attenuation law. As described in Section 4.1.2, the choice of the dust attenuation law has a negligible affect on the stellar masses and SFRs. This is not the case for the β slopes as shown in the lower panels of Figure 19. The left panel compares β derived using Calzetti and SMC dust attenuation. We notice a consistent positive offset of up to $\Delta\beta = 0.3$ for the reddest slopes. We compared the reduced χ^2 values output by *LePhare* for fits using a Calzetti and SMC dust attenuation in order to derive a preference for either of the dust attenuations. We find that the χ^2 values show insignificant differences,

Table 4. List of basis stellar population models for the parameterization of the rest-frame optical continuum at $4 < z < 5$ to derive $H\alpha$ emission from Spitzer colors.

| Model | SFH | Metallicity ($Z_{\odot} = 0.02$) | Dust attenuation |
|-------|-----------------------------|---------------------------------------|------------------|
| A | constant | 0.02 | Calzetti |
| B | constant | 0.004 | Calzetti |
| C | exp. declining ^a | 0.01 | Calzetti |
| D | constant | 0.02 | SMC |
| E | constant | 0.004 | SMC |
| F | exp. declining ^a | 0.01 | SMC |

^a Assuming $\tau = 3 \times 10^8$ yrs.

which lets us conclude that we are not able to distinguish between the different dust attenuations based on our SED fitting. Hence, we decided that the best way is to be agnostic about the dust attenuation and combine for each galaxy the two probability density functions $P_{\text{Calzetti}}(\beta)$ and $P_{\text{SMC}}(\beta)$ derived from our Monte Carlo approach (Section 4.3.1) assuming equal weighting to derive the median β and its 1σ uncertainties. In the lower left panel of Figure 19, the final combined β slopes are compared to the β derived assuming a Calzetti attenuation. The offset towards redder β is significantly reduced due to a narrower probability density functions assuming Calzetti dust (hence the average β are drawn to the Calzetti solution in most cases).

4.3.3. The β Slopes of the *ALPINE* Galaxies in Context

Figure 20 shows our β measurement (marginalized over both Calzetti and SMC dust) as a function of stellar mass split in the different methods of selection (Section 2.1). As the UV slope is mostly affected by the dust attenuation, the strong correlation between β and stellar mass is not surprising as more massive galaxies are expected to be more dusty. The $z \sim 5.5$ narrow-band selected galaxies have statistically the bluest slopes, indicating their dust-poor nature. The other galaxies are spread out over the whole parameter space. We also show the data from our parent sample at $4 < z < 6$ in gray and compare their β slope and stellar mass distribution to the *ALPINE* sample in the kernel density estimate plots. Note that the β slope distribution of *ALPINE* galaxies peaks at $\Delta\beta \sim 0.2$ bluer values than the parent sample at the same redshift. This is a minor bias (likely caused by our spectroscopic selection) that has to be kept in mind for future analyses.

4.4. Measurement of $H\alpha$ emission

Rest-frame optical emission lines in $z > 4$ galaxies are out of reach of current spectrographs. Specif-

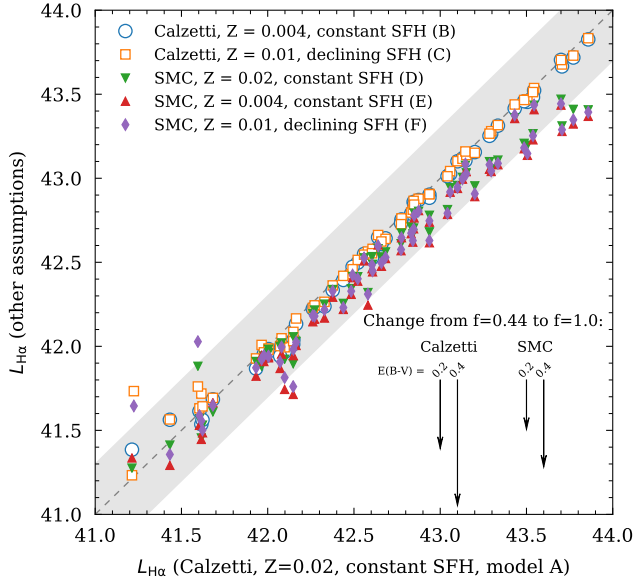


Figure 21. Effect of different assumptions of the rest-frame optical continuum, reddening law, and f -factor (arrows show absolute decrease in luminosity from $f = 0.44$ to 1.0 for different stellar dust attenuations and reddening laws) on the measurement of the $H\alpha$ luminosity. The gray band shows the 1-to-1 relation with ± 0.3 dex margin. The different models for the continuum are labeled in the same way as in Table 4). The f -factor (differential reddening between stellar continuum and nebular regions) has the strongest effect on the $H\alpha$ luminosity measurements.

ically, the $H\alpha$ emission provides a good tool to study the star-formation properties of galaxies in more detail. Fortunately, in the redshift range $4 < z < 5$, the $H\alpha$ line falls in the Spitzer $3.6 \mu\text{m}$ filter, while the $4.5 \mu\text{m}$ filter lacks any strong emission lines. Therefore, the $[3.6 \mu\text{m}] - [4.5 \mu\text{m}]$ color can be used to constrain the $H\alpha$ line flux and its equivalent width (a proxy of recent stellar mass build up). This method leads to $H\alpha$ emission properties that are statistically as accurate as derived from spectroscopic data (Faisst et al. 2016b). Several such measurements have been carried out in the past with success (Shim et al. 2011; Stark et al. 2013; de Barros et al. 2014; Smit et al. 2014; Mármol-Queraltó et al. 2016; Faisst et al. 2016b; Rasappu et al. 2016; Smit et al. 2016; Caputi et al. 2017; Faisst et al. 2019).

About 55% of the *ALPINE* sample (66 galaxies) lie in this redshift range. To measure the $H\alpha$ luminosity and equivalent widths, we follow the same technique as outlined in Faisst et al. (2019) (we refer to this paper for more technical details). In brief, this method makes an assumption on the rest-frame optical continuum to which emission lines are added in a consistent manner to reproduce the observed $[3.6 \mu\text{m}] - [4.5 \mu\text{m}]$ colors of the galaxies. This approach is robust as it only

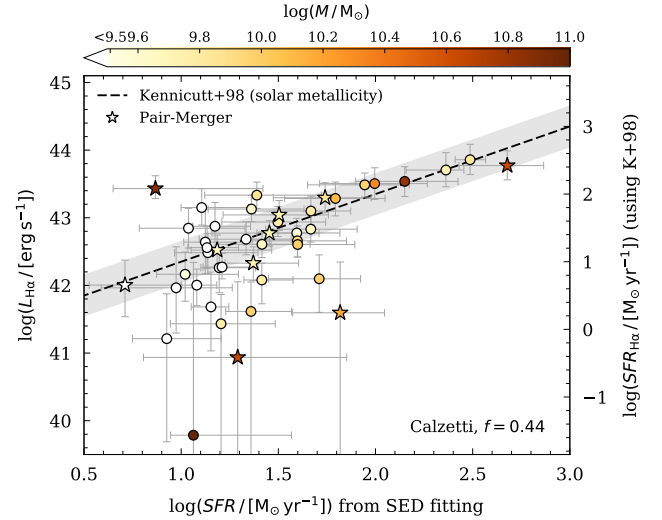


Figure 22. Comparison of SED-derived SFRs to $H\alpha$ luminosity (left y -axis) and $H\alpha$ -derived SFR (right y -axis). The latter are derived from $H\alpha$ assuming the conversion factor by Kennicutt (1998) for solar metallicity (dashed line and ± 0.3 dex margin, gray). Only galaxies with non-contaminated Spitzer photometry are shown. The symbols are color-coded by stellar mass. The star-symbols denote mergers based on the classification in Le Fèvre et al. (2019). The $H\alpha$ -dependent quantities are derived assuming a Calzetti reddening law, constant SFH, solar metallicity, and $f = 0.44$ (see Figure 21 for effect of different assumptions). Above a SFR of $\sim 13 M_{\odot} \text{yr}^{-1}$, the two SFRs are comparable. Below that threshold, the scatter in the $H\alpha$ -derived SFRs increases due to low S/N of the $4.5 \mu\text{m}$ observations (see Faisst et al. 2019).

depends on the slope of the rest-frame optical continuum, which is well defined and nearly independent of assumptions on age, metallicity, and star-formation history for galaxies younger than ~ 1 Gyrs (mostly the case at $z > 4$). To describe the rest-frame optical continuum, we use several basis stellar population models based on the Bruzual & Charlot (2003) template library (see Table 4). For the dust correction of the $H\alpha$ emission, we assume the stellar $E_s(B - V)$ values derived by LePhare, which we convert to nebular extinction factors by assuming an f -factor²⁰ of 0.44 as measured in local starburst galaxies (Calzetti et al. 2000). We also assume a Calzetti and SMC reddening law. Furthermore,

²⁰ The f -factor, $f = E_s(B - V) / E_n(B - V)$, describes the differential dust reddening between the stellar continuum and nebular regions. Its value is largely unknown at $z > 2$, but it is expected that f approaches a value closer to unity at higher redshifts (Erb et al. 2006; Reddy et al. 2010; Kashino et al. 2013; Koyama et al. 2015; Valentino et al. 2015; Puglisi et al. 2016; Kashino et al. 2017; Faisst et al. 2019).

we assume an $[\text{N II}]$ to $\text{H}\alpha$ ratio of 0.15, as expected for galaxies at $\log(M/M_\odot) = 10$ (Faisst et al. 2018), to correct the blending of the $[\text{N II}]$ and $\text{H}\alpha$ lines.

In Figure 21, we show systematic uncertainties in the measurement of the $\text{H}\alpha$ luminosity due to the assumptions in our model for the rest-frame optical continuum and the reddening law (models *A* through *F*, see Table 4), as well as the f -factor for $E_s(B - V) = 0.2$ and 0.4. It is evident that different assumptions in metallicity and SFH have a negligible impact on the measured $\text{H}\alpha$ luminosity. The choice of the reddening law matters as the $\text{H}\alpha$ luminosity decreases by ~ 0.3 dex for galaxies at high $\text{H}\alpha$ luminosities ($\log(L_{\text{H}\alpha}/L_\odot) > 43.5$) assuming an SMC reddening law. The f -factor is the largest uncertainty in this measurement method and will have to be pinned down by future observations with the JWST. For now, the assumed $f = 0.44$ provides likely an *upper* limit on the $\text{H}\alpha$ luminosities. As shown by the arrows in Figure 21, assuming an f -factor equal to unity (which is thought to be more likely based on observations at $z \sim 2$) would decrease the $\text{H}\alpha$ luminosities by up to 0.4 dex (0.8 dex) for a stellar dust reddening of 0.2 (0.4) magnitudes. The correction in case of an SMC reddening law are 0.1 – 0.2 dex less. We note that these factors also apply to $\text{H}\alpha$ -derived SFRs and any other quantity that depends linearly on the $\text{H}\alpha$ luminosity.

The top panel of Figure 22 compares the SFRs derived from SED fitting (Section 4.1) to the $\text{H}\alpha$ luminosity and $\text{H}\alpha$ -derived SFRs for galaxies without contaminated Spitzer photometry. The latter is derived using the standard conversion factor given in Kennicutt (1998),

$$\text{SFR} (M_\odot \text{ yr}^{-1}) = 4.5 \times 10^{-42} L_{\text{H}\alpha} (\text{erg s}^{-1}), \quad (5)$$

assuming solar metallicity and a Chabrier IMF. Assuming one-fifth solar metallicity, the inferred SFR is expected to be ~ 0.2 dex lower (Ly et al. 2016). As shown in Faisst et al. (2019), the uncertainty of this conversion factor is negligible compared to the impact of the uncertain f -factor. The $\text{H}\alpha$ luminosities in the *ALPINE* sample range from $\sim 10^{41} L_\odot$ to $\sim 10^{44} L_\odot$ assuming $f = 0.44$ and Calzetti dust. The $\text{H}\alpha$ -derived SFRs trace well the SED-derived SFRs above $\sim 13 M_\odot \text{ yr}^{-1}$. Below that value, we see a large scatter in $\text{H}\alpha$ derived SFRs, which happens when the $\text{H}\alpha$ emission becomes too faint to be measured reliably using the Spitzer broad bands. Specifically, this is the case roughly at $\log(M/M_\odot) = 9.5$, which corresponds to a $4.5 \mu\text{m}$ detection of less than 5σ (see figure 3 and appendix in Faisst et al. 2019).

Figure 23 shows the rest-frame $\text{H}\alpha$ EW distribution of our *ALPINE* galaxies in the context of local galaxies

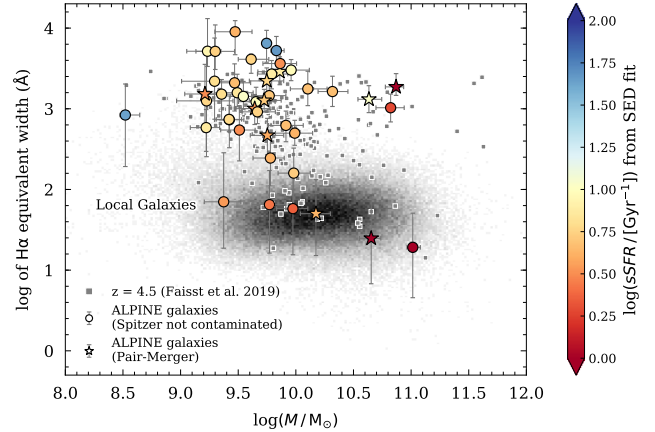


Figure 23. The rest-frame $\text{H}\alpha$ EW of our *ALPINE* galaxies in context of local galaxies (gray cloud) and $z = 4.5$ galaxies from Faisst et al. (2019) (gray squares). The $\text{H}\alpha$ EW is related to stellar mass and sSFR derived from SED fitting (color-coded). The *ALPINE* sample at $4 < z < 5$ builds a representative subsample of the general galaxy population at $z > 4$, also in terms of $\text{H}\alpha$ properties. Although with similar stellar masses as local galaxies, the high-redshift galaxies reside at significantly higher $\text{H}\alpha$ EWs, which is naturally explained by their higher star formation. Note the two galaxies with particularly low sSFR ($< 1 \text{ Gyr}^{-1}$, and consistently low $\text{H}\alpha$ EWs of less than 30 \AA) that fall onto the massive end of the distribution of local galaxies. These galaxies are indicative for systems with evolved stellar populations at high redshifts with currently reduced star formation activity.

(gray cloud) and other $z \sim 4.5$ galaxies on the COSMOS field (gray, Faisst et al. 2019). The $\text{H}\alpha$ EW for the $z > 4$ galaxies is derived consistently assuming a constant SFH, Calzetti reddening law, and $f = 0.44$. The *ALPINE* galaxies cover well the parameter space of the other $z \sim 4.5$ galaxies, hence build a representative sample also in terms of $\text{H}\alpha$ properties. For a fixed stellar mass, the high-redshift galaxies have higher $\text{H}\alpha$ EWs compared to local galaxies, which is expected from a galaxy evolution point of view as galaxies at higher redshift are highly star forming. Note that two galaxies in the *ALPINE* sample have similar $\text{H}\alpha$ EW values as massive ($\log(M/M_\odot) > 10.5$) local galaxies. Consistently, also their sSFR are low ($< 1 \text{ Gyr}^{-1}$), which is indicative of them being systems with evolved stellar populations at high redshifts.

5. SUMMARY AND CONCLUSIONS

The early growth phase at redshifts $z = 4 - 6$ marks an important time in which galaxies build up their stellar mass, enrich in metals and dust, and change their structure to transform into galaxies at the peak of SFR density or thereafter. For a better understanding of this interesting galaxy population, a multi-wavelength sur-

vey is crucial. *ALPINE* comprises a valuable set of 118 galaxies at $4.4 < z < 5.9$ with unprecedented ALMA data at $\sim 150 \mu\text{m}$ FIR wavelengths. Together with the ancillary data presented in this paper, it makes it the first large panchromatic survey to discover the formation and study the evolution of galaxies during the early growth phase.

Summarizing, the science enabling corner stone datasets of *ALPINE* are:

- unprecedented ALMA observations to study the dust, gas, and outflow properties of the largest sample of galaxies to-date at $z > 4$ (Bethérmin et al. in prep.),
- consistently calibrated deep spectroscopic observations at rest-frame UV wavelengths (§2) to study Ly α emission and absorption lines (§2.4, 2.4.2),
- coherent ground-based (and space-based in ECDFS) imaging data from the optical to near-IR (§3) for the measurement of various properties from SED fitting methods (§4.1), including stellar masses and SFRs (§4.1.1), UV luminosities (§4.2), and UV continuum slopes to study stellar dust attenuation (§4.3),
- deep Spitzer imaging at $3.6 \mu\text{m}$ and $4.5 \mu\text{m}$ to measure H α emission for 66 galaxies between $4 < z < 5$ (§4.4),
- high-resolution HST/ACS imaging in *F814W* for all galaxies and WFC3/IR imaging for a smaller fraction (less than 30% with deep *F160W* data) to study their resolved structure in connection with FIR [CII] emission (§3).

The *ALPINE* sample is built upon several different selection methods (Section 2.1, Figure 2), hence contains a multitude of different spectroscopic properties. Because of the requirement for spectroscopic confirmation, the sample is slightly biased towards brighter UV magnitudes (Section 4.2, Figure 18) and blue UV continuum slopes ($\Delta\beta \sim 0.2$) compared to the average $4 < z < 6$ galaxy population (Section 4.3, Figure 20). Nonetheless, stellar masses and SFRs, derived from the wealth of ancillary data, show that the *ALPINE* sample is broadly representative of the $4 < z < 6$ galaxy population.

The FIR [CII] redshifts observed by ALMA allow us to set the systemic redshift of the galaxies in order to study velocity offsets of Ly α emission and several rest-frame UV absorption lines (Section 2.4). From one galaxy at $z = 4.57$ with optical [OII] measurements acquired from Keck/MOSFIRE, we show that the [OII] and FIR [CII] redshifts are in excellent agreement, hence the latter likely is a good tracer of the systemic redshift derived by optical emission lines at lower redshifts (Sec-

tion 2.4.3, Figure 10). In general concordance with studies at $z = 2-3$ (using H α to define the systemic redshift), we find that on average Ly α is red shifted ($\sim 180 \text{ km s}^{-1}$) with respect to the [CII] line, while the absorption lines are blue shifted ($\sim -230 \text{ km s}^{-1}$). In Cassata et al. (2019, in prep.), we perform a more detailed comparison to samples at lower redshifts and study the implication on the Ly α escape fraction in correlation with Ly α equivalent widths. Stacking the spectra in bins of sSFR, we find larger velocity offsets of absorption lines with respect to systemic for galaxies with high sSFRs, which is indicative of stronger winds and outflows in these galaxies (Section 2.4.2, Figure 9). This finding is in agreement with the recent work by Ginolfi et al. (2019), who show a broadening in the FIR [CII] profiles in *ALPINE* galaxies with high star formation.

Statistically, the SFRs derived from H α emission via the Kennicutt (1998) relation for galaxies between $4 < z < 5$ agree well with the values derived from SED fitting, assuming a differential dust reddening factor of $f = 0.44$ (Section 4.4, Figure 22). However, we observe a considerable scatter for fainter galaxies ($\log(M/M_{\odot}) < 9.5$) due to the lower S/N of the Spitzer observations.

ALPINE is the beginning of a thorough exploration of galaxies at $z > 4$. It builds the foundation onto which future follow-up observations can build on. In fact, several follow-up programs are being granted, some of which are already on going. These include (i) additional HST WFC3/IR observations of interacting *ALPINE* galaxies (PI: Faisst), (ii) follow up observations of [NII] at $205 \mu\text{m}$ with ALMA for 9 *ALPINE* galaxies (PI: Faisst), (iii) high spatial resolution ($\sim 0.15''$) observations of the brightest *ALPINE* galaxies (PI: Ibar), and (iv) the follow up of four serendipitous objects at $z > 4$ with NOEMA (PI: Loiacono & Béthermin). In addition, several JWST proposals are in preparation.

All ancillary data products (including catalogs, images, and spectra) will be made public accessible. In the Appendix A, we detail the layout of the catalogs including the measurements detailed in this paper. In Appendix B, we show HST cutouts in ACS *F814W* and WFC3/IR *F160W* bands as well as the rest-frame UV spectra of all individual *ALPINE* galaxies.

This paper completes a series of three papers presenting the *ALPINE* survey (Le Fèvre et al. 2019) and the data processing (Bethérmin et al. in prep.).

Acknowledgements: We would like to thank numerous people for the exchange of data without which the *ALPINE* ancillary data paper would not exist. Especially we would like to thank E. Vanzella for helping us gathering the spectra in the ECDFS field

and O. Ilbert for useful discussions that improved the SED fitting results. This paper is based on data obtained with the ALMA Observatory, under Large Program 2017.1.00428.L. ALMA is a partnership of ESO (representing its member states), NSF(USA) and NINS (Japan), together with NRC (Canada), MOST and ASIAA (Taiwan), and KASI (Republic of Korea), in cooperation with the Republic of Chile. The Joint ALMA Observatory is operated by ESO, AUI/NRAO and NAOJ. This program receives funding from the CNRS national program Cosmology and Galaxies. This work is based on observations and archival data made with the Spitzer Space Telescope, which is operated by the Jet Propulsion Laboratory, California Institute of Technology, under a contract with NASA along with archival data from the NASA/ESA Hubble Space Telescope. This research made also use of the NASA/IPAC Infrared Science Archive (IRSA), which is operated by the Jet Propulsion Laboratory, California Institute of Technology, under contract with the National Aeronautics and Space Administration. In parts based on data products from observations made with ESO Telescopes at the La Silla Paranal Observatory under ESO programme ID 179.A-2005 and on data products produced by TERAPIX and the Cambridge Astronomy Survey Unit on behalf of the UltraVISTA consortium. Based on data obtained with the European Southern Observatory Very Large Telescope, Paranal, Chile, under Large Program 185.A-0791, and made available by the VUDS team at the CESAM data center, Laboratoire d'Astrophysique de Marseille, France. This work is based on observations taken by the 3D-HST Treasury Program (GO 12177 and 12328) with the NASA/ESA HST, which is operated by the Association of Universities for Research in Astronomy, Inc., under NASA contract NAS5-26555. Furthermore, this work is based on data from the W.M. Keck Observatory and the Canada-France-Hawaii Telescope, as well as collected at the Subaru Telescope and retrieved from the HSC data archive system, which is operated by the Subaru Telescope and Astronomy Data Center at the National Astronomical Observatory of Japan. The authors wish to recognize and acknowledge the very significant cultural role and reverence that the summit of Mauna Kea has always had within the indigenous Hawaiian community. We are most fortunate to have the opportunity to conduct observations from this mountain. Finally, we would also like to recognize the contributions from all of the members of the COSMOS Team who helped in obtaining and reducing the large amount of multi-wavelength data that are now publicly available through IRSA at <http://irsa.ipac.caltech.edu/Missions/cosmos.html>. A.C., F.P., M.T., C.G., and F.L. acknowledge the support from grant PRIN MIUR 2017. G.C.J. acknowledges ERC Advanced Grant 695671 "QUENCH" and support by the Science and Technology Facilities Council (STFC). E.I. acknowledges partial support from FONDECYT through grant Nbr 1171710. The Cosmic Dawn Center (DAWN) is funded by the Danish National Research Foundation under grant No. 140. S.T. acknowledges support from the ERC Consolidator Grant funding scheme (project Context, grant No. 648179). LV acknowledges funding from the European Unions Horizon 2020 research and innovation program under the Marie Skłodowska-Curie Grant agreement No. 746119. D.R. acknowledges support from the National Science Foundation under grant numbers AST-1614213 and AST-1910107 and from the Alexander von Humboldt Foundation through a Humboldt Research Fellowship for Experienced Researchers.

APPENDIX

A. DESCRIPTION OF PUBLISHED DATA PRODUCTS

The data presented in this paper are summarized in three different catalogs.

- The *main catalog*, which contains properties consistently measured for all the galaxies. These include general information (such as coordinates, redshifts, selection, morphological class), measurements performed on the spectra (such as Ly α redshift and properties as well as absorption line redshifts), measurements from SED fitting (including UV continuum slopes), and H α line properties and SFRs.
- The *ECDFS photometry catalog*, which contains all the Galactic extinction corrected total photometry (magnitude, fluxes, and uncertainties) of the galaxies in the ECDFS field. This catalog is based on the *3D-HST* catalog.
- The *COSMOS photometry catalog*, which contains all the Galactic extinction corrected total photometry (magnitude, fluxes, and uncertainties) of the galaxies in the COSMOS field. This catalog is based on the *COSMOS2015* catalog.

The following Tables A.1, A.3, and A.2 summarize the columns of each of these three catalogs. The catalogs can be downloaded in *FITS* format at [This link will be available in the accepted version of this paper].

Table A.1. Column description of main catalog. Sections of this paper where the measurements are discussed are indicated.

| Column | Unit | Description |
|--|---------------------|--|
| General information and selection | | |
| ALPINE_ID | - | Unique name for each galaxy in string format |
| RA | <i>degrees</i> | Right-ascension in J2000 in degrees from either the COSMOS or 3D-HST catalog |
| delta_RA | <i>milli-arcsec</i> | Constant shift (to be added to RA) in right-ascension due to astrometric offset (see Section 3.3) |
| DEC | <i>degrees</i> | Declination in J2000 in degrees from either the COSMOS or 3D-HST catalog |
| delta_DEC | <i>milli-arcsec</i> | Constant shift (to be added to DEC) in declination due to astrometric offset (see Section 3.3) |
| field | - | Field name (1 = ECDFS or 2 = COSMOS) |
| selection | - | Original selection. For galaxies in the ECDFS field, this can be <i>vlt</i> or <i>grapes</i> . For galaxies in COSMOS, possible selections are <i>CHANDRA</i> , <i>LBG</i> , <i>NB1^a</i> , <i>NB2^a</i> , <i>excess</i> , <i>photz</i> , or <i>vuds</i> . See Section 2.1 and Table 1 for details. |
| z_orig | - | Original redshift used for initial selection (this redshift is derived from Ly α or absorption lines). |
| z_cii | - | Redshift determined from FIR [CII] emission lines (see details in Bethermin et al. in prep.). Is -99 if [CII] is not detected at S/N > 3.5. |
| morph_class | - | Morpho-kinematic classes from Le Fèvre et al. (2019) . Only for galaxies with > 3.5 σ [CII] detection (else class set to -99). The classes are: (1) rotator; (2) pair-merger (major or minor); (3) extended dispersion dominated; (4) compact dispersion dominated; (5) too weak for assigning a class. |
| Measurements on spectra (Section 2) | | |
| has_twin | - | A flag set to 1 if for a galaxy has been observed by Keck/DEIMOS and VUDS (two spectra available). If false, the flag is set to 0. |
| z_lya | - | Redshift determined from peak of Ly α emission (see details in Cassata et al. 2019, in prep.). Is -99 if no redshift measured. |

Continued on next page

Table A.1 – *Continued from previous page*

| Column Name | Unit | Description |
|---|-----------------------------|---|
| lya_ew | Å | Observer-frame Ly α emission equivalent (see details in Cassata et al. 2019, in prep.). Is -99 if no equivalent width is measured. |
| flag_specpro | - | Visual flag for reliability of absorption redshift measurements. Set to -99 if not attempted, then 1, 2, and 3 for least, medium, and most robust. |
| z_iswind | - | Redshift determined from IS+wind absorption lines (see Section 2.4). Set to -99 if no redshift measured. |
| z_iswind_low | - | Lower 95% percentile of redshift determined from IS+wind absorption lines. Set to -99 if no redshift measured. |
| z_iswind_up | - | Upper 95% percentile of redshift determined from IS+wind absorption lines. Set to -99 if no redshift measured. |
| n_lines_iswind_used | - | Number of lines used for IS+wind redshift measurement. We advice to generally only use galaxies with a value > 2 together with <code>flag_specpro</code> > 0 for a conservative sample selection. |
| z_wind | - | Redshift determined from wind absorption lines (see Section 2.4). Set to -99 if no redshift measured. |
| z_wind_low | - | Lower 95% percentile of redshift determined from wind absorption lines. Set to -99 if no redshift measured. |
| z_wind_up | - | Upper 95% percentile of redshift determined from wind absorption lines. Set to -99 if no redshift measured. |
| n_lines_wind_used | - | Number of lines used for wind redshift measurement. We advice to generally only use galaxies with a value > 0 together with <code>flag_specpro</code> > 0 for a conservative sample selection. |
| Properties from SED fitting with LePhare (Sections 4.1 and 4.2) | | |
| ID_photcat | - | ID in the photometric catalogs. This is the <i>3D-HST</i> catalog for galaxies in ECDFS and the <i>COSMOS2015</i> catalog for galaxies in COSMOS. |
| chi2 | - | χ^2 value given by the LePhare fit. |
| Nband | - | Number of bands used for SED fitting. |
| ebmv | mag | $E(B - V)$ derived from SED fitting. |
| logAge | yr | Logarithmic age |
| logAge_loweff1sig | yr | Lower 1σ limit on age in log |
| logAge_higheff1sig | yr | Upper 1σ limit on age in log |
| logMstar | M_{\odot} | Logarithmic stellar mass |
| logMstar_loweff1sig | M_{\odot} | Lower 1σ limit on stellar mass in log |
| logMstar_higheff1sig | M_{\odot} | Upper 1σ limit on stellar mass in log |
| logSFR | $M_{\odot} \text{ yr}^{-1}$ | Logarithmic SFR |
| logSFR_loweff1sig | $M_{\odot} \text{ yr}^{-1}$ | Lower 1σ limit on SFR in log |
| logSFR_higheff1sig | $M_{\odot} \text{ yr}^{-1}$ | Upper 1σ limit on SFR in log |
| logsSFR | yr^{-1} | Logarithmic sSFR |
| logsSFR_loweff1sig | yr^{-1} | Lower 1σ limit on sSFR in log |
| logsSFR_higheff1sig | yr^{-1} | Upper 1σ limit on sSFR in log |
| M_FUV | mag | Absolute rest-frame UV magnitude measured in the GALEX FUV filter (corresponding approximately to rest-frame 1500 Å) |
| UV continuum slopes (β) with different dust reddening (Section 4.3) | | |
| beta_med_calz | - | UV slope measured assuming Calzetti dust |
| beta_low1sig_calz | - | Lower 1σ UV slope limit (Calzetti dust) |
| beta_high1sig_calz | - | Upper 1σ UV slope limit (Calzetti dust) |
| beta_med_smc | - | UV slope measured assuming SMC dust |
| beta_low1sig_smc | - | Lower 1σ UV slope limit (SMC dust) |

Continued on next page

Table A.1 – *Continued from previous page*

| Column Name | Unit | Description |
|---|-----------------------------|--|
| beta_high1sig_smc | – | Upper 1σ UV slope limit (SMC dust) |
| beta_med_comb | – | UV slope measured by marginalizing over Calzetti and SMC dust |
| beta_low1sig_comb | – | Lower 1σ UV slope limit (Calzetti+SMC dust) |
| beta_high1sig_comb | – | Upper 1σ UV slope limit (Calzetti+SMC dust) |
| Hα measurements from Spitzer colors (using Model A, see Section 4.4) | | |
| spitzer_cont | – | Spitzer photometry contamination flag. Set to 0, 1, and 2 for no, slight, and heavy contamination, respectively. |
| ewha_med | \AA | Rest-frame H α equivalent width assuming Calzetti et al. (2000) dust attenuation and $f = 0.44$ |
| ewha_low | \AA | Lower 1σ limit of rest-frame H α equivalent width |
| ewha_up | \AA | Upper 1σ limit of rest-frame H α equivalent width |
| log_halum_med | erg s^{-1} | Logarithmic H α luminosity assuming Calzetti et al. (2000) dust attenuation and $f = 0.44$ |
| log_halum_low | erg s^{-1} | Lower 1σ limit of H α luminosity in log |
| log_halum_up | erg s^{-1} | Upper 1σ limit of H α luminosity in log |
| log_sfrha_med | $M_{\odot} \text{ yr}^{-1}$ | Logarithmic SFR based on H α luminosity. Derived assuming (Kennicutt 1998) (solar metallicity), Calzetti et al. (2000) dust attenuation, and $f = 0.44$ |
| log_sfrha_low | $M_{\odot} \text{ yr}^{-1}$ | Lower 1σ limit of H α based SFR in log |
| log_sfrha_up | $M_{\odot} \text{ yr}^{-1}$ | Upper 1σ limit of H α based SFR log |

^aNote that *NB1* and *NB2* stand for the narrow-band selection of galaxies at $z \sim 4.5$ and $z \sim 5.7$, respectively.

Table A.2. Column description of the photometry catalog for galaxies in the ECDFS field (Section 3.1). Wavelengths, depths, and references are given in Table 2.

| Column | Unit | Description |
|---|----------------|---|
| ALPINE_ID | - | Unique name for each galaxy in string format |
| id_3dhst | - | Unique identification number in the <i>3D-HST</i> catalog |
| ra_3dhst | <i>degrees</i> | Right-ascension as given in <i>3D-HST</i> catalog |
| dec_3dhst | <i>degrees</i> | Declination as given in <i>3D-HST</i> catalog |
| Galactic extinction corrected total fluxes with 1σ uncertainty | | |
| f_f160w | μJy | HST/WFC3 <i>F160</i> flux and uncertainty |
| e_f160w | μJy | . |
| f_u38 | μJy | MPG-ESO/WFI <i>U</i> -band flux and uncertainty |
| e_u38 | μJy | . |
| f_u | μJy | VLT/VIMOS <i>U</i> -band flux and uncertainty |
| e_u | μJy | . |
| f_f435w | μJy | HST/ACS <i>F435W</i> flux and uncertainty |
| e_f435w | μJy | . |
| f_b | μJy | MPG-ESO/WFI <i>b</i> -band flux and uncertainty |
| e_b | μJy | . |
| f_v | μJy | MPG-ESO/WFI <i>v</i> -band flux and uncertainty |
| e_v | μJy | . |
| f_f606wcand | μJy | HST/ACS <i>F606W</i> flux and uncertainty (from CANDELS) |
| e_f606wcand | μJy | . |

Continued on next page

Table A.2 – *Continued from previous page*

| Column Name | Unit | Description |
|--------------|----------|---|
| f_f606w | μJy | HST/ACS <i>F606W</i> flux and uncertainty |
| e_f606w | μJy | . |
| f_r | μJy | VLT/VIMOS <i>r</i> -band flux and uncertainty |
| e_r | μJy | . |
| f_rc | μJy | MPG-ESO/WFI <i>r</i> -band flux and uncertainty |
| e_rc | μJy | . |
| f_f775w | μJy | HST/ACS <i>F775W</i> flux and uncertainty |
| e_f775w | μJy | . |
| f_i | μJy | MPG-ESO/WFI <i>i</i> -band flux and uncertainty |
| e_i | μJy | . |
| f_f814wcand | μJy | HST/ACS <i>F814W</i> flux and uncertainty (from CANDELS) |
| e_f814wcand | μJy | . |
| f_f850lp | μJy | HST/ACS <i>F850LP</i> flux and uncertainty |
| e_f850lp | μJy | . |
| f_f850lpcand | μJy | HST/ACS <i>F850LP</i> flux and uncertainty (from CANDELS) |
| e_f850lpcand | μJy | . |
| f_f125w | μJy | HST/WFC3 <i>F125W</i> flux and uncertainty |
| e_f125w | μJy | . |
| f_j | μJy | VLT/ISAAC <i>J</i> -band flux and uncertainty |
| e_j | μJy | . |
| f_tenisj | μJy | CFHT/WIRCam <i>J</i> -band flux and uncertainty |
| e_tenisj | μJy | . |
| f_f140w | μJy | HST/WFC3 <i>F140W</i> flux and uncertainty |
| e_f140w | μJy | . |
| f_h | μJy | VLT/ISAAC <i>H</i> -band flux and uncertainty |
| e_h | μJy | . |
| f_tenisk | μJy | CFHT/WIRCam <i>K</i> -band flux and uncertainty |
| e_tenisk | μJy | . |
| f_ks | μJy | VLT/ISAAC <i>K</i> -band flux and uncertainty. |
| e_ks | μJy | . |
| f_irac1 | μJy | Spitzer/IRAC 3.6 μm flux and uncertainty |
| e_irac1 | μJy | . |
| f_irac2 | μJy | Spitzer/IRAC 4.5 μm flux and uncertainty |
| e_irac2 | μJy | . |
| f_irac3 | μJy | Spitzer/IRAC 5.8 μm flux and uncertainty |
| e_irac3 | μJy | . |
| f_irac4 | μJy | Spitzer/IRAC 8.0 μm flux and uncertainty |
| e_irac4 | μJy | . |
| f_ia427 | μJy | Subaru/Suprime-Cam <i>IA427</i> flux and uncertainty |
| e_ia427 | μJy | . |
| f_ia445 | μJy | Subaru/Suprime-Cam <i>IA445</i> flux and uncertainty |
| e_ia445 | μJy | . |
| f_ia505 | μJy | Subaru/Suprime-Cam <i>IA505</i> flux and uncertainty |
| e_ia505 | μJy | . |
| f_ia527 | μJy | Subaru/Suprime-Cam <i>IA527</i> flux and uncertainty |
| e_ia527 | μJy | . |
| f_ia550 | μJy | Subaru/Suprime-Cam <i>IA550</i> flux and uncertainty |

Continued on next page

Table A.2 – *Continued from previous page*

| Column Name | Unit | Description |
|-------------|----------|---|
| e_ia550 | μJy | . |
| f_ia574 | μJy | Subaru/Suprime-Cam IA574 flux and uncertainty |
| e_ia574 | μJy | . |
| f_ia598 | μJy | Subaru/Suprime-Cam IA598 flux and uncertainty |
| e_ia598 | μJy | . |
| f_ia624 | μJy | Subaru/Suprime-Cam IA624 flux and uncertainty |
| e_ia624 | μJy | . |
| f_ia651 | μJy | Subaru/Suprime-Cam IA651 flux and uncertainty |
| e_ia651 | μJy | . |
| f_ia679 | μJy | Subaru/Suprime-Cam IA679 flux and uncertainty |
| e_ia679 | μJy | . |
| f_ia738 | μJy | Subaru/Suprime-Cam IA738 flux and uncertainty |
| e_ia738 | μJy | . |
| f_ia767 | μJy | Subaru/Suprime-Cam IA767 flux and uncertainty |
| e_ia767 | μJy | . |
| f_ia797 | μJy | Subaru/Suprime-Cam IA797 flux and uncertainty |
| e_ia797 | μJy | . |
| f_ia856 | μJy | Subaru/Suprime-Cam IA856 flux and uncertainty |
| e_ia856 | μJy | . |

Galactic extinction corrected total magnitudes with 1σ uncertainty

Note: given are 1σ limits (and magnitude uncertainties are set to -1) if fluxes are smaller than 1σ flux uncertainties.

| | | |
|------------------|-----|--|
| mag_f160w | mag | HST/WFC3 F160 magnitude and error |
| magerr_f160w | mag | . |
| mag_u38 | mag | MPG-ESO/WFI U38-band magnitude and uncertainty |
| magerr_u38 | mag | . |
| mag_u | mag | VLT/VIMOS U-band magnitude and uncertainty |
| magerr_u | mag | . |
| mag_f435w | mag | HST/ACS F435W magnitude and uncertainty |
| magerr_f435w | mag | . |
| mag_b | mag | MPG-ESO/WFI b-band magnitude and uncertainty |
| magerr_b | mag | . |
| mag_v | mag | MPG-ESO/WFI v-band magnitude and uncertainty |
| magerr_v | mag | . |
| mag_f606wcand | mag | HST/ACS F606W magnitude and uncertainty (from CANDELS) |
| magerr_f606wcand | mag | . |
| mag_f606w | mag | HST/ACS F606W magnitude and uncertainty |
| magerr_f606w | mag | . |
| mag_r | mag | VLT/VIMOS R-band magnitude and uncertainty |
| magerr_r | mag | . |
| mag_rc | mag | MPG-ESO/WFI R _c -band magnitude and uncertainty |
| magerr_rc | mag | . |
| mag_f775w | mag | HST/ACS F775W magnitude and uncertainty |
| magerr_f775w | mag | . |
| mag_i | mag | MPG-ESO/WFI I-band magnitude and uncertainty |
| magerr_i | mag | . |
| mag_f814wcand | mag | HST/ACS F814W magnitude and uncertainty (from CANDELS) |
| magerr_f814wcand | mag | . |

Continued on next page

Table A.2 – *Continued from previous page*

| Column Name | Unit | Description |
|-------------------|------|--|
| mag_f850lp | mag | HST/ACS <i>F850LP</i> magnitude and uncertainty |
| magerr_f850lp | mag | . |
| mag_f850lpcand | mag | HST/ACS <i>F850LP</i> magnitude and uncertainty (from CANDELS) |
| magerr_f850lpcand | mag | . |
| mag_f125w | mag | HST/WFC3 <i>F125W</i> magnitude and uncertainty |
| magerr_f125w | mag | . |
| mag_j | mag | VLT/ISAAC <i>J^v</i> -band magnitude and uncertainty |
| magerr_j | mag | . |
| mag_tenisj | mag | CFHT/WIRCam <i>J_w</i> -band magnitude and uncertainty |
| magerr_tenisj | mag | . |
| mag_f140w | mag | HST/WFC3 <i>F140W</i> magnitude and uncertainty |
| magerr_f140w | mag | . |
| mag_h | mag | VLT/ISAAC <i>H^v</i> -band magnitude and uncertainty |
| magerr_h | mag | . |
| mag_tenisk | mag | CFHT/WIRCam <i>K_s^w</i> -band magnitude and uncertainty |
| magerr_tenisk | mag | . |
| mag_ks | mag | VLT/ISAAC <i>K_s^v</i> -band magnitude and uncertainty |
| magerr_ks | mag | . |
| mag_irac1 | mag | Spitzer/IRAC 3.6 μm (ch ₁) magnitude and uncertainty |
| magerr_irac1 | mag | . |
| mag_irac2 | mag | Spitzer/IRAC 4.5 μm (ch ₂) magnitude and uncertainty |
| magerr_irac2 | mag | . |
| mag_irac3 | mag | Spitzer/IRAC 5.8 μm (ch ₃) magnitude and uncertainty |
| magerr_irac3 | mag | . |
| mag_irac4 | mag | Spitzer/IRAC 8.0 μm (ch ₄) magnitude and uncertainty |
| magerr_irac4 | mag | . |
| mag_ia427 | mag | Subaru/Suprime-Cam <i>IA427</i> magnitude and uncertainty |
| magerr_ia427 | mag | . |
| mag_ia445 | mag | Subaru/Suprime-Cam <i>IA445</i> magnitude and uncertainty |
| magerr_ia445 | mag | . |
| mag_ia505 | mag | Subaru/Suprime-Cam <i>IA505</i> magnitude and uncertainty |
| magerr_ia505 | mag | . |
| mag_ia527 | mag | Subaru/Suprime-Cam <i>IA527</i> magnitude and uncertainty |
| magerr_ia527 | mag | . |
| mag_ia550 | mag | Subaru/Suprime-Cam <i>IA550</i> magnitude and uncertainty |
| magerr_ia550 | mag | . |
| mag_ia574 | mag | Subaru/Suprime-Cam <i>IA574</i> magnitude and uncertainty |
| magerr_ia574 | mag | . |
| mag_ia598 | mag | Subaru/Suprime-Cam <i>IA598</i> magnitude and uncertainty |
| magerr_ia598 | mag | . |
| mag_ia624 | mag | Subaru/Suprime-Cam <i>IA624</i> magnitude and uncertainty |
| magerr_ia624 | mag | . |
| mag_ia651 | mag | Subaru/Suprime-Cam <i>IA651</i> magnitude and uncertainty |
| magerr_ia651 | mag | . |
| mag_ia679 | mag | Subaru/Suprime-Cam <i>IA679</i> magnitude and uncertainty |
| magerr_ia679 | mag | . |
| mag_ia738 | mag | Subaru/Suprime-Cam <i>IA738</i> magnitude and uncertainty |

Continued on next page

Table A.2 – *Continued from previous page*

| Column Name | Unit | Description |
|--------------|------|--|
| magerr_ia738 | mag | . |
| mag_ia767 | mag | Subaru/Suprime-Cam IA767 magnitude and uncertainty |
| magerr_ia767 | mag | . |
| mag_ia797 | mag | Subaru/Suprime-Cam IA797 magnitude and uncertainty |
| magerr_ia797 | mag | . |
| mag_ia856 | mag | Subaru/Suprime-Cam IA856 magnitude and uncertainty |
| magerr_ia856 | mag | . |

Table A.3. Column description of the photometry catalog for galaxies in the COSMOS field (Section 3.2). Wavelengths, depths, and references are given in Table 3.

| Column | Unit | Description |
|---|----------|---|
| ALPINE_ID | - | Unique name for each galaxy in string format |
| id_cosmos15 | - | Unique identification number in the <i>COSMOS2015</i> catalog |
| ra_cosmos15 | degrees | Right-ascension as given in the <i>COSMOS2015</i> catalog |
| dec_cosmos15 | degrees | Declination as given in the <i>COSMOS2015</i> catalog |
| Galactic extinction corrected total fluxes with 1σ uncertainty | | |
| Ks_FLUX_APER3 | μJy | CFHT/WIRCam K_s -band flux and uncertainty |
| Ks_FLUXERR_APER3 | μJy | . |
| Y_FLUX_APER3 | μJy | VISTA/VIRCAM Y -band flux and uncertainty |
| Y_FLUXERR_APER3 | μJy | . |
| H_FLUX_APER3 | μJy | VISTA/VIRCAM H -band flux and uncertainty |
| H_FLUXERR_APER3 | μJy | . |
| J_FLUX_APER3 | μJy | VISTA/VIRCAM J -band flux and uncertainty |
| J_FLUXERR_APER3 | μJy | . |
| B_FLUX_APER3 | μJy | Subaru/Suprime-Cam B -band flux and uncertainty |
| B_FLUXERR_APER3 | μJy | . |
| V_FLUX_APER3 | μJy | Subaru/Suprime-Cam V -band flux and uncertainty |
| V_FLUXERR_APER3 | μJy | . |
| ip_FLUX_APER3 | μJy | Subaru/Suprime-Cam i^+ -band flux and uncertainty |
| ip_FLUXERR_APER3 | μJy | . |
| r_FLUX_APER3 | μJy | Subaru/Suprime-Cam r^+ -band flux and uncertainty |
| r_FLUXERR_APER3 | μJy | . |
| u_FLUX_APER3 | μJy | CFHT/MegaCam u^* -band flux and uncertainty |
| u_FLUXERR_APER3 | μJy | . |
| zp_FLUX_APER3 | μJy | Subaru/Suprime-Cam z^+ -band flux and uncertainty |
| zp_FLUXERR_APER3 | μJy | . |
| zpp_FLUX_APER3 | μJy | Subaru/Suprime-Cam z^{++} -band flux and uncertainty |
| zpp_FLUXERR_APER3 | μJy | . |
| IA484_FLUX_APER3 | μJy | Subaru/Suprime-Cam IA484-band flux and uncertainty |
| IA484_FLUXERR_APER3 | μJy | . |
| IA527_FLUX_APER3 | μJy | Subaru/Suprime-Cam IA527-band flux and uncertainty |
| IA527_FLUXERR_APER3 | μJy | . |
| IA624_FLUX_APER3 | μJy | Subaru/Suprime-Cam IA624-band flux and uncertainty |

Continued on next page

Table A.3 – *Continued from previous page*

| Column Name | Unit | Description |
|--------------------------------|----------|--|
| IA624_FLUXERR_APER3 | μJy | . |
| IA679_FLUX_APER3 | μJy | Subaru/Suprime-Cam IA679-band flux and uncertainty |
| IA679_FLUXERR_APER3 | μJy | . |
| IA738_FLUX_APER3 | μJy | Subaru/Suprime-Cam IA738-band flux and uncertainty |
| IA738_FLUXERR_APER3 | μJy | . |
| IA767_FLUX_APER3 | μJy | Subaru/Suprime-Cam IA767-band flux and uncertainty |
| IA767_FLUXERR_APER3 | μJy | . |
| IB427_FLUX_APER3 | μJy | Subaru/Suprime-Cam IA427-band flux and uncertainty |
| IB427_FLUXERR_APER3 | μJy | . |
| IB464_FLUX_APER3 | μJy | Subaru/Suprime-Cam IA464-band flux and uncertainty |
| IB464_FLUXERR_APER3 | μJy | . |
| IB505_FLUX_APER3 | μJy | Subaru/Suprime-Cam IA505-band flux and uncertainty |
| IB505_FLUXERR_APER3 | μJy | . |
| IB574_FLUX_APER3 | μJy | Subaru/Suprime-Cam IA574-band flux and uncertainty |
| IB574_FLUXERR_APER3 | μJy | . |
| IB709_FLUX_APER3 | μJy | Subaru/Suprime-Cam IA709-band flux and uncertainty |
| IB709_FLUXERR_APER3 | μJy | . |
| IB827_FLUX_APER3 | μJy | Subaru/Suprime-Cam IA827-band flux and uncertainty |
| IB827_FLUXERR_APER3 | μJy | . |
| NB711_FLUX_APER3 | μJy | Subaru/Suprime-Cam NB711-band flux and uncertainty |
| NB711_FLUXERR_APER3 | μJy | . |
| NB816_FLUX_APER3 | μJy | Subaru/Suprime-Cam NB816-band flux and uncertainty |
| NB816_FLUXERR_APER3 | μJy | . |
| SPLASH_1_FLUX | μJy | Spitzer/IRAC 3.6 μm (ch ₁) flux and uncertainty |
| SPLASH_1_FLUX_ERR | μJy | . |
| SPLASH_2_FLUX | μJy | Spitzer/IRAC 4.5 μm (ch ₂) flux and uncertainty |
| SPLASH_2_FLUX_ERR | μJy | . |
| SPLASH_3_FLUX | μJy | Spitzer/IRAC 5.8 μm (ch ₃) flux and uncertainty |
| SPLASH_3_FLUX_ERR | μJy | . |
| SPLASH_4_FLUX | μJy | Spitzer/IRAC 8.0 μm (ch ₄) flux and uncertainty |
| SPLASH_4_FLUX_ERR | μJy | . |
| H _w _FLUX_APER3 | μJy | CFHT/WIRCam H _w -band flux and uncertainty |
| H _w _FLUXERR_APER3 | μJy | . |
| K _{sw} _FLUX_APER3 | μJy | CFHT/WIRCam H _s ^w -band flux and uncertainty |
| K _{sw} _FLUXERR_APER3 | μJy | . |
| yHSC_FLUX_APER3 | μJy | Subaru/HSC Y _{HSC} -band magnitude and error |

Galactic extinction corrected total magnitudes with 1 σ uncertainty

Note: given are 1 σ limits (and magnitude uncertainties are set to -1) if fluxes are smaller than 1 σ flux uncertainties.

| | | |
|------------------------|------------|--|
| K _s _MAG | <i>mag</i> | CFHT/WIRCam K _s -band magnitude and uncertainty |
| K _s _MAGERR | <i>mag</i> | . |
| Y_MAG | <i>mag</i> | VISTA/VIRCAM Y-band magnitude and uncertainty |
| Y_MAGERR | <i>mag</i> | . |
| H_MAG | <i>mag</i> | VISTA/VIRCAM H-band magnitude and uncertainty |
| H_MAGERR | <i>mag</i> | . |
| J_MAG | <i>mag</i> | VISTA/VIRCAM J-band magnitude and uncertainty |
| J_MAGERR | <i>mag</i> | . |
| B_MAG | <i>mag</i> | Subaru/Suprime-Cam B-band magnitude and uncertainty |

Continued on next page

Table A.3 – *Continued from previous page*

| Column Name | Unit | Description |
|-----------------|------------|---|
| B_MAGERR | <i>mag</i> | . |
| V_MAG | <i>mag</i> | Subaru/Suprime-Cam <i>V</i> -band magnitude and uncertainty |
| V_MAGERR | <i>mag</i> | . |
| ip_MAG | <i>mag</i> | Subaru/Suprime-Cam <i>i</i> ⁺ -band magnitude and uncertainty |
| ip_MAGERR | <i>mag</i> | . |
| r_MAG | <i>mag</i> | Subaru/Suprime-Cam <i>r</i> ⁺ -band magnitude and uncertainty |
| r_MAGERR | <i>mag</i> | . |
| u_MAG | <i>mag</i> | CFHT/MegaCam <i>u</i> [*] -band magnitude and uncertainty |
| u_MAGERR | <i>mag</i> | . |
| zp_MAG | <i>mag</i> | Subaru/Suprime-Cam <i>z</i> ⁺ -band magnitude and uncertainty |
| zp_MAGERR | <i>mag</i> | . |
| zpp_MAG | <i>mag</i> | Subaru/Suprime-Cam <i>z</i> ⁺⁺ -band magnitude and uncertainty |
| zpp_MAGERR | <i>mag</i> | . |
| IA484_MAG | <i>mag</i> | Subaru/Suprime-Cam <i>IA484</i> -band magnitude and uncertainty |
| IA484_MAGERR | <i>mag</i> | . |
| IA527_MAG | <i>mag</i> | Subaru/Suprime-Cam <i>IA527</i> -band magnitude and uncertainty |
| IA527_MAGERR | <i>mag</i> | . |
| IA624_MAG | <i>mag</i> | Subaru/Suprime-Cam <i>IA624</i> -band magnitude and uncertainty |
| IA624_MAGERR | <i>mag</i> | . |
| IA679_MAG | <i>mag</i> | Subaru/Suprime-Cam <i>IA679</i> -band magnitude and uncertainty |
| IA679_MAGERR | <i>mag</i> | . |
| IA738_MAG | <i>mag</i> | Subaru/Suprime-Cam <i>IA738</i> -band magnitude and uncertainty |
| IA738_MAGERR | <i>mag</i> | . |
| IA767_MAG | <i>mag</i> | Subaru/Suprime-Cam <i>IA767</i> -band magnitude and uncertainty |
| IA767_MAGERR | <i>mag</i> | . |
| IB427_MAG | <i>mag</i> | Subaru/Suprime-Cam <i>IA427</i> -band magnitude and uncertainty |
| IB427_MAGERR | <i>mag</i> | . |
| IB464_MAG | <i>mag</i> | Subaru/Suprime-Cam <i>IA464</i> -band magnitude and uncertainty |
| IB464_MAGERR | <i>mag</i> | . |
| IB505_MAG | <i>mag</i> | Subaru/Suprime-Cam <i>IA505</i> -band magnitude and uncertainty |
| IB505_MAGERR | <i>mag</i> | . |
| IB574_MAG | <i>mag</i> | Subaru/Suprime-Cam <i>IA574</i> -band magnitude and uncertainty |
| IB574_MAGERR | <i>mag</i> | . |
| IB709_MAG | <i>mag</i> | Subaru/Suprime-Cam <i>IA709</i> -band magnitude and uncertainty |
| IB709_MAGERR | <i>mag</i> | . |
| IB827_MAG | <i>mag</i> | Subaru/Suprime-Cam <i>IA827</i> -band magnitude and uncertainty |
| IB827_MAGERR | <i>mag</i> | . |
| NB711_MAG | <i>mag</i> | Subaru/Suprime-Cam <i>NB711</i> -band magnitude and uncertainty |
| NB711_MAGERR | <i>mag</i> | . |
| NB816_MAG | <i>mag</i> | Subaru/Suprime-Cam <i>NB816</i> -band magnitude and uncertainty |
| NB816_MAGERR | <i>mag</i> | . |
| SPLASH_1_MAG | <i>mag</i> | Spitzer/IRAC 3.6 μm (ch ₁) magnitude and uncertainty |
| SPLASH_1_MAGERR | <i>mag</i> | . |
| SPLASH_2_MAG | <i>mag</i> | Spitzer/IRAC 4.5 μm (ch ₂) magnitude and uncertainty |
| SPLASH_2_MAGERR | <i>mag</i> | . |
| SPLASH_3_MAG | <i>mag</i> | Spitzer/IRAC 5.8 μm (ch ₃) magnitude and uncertainty |
| SPLASH_3_MAGERR | <i>mag</i> | . |

Continued on next page

Table A.3 – *Continued from previous page*

| Column Name | Unit | Description |
|-------------------------|------------|--|
| SPLASH_4_MAG | <i>mag</i> | Spitzer/IRAC 8.0 μm (ch_4) magnitude and uncertainty |
| SPLASH_4_MAGERR | <i>mag</i> | . |
| H _w _MAG | <i>mag</i> | CFHT/WIRCam H_w -band magnitude and uncertainty |
| H _w _MAGERR | <i>mag</i> | . |
| K _{sw} _MAG | <i>mag</i> | CFHT/WIRCam H_s^w -band magnitude and uncertainty |
| K _{sw} _MAGERR | <i>mag</i> | . |
| yHSC_MAG | <i>mag</i> | Subaru/HSC Y_{HSC} -band magnitude and error |
| yHSC_MAGERR | <i>mag</i> | . |

B. ADDITIONAL FIGURES

In the following, we show the imaging and spectroscopic data for the individual *ALPINE galaxies*.

Figures B.1 through B.3 show $2'' \times 2''$ cutouts of the HST *F814W* band of each of the galaxies, sorted by increasing redshift. The redshift, stellar mass, and SFR is indicated. The dashed contours show -3σ levels and the solid contours show 3σ , 5σ , 10σ , 15σ , and 30σ levels. The cutouts are oriented such that north is up and east is to the left. Similarly, Figures B.4 and B.5 show the all the available HST *F160W* data for the *ALPINE* galaxies as of October 2019. The cutout size and the drawn σ -levels are the same as in the previous figures. Note that the HST program *DASH* covers most of the galaxies, however, only a fraction is detected due to the low depth of these observations.

Figures B.6 through B.10 show the rest-frame UV spectra for each *ALPINE* galaxy sorted by increasing redshift. The spectra are smoothed with a Savitzky-Golay filter of size 2 \AA . Prominent emission lines as well as individual absorption lines and absorption line complexes are indicated by the dark-red bars (compare to Section 2.4.2). For some of the galaxies in COSMOS a spectrum obtained by VUDS and Keck/DEIMOS is available. The names of these galaxies have an appended “_v” or “_d”, respectively. Note their different spectral resolution.

REFERENCES

- Agertz, O., Teyssier, R., & Moore, B. 2009, MNRAS, 397, L64
- Aihara, H., AlSayyad, Y., Ando, M., et al. 2019, arXiv e-prints, arXiv:1905.12221
- Ando, M., Ohta, K., Iwata, I., et al. 2007, PASJ, 59, 717
- Arnouts, S., Cristiani, S., Moscardini, L., et al. 1999, MNRAS, 310, 540
- Ashby, M. L. N., Willner, S. P., Fazio, G. G., et al. 2013, ApJ, 769, 80
- Balestra, I., Mainieri, V., Popesso, P., et al. 2010, A&A, 512, A12
- Barisic et al. 2017, ApJL, submitted
- Bertin, E., & Arnouts, S. 1996, A&AS, 117, 393
- Bethermin et al. in prep.
- Bolzonella, M., Miralles, J. M., & Pelló, R. 2000, A&A, 363, 476
- Bournaud, F., Elmegreen, B. G., & Elmegreen, D. M. 2007, ApJ, 670, 237
- Bouwens, R. J., Illingworth, G. D., Franx, M., et al. 2009, ApJ, 705, 936
- Bouwens, R. J., Illingworth, G. D., Oesch, P. A., et al. 2014, ApJ, 793, 115
- . 2015, ApJ, 803, 34
- Brammer, G. B., van Dokkum, P. G., Franx, M., et al. 2012, ApJS, 200, 13
- Bruzual, G., & Charlot, S. 2003, MNRAS, 344, 1000
- Calzetti, D., Armus, L., Bohlin, R. C., et al. 2000, ApJ, 533, 682
- Calzetti, D., Kinney, A. L., & Storchi-Bergmann, T. 1994, ApJ, 429, 582
- Capak, P., Cowie, L. L., Hu, E. M., et al. 2004, AJ, 127, 180
- Capak, P., Aussel, H., Ajiki, M., et al. 2007, ApJS, 172, 99
- Capak, P., Aussel, H., Bundy, K., et al. 2012, SPLASH: Spitzer Large Area Survey with Hyper-Suprime-Cam, Spitzer Proposal, ,
- Capak, P. L., Riechers, D., Scoville, N. Z., et al. 2011, Nature, 470, 233
- Capak, P. L., Carilli, C., Jones, G., et al. 2015, Nature, 522, 455
- Caputi, K. I., Cirasuolo, M., Dunlop, J. S., et al. 2011, MNRAS, 413, 162
- Caputi, K. I., Deshmukh, S., Ashby, M. L. N., et al. 2017, ApJ, 849, 45
- Cardamone, C. N., van Dokkum, P. G., Urry, C. M., et al. 2010, ApJS, 189, 270
- Carilli, C. L., & Walter, F. 2013, ARA&A, 51, 105
- Carniani, S., Maiolino, R., Amorin, R., et al. 2018, MNRAS, 478, 1170
- Cassata et al. 2019, in prep.
- Castor, J. I., & Lamers, H. J. G. L. M. 1979, ApJS, 39, 481
- Chabrier, G. 2003, PASP, 115, 763
- Cowie, L. L., Barger, A. J., & Hu, E. M. 2011, ApJ, 738, 136
- Cullen, F., McLure, R. J., Khochfar, S., et al. 2018, MNRAS, 476, 3218
- Davidzon, I., Ilbert, O., Laigle, C., et al. 2017, A&A, 605, A70
- de Barros, S., Schaerer, D., & Stark, D. P. 2014, A&A, 563, A81
- De Looze, I., Cormier, D., Leboutteiller, V., et al. 2014, A&A, 568, A62
- Dickinson, M. 1998, in The Hubble Deep Field, ed. M. Livio, S. M. Fall, & P. Madau, 219
- Dickinson, M., Giavalisco, M., & GOODS Team. 2003, in The Mass of Galaxies at Low and High Redshift, ed. R. Bender & A. Renzini, 324

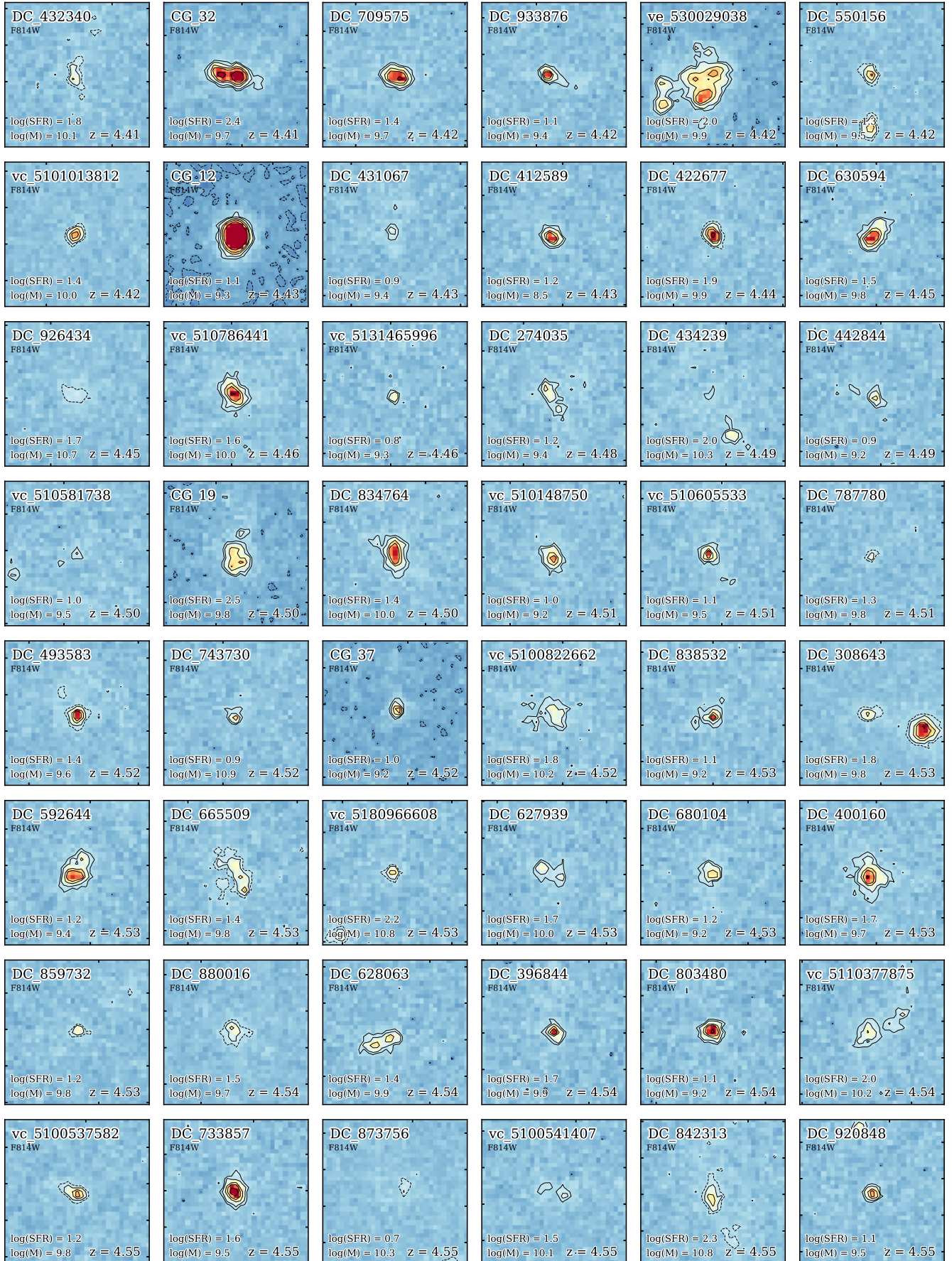
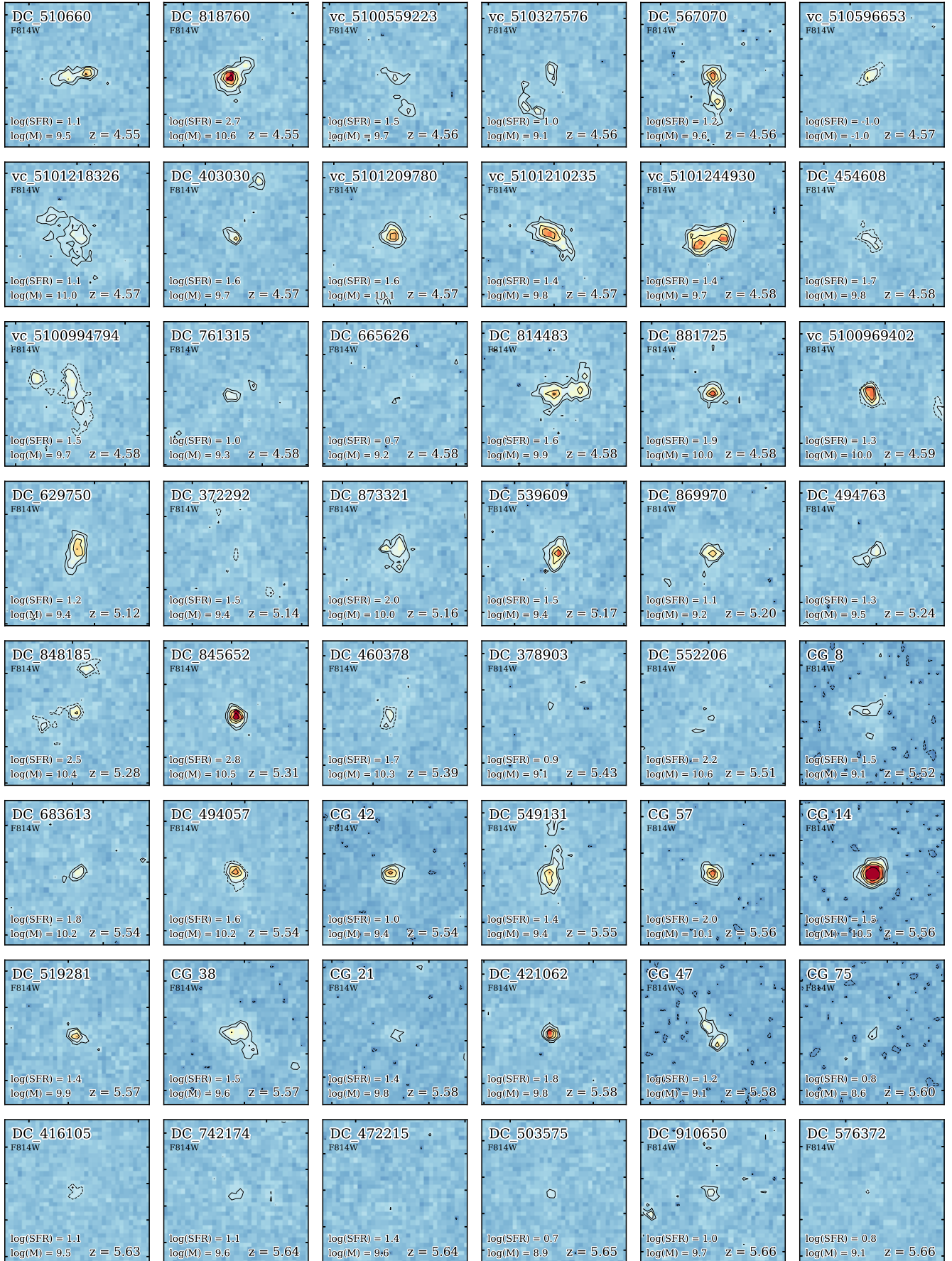


Figure B.1. $F814W$ cutouts sorted by redshift (part 1). The dashed contours show -3σ levels and the solid contours show 3σ , 5σ , 10σ , 15σ , and 30σ levels. All cutouts are $2''$ on each side.

- Dunlop, J. S., McLure, R. J., Biggs, A. D., et al. 2017, *MNRAS*, 466, 861
- Erb, D. K., Shapley, A. E., Pettini, M., et al. 2006, *ApJ*, 644, 813
- Erben, T., Schirmer, M., Dietrich, J. P., et al. 2005, *Astronomische Nachrichten*, 326, 432
- Faisst, A. L., Capak, P. L., Emami, N., Tacchella, S., & Larson, K. L. 2019, arXiv e-prints, arXiv:1909.03076
- Faisst, A. L., Masters, D., Wang, Y., et al. 2018, *ApJ*, 855, 132
- Faisst, A. L., Capak, P. L., Davidzon, I., et al. 2016a, *ApJ*, 822, 29
- Faisst, A. L., Capak, P., Hsieh, B. C., et al. 2016b, *ApJ*, 821, 122
- Faisst, A. L., Capak, P. L., Yan, L., et al. 2017, *ApJ*, 847, 21
- Ferrara, A., Vallini, L., Pallottini, A., et al. 2019, *MNRAS*, 489, 1
- Finkelstein, S. L., Papovich, C., Salmon, B., et al. 2012, *ApJ*, 756, 164
- Franco, M., Elbaz, D., Béthermin, M., et al. 2018, *A&A*, 620, A152
- Fudamoto, Y., Oesch, P. A., Schinnerer, E., et al. 2017, *MNRAS*, 472, 483
- Giacconi, R., Zirm, A., Wang, J., et al. 2002, *ApJS*, 139, 369
- Giavalisco, M., Ferguson, H. C., Koekemoer, A. M., et al. 2004, *ApJL*, 600, L93
- Ginolfi, M., Jones, G. C., Béthermin, M., et al. 2019, arXiv e-prints, arXiv:1910.04770
- Glazebrook, K., Schreiber, C., Labbé, I., et al. 2017, *Nature*, 544, 71
- Gnedin, N. Y., Norman, M. L., & Ostriker, J. P. 1999, in *American Institute of Physics Conference Series*, Vol. 470, *After the Dark Ages: When Galaxies were Young (the Universe at $2 < Z < 5$)*, ed. S. Holt & E. Smith, 48–57
- Grogin, N. A., Kocevski, D. D., Faber, S. M., et al. 2011, *ApJS*, 197, 35
- Gullberg, B., De Breuck, C., Vieira, J. D., et al. 2015, *MNRAS*, 449, 2883
- Guo, Y., Ferguson, H. C., Giavalisco, M., et al. 2013, *ApJS*, 207, 24
- Harikane, Y., Ouchi, M., Shibuya, T., et al. 2018, *ApJ*, 859, 84
- Hashimoto, T., Verhamme, A., Ouchi, M., et al. 2015, *ApJ*, 812, 157
- Hasinger, G., Capak, P., Salvato, M., et al. 2018, arXiv e-prints, arXiv:1803.09251
- Heckman, T. M., González-Delgado, R., Leitherer, C., et al. 1997, *ApJ*, 482, 114
- Hildebrandt, H., Pielorz, J., Erben, T., et al. 2009, *A&A*, 498, 725
- Hildebrandt, H., Erben, T., Dietrich, J. P., et al. 2006, *A&A*, 452, 1121
- Hsieh, B.-C., Wang, W.-H., Hsieh, C.-C., et al. 2012, *ApJS*, 203, 23
- Ilbert, O., Arnouts, S., McCracken, H. J., et al. 2006, *A&A*, 457, 841
- Ilbert, O., Capak, P., Salvato, M., et al. 2009, *ApJ*, 690, 1236
- Ilbert, O., Salvato, M., Le Floc'h, E., et al. 2010, *ApJ*, 709, 644
- Ilbert, O., McCracken, H. J., Le Fèvre, O., et al. 2013, *A&A*, 556, A55
- Iwata, I., Ohta, K., Tamura, N., et al. 2003, *PASJ*, 55, 415
- Jones, G. C., Carilli, C. L., Shao, Y., et al. 2017, *ApJ*, 850, 180
- Kashino, D., Silverman, J. D., Rodighiero, G., et al. 2013, *ApJL*, 777, L8
- Kashino, D., Silverman, J. D., Sanders, D., et al. 2017, *ApJ*, 835, 88
- Kennicutt, Jr., R. C. 1998, *ARA&A*, 36, 189
- Kewley, L. J., & Ellison, S. L. 2008, *ApJ*, 681, 1183
- Khusanova, Y., Le Fèvre, O., Cassata, P., et al. 2019, arXiv e-prints, arXiv:1903.01884
- Koekemoer, A. M., Aussel, H., Calzetti, D., et al. 2007, *ApJS*, 172, 196
- Koekemoer, A. M., Faber, S. M., Ferguson, H. C., et al. 2011, *ApJS*, 197, 36
- Kohandel, M., Pallottini, A., Ferrara, A., et al. 2019, *MNRAS*, 487, 3007
- Koyama, Y., Kodama, T., Hayashi, M., et al. 2015, *MNRAS*, 453, 879
- Labbé, I., Bouwens, R., Illingworth, G. D., & Franx, M. 2006, *ApJL*, 649, L67
- Laigle, C., McCracken, H. J., Ilbert, O., et al. 2016, *ApJS*, 224, 24
- Lam, D., Bouwens, R. J., Labbé, I., et al. 2019, *A&A*, 627, A164
- Le Fèvre, O., Béthermin, M., Faisst, A., et al. 2019, arXiv e-prints, arXiv:1910.09517
- Le Fèvre, O., Tasca, L. A. M., Cassata, P., et al. 2015, *A&A*, 576, A79
- Leitherer, C., Tremonti, C. A., Heckman, T. M., & Calzetti, D. 2011, *AJ*, 141, 37
- Loiacono et al. in prep.
- Ly, C., Malkan, M. A., Rigby, J. R., & Nagao, T. 2016, *ApJ*, 828, 67
- Ma, X., Hayward, C. C., Casey, C. M., et al. 2019, *MNRAS*, 487, 1844

Figure B.2. $F814W$ cutouts sorted by redshift (part 2).

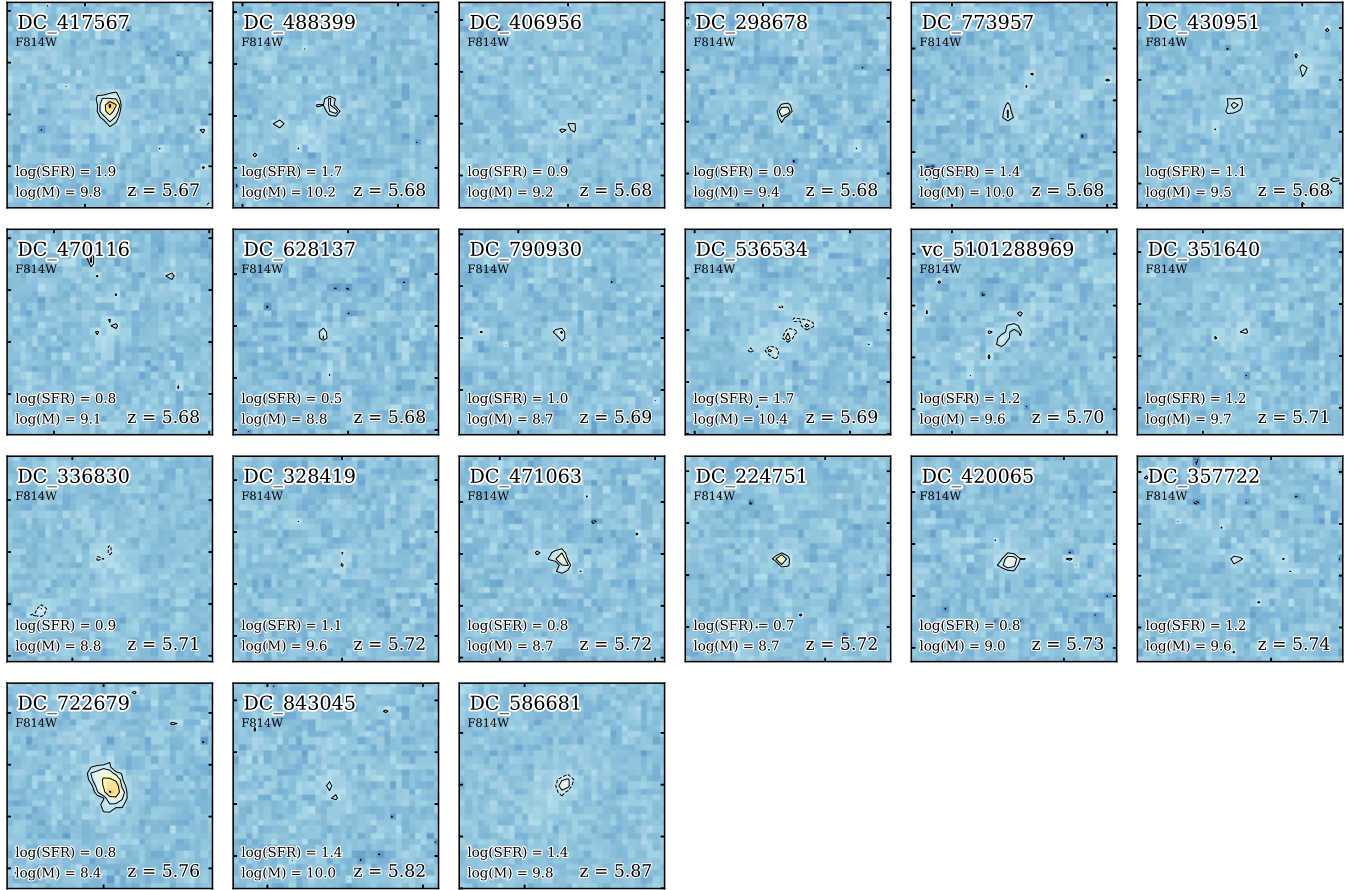


Figure B.3. *F814W* cutouts sorted by redshift (part 3).

- Malhotra, S., Rhoads, J. E., Pirzkal, N., et al. 2005, *ApJ*, 626, 666
- Mallery, R. P., Mobasher, B., Capak, P., et al. 2012, *ApJ*, 760, 128
- Maraston, C., Nieves Colmenárez, L., Bender, R., & Thomas, D. 2009, *A&A*, 493, 425
- Marchi, F., Pentericci, L., Guaita, L., et al. 2019, *A&A*, 631, A19
- Mármol-Queraltó, E., McLure, R. J., Cullen, F., et al. 2016, *MNRAS*, 460, 3587
- Masters, D., & Capak, P. 2011, *PASP*, 123, 638
- McCracken, H. J., Milvang-Jensen, B., Dunlop, J., et al. 2012, *A&A*, 544, A156
- McLean, I. S., Steidel, C. C., Epps, H., et al. 2010, in *Society of Photo-Optical Instrumentation Engineers (SPIE) Conference Series*, Vol. 7735, Proc. SPIE, 77351E
- McLean, I. S., Steidel, C. C., Epps, H. W., et al. 2012, in *Society of Photo-Optical Instrumentation Engineers (SPIE) Conference Series*, Vol. 8446, Proc. SPIE, 84460J
- Meurer, G. R., Heckman, T. M., & Calzetti, D. 1999, *ApJ*, 521, 64
- Mignard, F., & Klioner, S. 2018, in *IAU Symposium*, Vol. 330, *Astrometry and Astrophysics in the Gaia Sky*, ed. A. Recio-Blanco, P. de Laverny, A. G. A. Brown, & T. Prusti, 71–74
- Mignard, F., Klioner, S., Lindegren, L., et al. 2018, *arXiv e-prints*, arXiv:1804.09377
- Momcheva, I. G., van Dokkum, P. G., van der Wel, A., et al. 2017, *PASP*, 129, 015004
- Narayanan, D., Dave, R., Johnson, B., et al. 2017, *ArXiv e-prints*, arXiv:1705.05858
- Nonino, M., Dickinson, M., Rosati, P., et al. 2009, *ApJS*, 183, 244
- Oke, J. B. 1974, *ApJS*, 27, 21
- Ouchi, M., Shimasaku, K., Okamura, S., et al. 2004, *ApJ*, 611, 660
- Pahl, A. J., Shapley, A., Faisst, A. L., et al. 2019, *arXiv e-prints*, arXiv:1910.04179
- Pavesi, R., Riechers, D. A., Faisst, A. L., Stacey, G. J., & Capak, P. L. 2019, *ApJ*, 882, 168
- Pavesi, R., Riechers, D. A., Capak, P. L., et al. 2016, *ApJ*, 832, 151

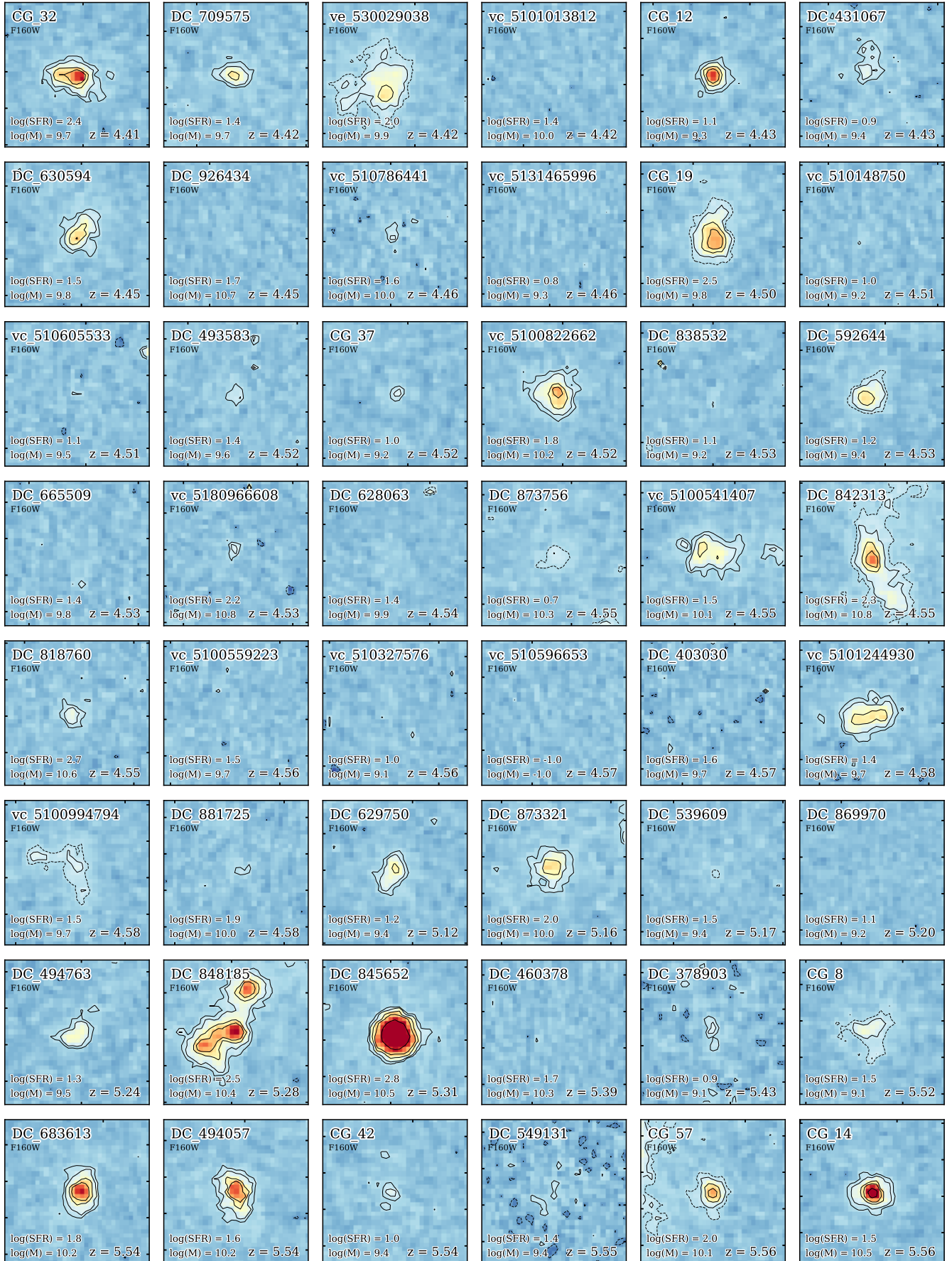


Figure B.4. $F160W$ cutouts sorted by redshift (part 1). The dashed contours show -3σ levels and the solid contours show 3σ , 5σ , 10σ , 15σ , and 30σ levels. All cutouts are $2''$ on each side.

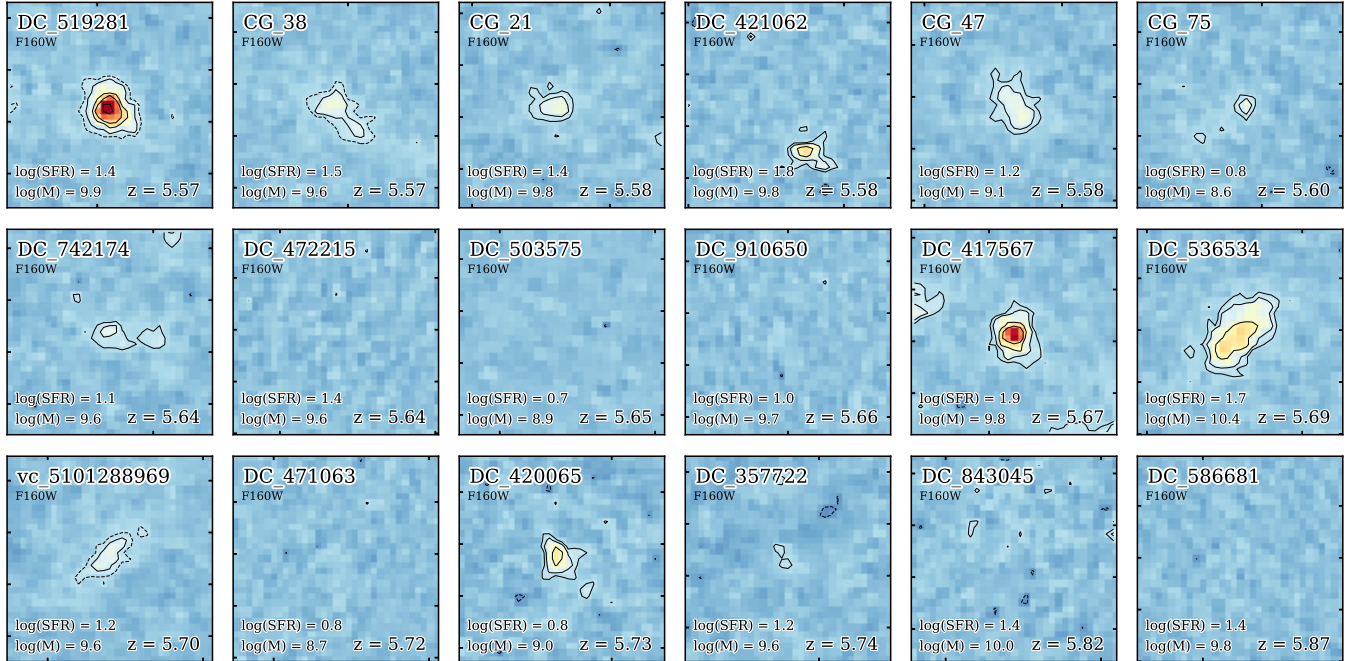


Figure B.5. *F160W* cutouts sorted by redshift (part 2).

- Pavesi, R., Riechers, D. A., Sharon, C. E., et al. 2018, *ApJ*, 861, 43
- Pineda, J. L., Langer, W. D., Velusamy, T., & Goldsmith, P. F. 2013, *A&A*, 554, A103
- Popping, G., Somerville, R. S., & Galametz, M. 2017, *MNRAS*, 471, 3152
- Prevot, M. L., Lequeux, J., Prevot, L., Maurice, E., & Rocca-Volmerange, B. 1984, *A&A*, 132, 389
- Puglisi, A., Rodighiero, G., Franceschini, A., et al. 2016, *A&A*, 586, A83
- Rasappu, N., Smit, R., Labbé, I., et al. 2016, *MNRAS*, 461, 3886
- Reddy, N. A., Erb, D. K., Pettini, M., Steidel, C. C., & Shapley, A. E. 2010, *ApJ*, 712, 1070
- Retzlaff, J., Rosati, P., Dickinson, M., et al. 2010, *A&A*, 511, A50
- Rhoads, J. E., Malhotra, S., Pirzkal, N., et al. 2009, *ApJ*, 697, 942
- Riechers, D. A., Carilli, C. L., Capak, P. L., et al. 2014, *ApJ*, 796, 84
- Sanders, D. B., Salvato, M., Aussel, H., et al. 2007, *ApJS*, 172, 86
- Schaerer, D., & de Barros, S. 2009, *A&A*, 502, 423
- Schaerer et al. in prep.
- Schlegel, D. J., Finkbeiner, D. P., & Davis, M. 1998, *ApJ*, 500, 525
- Scoville, N., Abraham, R. G., Aussel, H., et al. 2007a, *ApJS*, 172, 38
- Scoville, N., Aussel, H., Brusa, M., et al. 2007b, *ApJS*, 172, 1
- Shapley, A. E., Steidel, C. C., Pettini, M., Adelberger, K. L., & Erb, D. K. 2006, *ApJ*, 651, 688
- Shim, H., Chary, R.-R., Dickinson, M., et al. 2011, *ApJ*, 738, 69
- Skelton, R. E., Whitaker, K. E., Momcheva, I. G., et al. 2014, *ApJS*, 214, 24
- Smit, R., Bouwens, R. J., Labbé, I., et al. 2016, *ApJ*, 833, 254
- . 2014, *ApJ*, 784, 58
- Speagle, J. S., Steinhardt, C. L., Capak, P. L., & Silverman, J. D. 2014, *ApJS*, 214, 15
- Stacey, G. J., Geis, N., Genzel, R., et al. 1991, *ApJ*, 373, 423
- Stark, D. P., Schenker, M. A., Ellis, R., et al. 2013, *ApJ*, 763, 129
- Steidel, C. C., Erb, D. K., Shapley, A. E., et al. 2010, *ApJ*, 717, 289
- Steidel, C. C., Giavalisco, M., Pettini, M., Dickinson, M., & Adelberger, K. L. 1996, *ApJL*, 462, L17
- Steinhardt, C. L., Speagle, J. S., Capak, P., et al. 2014, *ApJL*, 791, L25
- Stockmann et al. in prep.
- Tanaka, M., Valentino, F., Toft, S., et al. 2019, arXiv e-prints, arXiv:1909.10721
- Taniguchi, Y., Scoville, N., Murayama, T., et al. 2007, *ApJS*, 172, 9

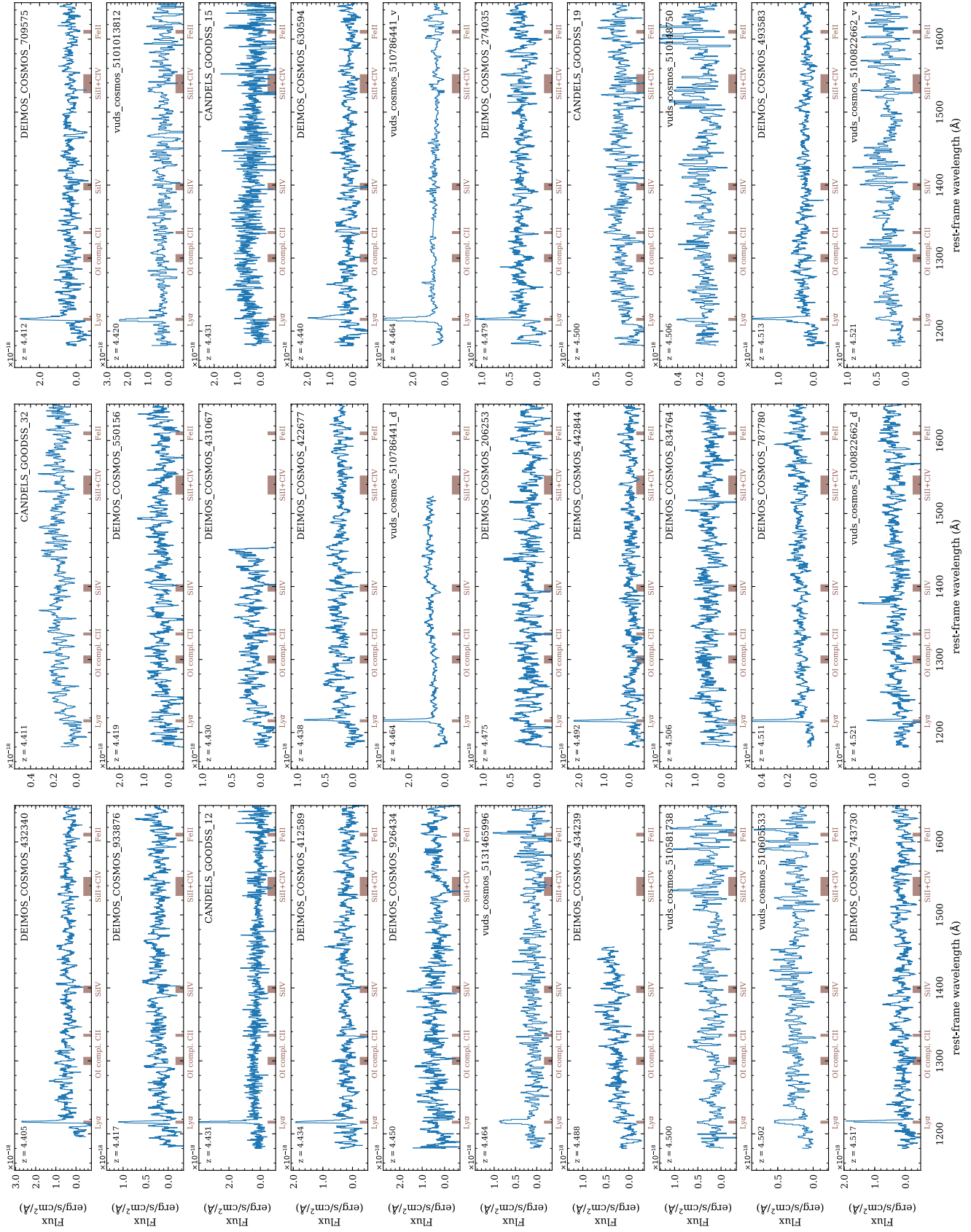


Figure B.6. Rest-frame UV spectra of all galaxies sorted by redshift (part 1).

- Taniguchi, Y., Kajisawa, M., Kobayashi, M. A. R., et al. 2015, PASJ, 67, 104
- Tasca, L. A. M., Le Fèvre, O., Ribeiro, B., et al. 2017, A&A, 600, A110
- Valentino, F., Daddi, E., Strazzullo, V., et al. 2015, ApJ, 801, 132
- Valentino, F., Tanaka, M., Davidzon, I., et al. 2019, arXiv e-prints, arXiv:1909.10540
- Vallini, L., Gallerani, S., Ferrara, A., Pallottini, A., & Yue, B. 2015, ApJ, 813, 36
- van Dokkum, P., Brammer, G., Momcheva, I., et al. 2013, ArXiv e-prints, arXiv:1305.2140
- Vanzella, E., Cristiani, S., Dickinson, M., et al. 2007, VizieR Online Data Catalog, 347
- . 2008, A&A, 478, 83
- Whitaker, K. E., Labbé, I., van Dokkum, P. G., et al. 2011, ApJ, 735, 86
- Whitaker, K. E., Ashas, M., Illingworth, G., et al. 2019, ApJS, 244, 16
- Willott, C. J., Carilli, C. L., Wagg, J., & Wang, R. 2015, ApJ, 807, 180
- Wuyts, S., Labbé, I., Förster Schreiber, N. M., et al. 2008, ApJ, 682, 985
- Wuyts, S., Labbé, I., Franx, M., et al. 2007, ApJ, 655, 51
- Yamanaka, S., & Yamada, T. 2019, PASJ, 71, 51

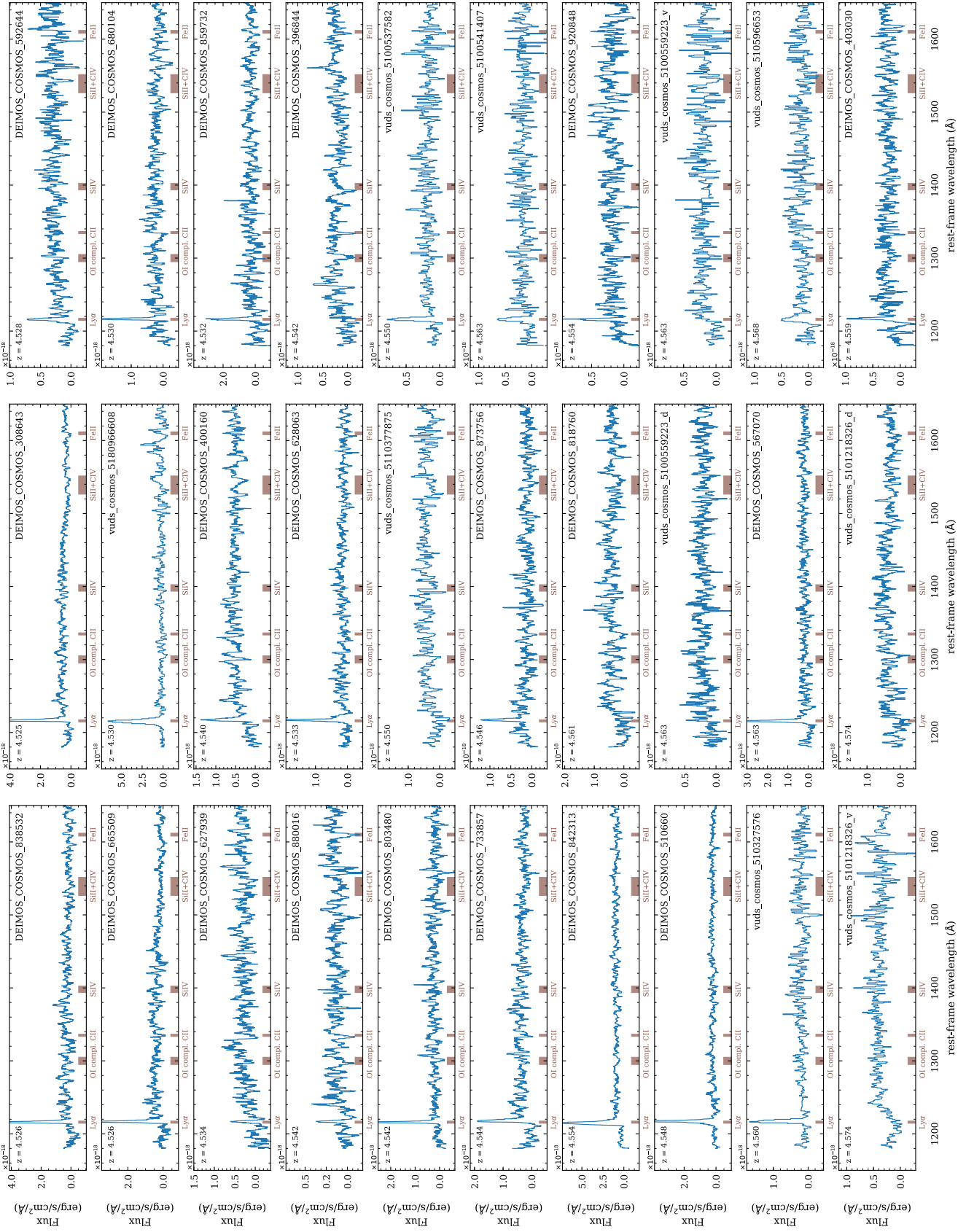


Figure B.7. Rest-frame UV spectra of all galaxies sorted by redshift (part 2).

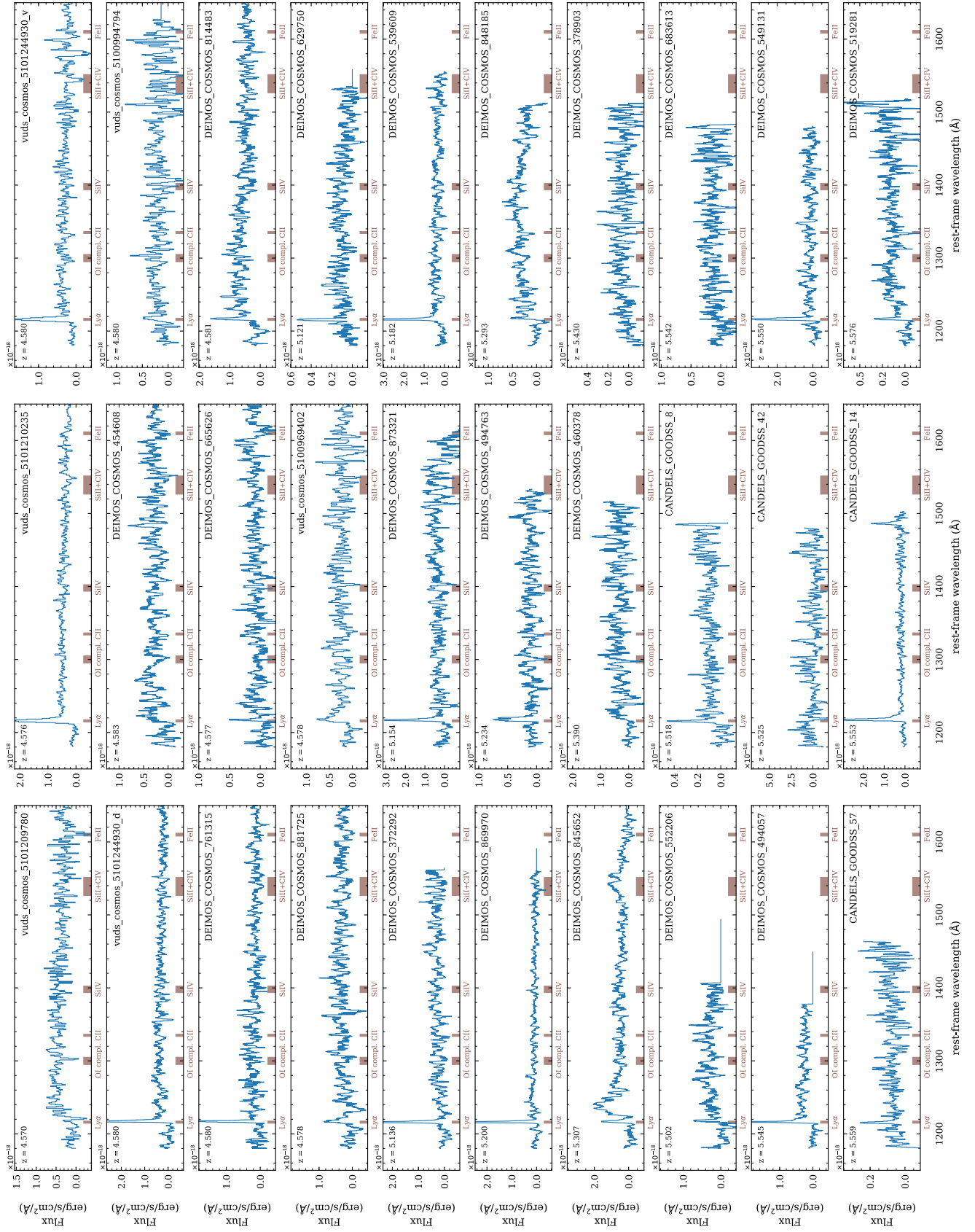


Figure B.8. Rest-frame UV spectra of all galaxies sorted by redshift (part 3).

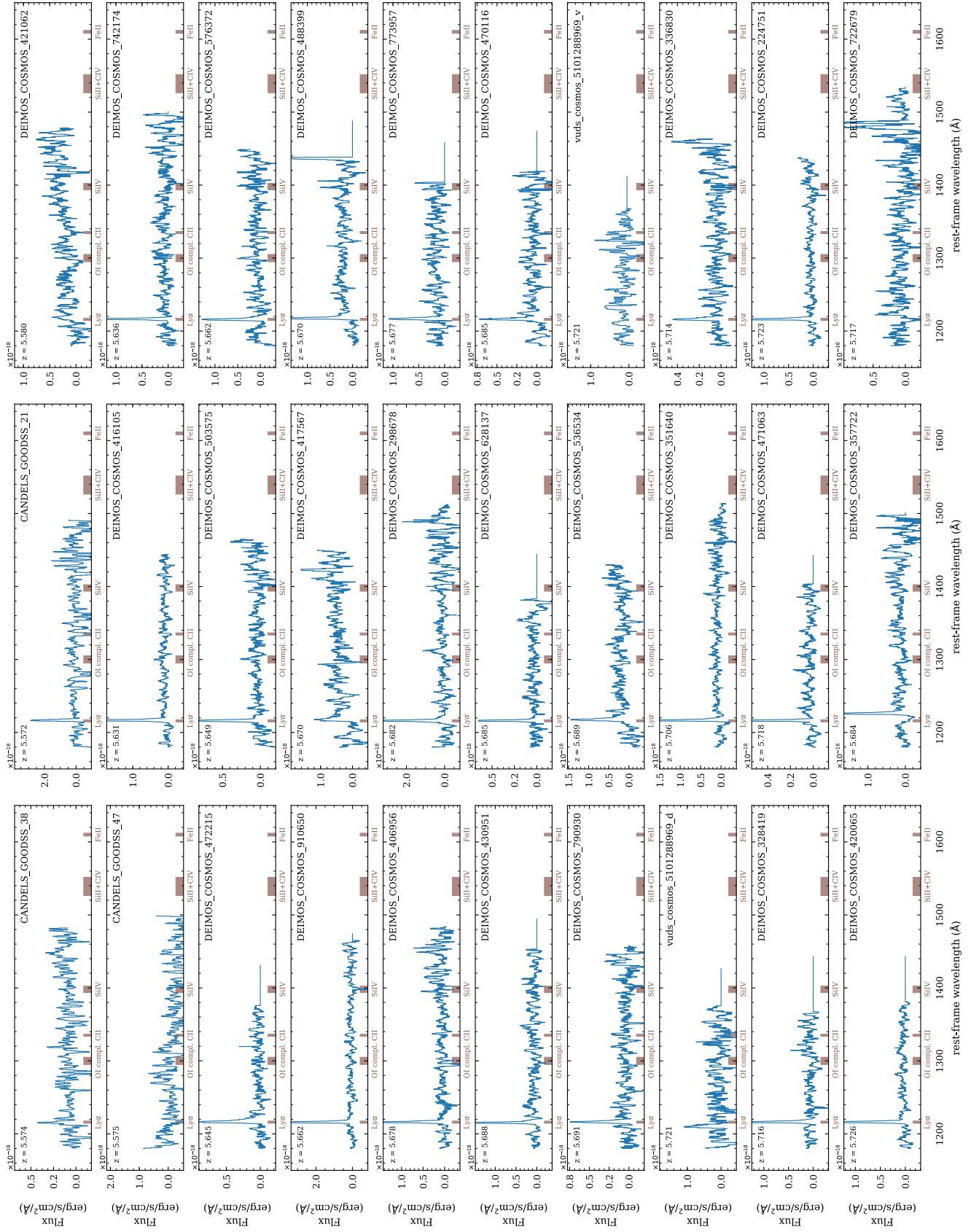


Figure B.9. Rest-frame UV spectra of all galaxies sorted by redshift (part 4).

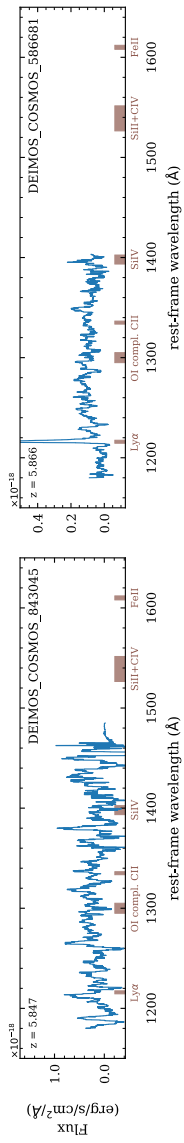


Figure B.10. Rest-frame UV spectra of all galaxies sorted by redshift (part 5).